SSC PC-037
137 PAGES

Proposal to the Physics Research Division

SSC Laboratory
United States Department of Energy

For: **Research and Development of Real Time Processing of Silicon Microvertex Data for the Forward Beauty Detector at the SSC**
(Research and Development for Major Detector Subsystems)

For the Period: January 1, 1990 to September 31, 1990

In the Amount: $413,500

Organization : The Regents of the University of California
Department of Physics
University of California, Los Angeles
405 Hilgard Avenue
Los Angeles, CA 90024-1547

Peter Schlein
Principal Investigator

William Slater, Vice-Chairman
Department of Physics

Elisabeth Johnson
Contract & Grant Officer

Date: 29 Sept 89

1. Introduction

Appendix A of this document contains a Letter-of-Intent that has been submitted to the SSC Laboratory for a Forward Beauty Detector (FBD) for the SSC. The FBD has been proposed (proposal P238) for the SPS-Collider. That proposal and its Addenda are hereto attached as Appendices B, C and D, respectively. It is planned that the FBD will run first at the SPS, then possibly at the Tevatron, UNK or LHC, and then transported to the SSC in time for startup in 1998.

The Forward Beauty Detector is distinguished by the following characteristics: (a) There are forward detectors installed on both arms, which cover apertures of 2-600 mrad from the outgoing beam directions. A silicon microvertex detector with elements perpendicular to the beam is installed inside the vacuum pipe; (b) Data acquisition is triggered by sophisticated real-time calculations on the microvertex detector data.

In the present document, we request funding to support the costs of Research & Development of the trigger and readout electronics. The nature of our proposed trigger (real-time calculations on silicon data) imposes several unusual demands which are discussed in the next chapter.

As we have noted in our SSC Letter-of-Intent, a detector of the type proposed is "transportable". That is, a forward detector which is designed to run at $\sqrt{s} = 0.63$ TeV can also be used at $\sqrt{s} = 40$ TeV with the addition of a downstream spectrometer which extends the coverage to smaller angles. Figure 1 to this document shows the average momentum of B-meson decay tracks vs. laboratory angle for the SSC and the SPS-Collider. In the angular range of the first spectrometer (100-600 mrad), the track momenta at SSC and SPS are nearly the same. Thus, the first spectrometer requires no changes. In the second spectrometer (10-100 mrad), tracks at the SSC have somewhat larger momenta. The larger momenta can be accomodated if the normal dipole magnet is replaced by a superconducting dipole when the transition to SSC is made. In the third spectrometer, which is added for the SSC transition, a superconducting dipole magnet would be used together with silicon tracking (maximum transverse size can be probably be limited to about 20 x 20 cm^2.

Our beauty program will evolve and lead to an SSC experiment in which we should have sufficient statistics to perform quality CP-Violation studies in B decay. We anticipate being able to start at the SPS-Collider in Fall 1990 with the fundamental silicon trigger test requested in the document attached as Appendix D to this proposal. Although uncertainties with future possibilties at the SPS-Collider, Tevatron, UNK and LHC make it impossible to predict with certainty how our future will develop beyond the silicon test in 1990, it seems likely that, before the SSC, our Beauty experiment will run on at least one of these colliders. Thus, we could be ready at SSC turn-on with a known, tested and reliable detector.

2. Proposed R. & D. Program

As outlined in the Introduction and in Appendix A, the proposed SPS-Collider detector can be used at the SSC with relatively straight forward modifications. Thus, all work on this detector is really preparation for an SSC Beauty experiment.

Although our unusual trigger, based entirely on real-time calculations on silicon data, is very challenging, it is recognized by the community to be an area worth considerable effort to develop. In particular, the SPS-Committee seems ready to recommend approval of a silicon trigger test run that we have requested (see Appendix D) at the SPS-Collider during its Fall 1990 operation. We expect to have the committee's response after their meeting on October 25, 1989. The results of this test run, if successful, will be of great import to B physics programs at all future hadron colliders.

Because of the importance of this program and our plans to continue on to the SSC, it is appropriate that we now seek SSC R&D support for the delicate job of designing the trigger and readout electronics.

Because of the unusual nature of the trigger, real-time calculations on silicon data, the demands made on the readout system and trigger processor are particularly severe:

- We read out the silicon detectors every time there is an interaction. This must be accomplished in the shortest possible time and the data transferred to the trigger processor.
- With the utilization of Data-Flow (Data-Driven) Architecture, the real-time calculations for one event can be completed in the short time of about 15 microseconds.
- All detector information must be read out between bunch crossings and stored until the trigger calculation is completed. Among other things, this requires a high capacity pipelined buffer

(FIFO) which has the capacity to store all events produced during this time. Thus, for example, a 10^6 Hz interaction rate would require a 15 event buffer capability (there are other reasons, discussed below, why the interaction rate probably should not exceed this value).

These points are discussed in somewhat more detail in Chapter 6 of the SPS P238 proposal (Appendix B to this document). In particular, Section 6.2 covers the readout system.

Although Section 6.1 (Appendix B) discusses the data-driven processor in general terms, we have since decided that, for the first version of the experiment, we can use existing modules of the Nevis/Univ. of Mass. data-driven processor design (B. Knapp et al.). This is discussed in Appendix A of P238-Addendum 1 (which is Appendix C to this document). It is explained there how we are currently proceeding with the development of a complete software emulation package which will allow us to determine precisely in how many clock cycles (in a 40 MHz clocked system), the calculations will be completed. This will determine the number of events which must be buffered and hence the necessary storage capacity of the FIFO's.

As suggested by the above demands, we shall develop fast hi-capacity FIFO's and high speed data links. We estimate that about 200 parallel data paths are necessary in the detector readout. In doing this, we shall attempt to make some use of the higher luminosity available at a proton-proton collider. However, as commented on above, radiation damage to the silicon from beam-beam interactions and problems arising from pileup, will likely limit our useable luminosity to about 10^{31}.

Concerning the data-driven processor, we expect to have a configuration of the Nevis-U. Mass. processor appropriate to our trigger requirements fully operational by February or March 1990. It is worth pointing out, as is discussed in the following chapter, that our group is quite strong in this area and we have full confidence that we shall succeed in this effort.

Extrapolation to the more complex event and possibly background of the SSC configuration, will require a re-engineering of the components involving greater speed, compaction and more complex modular components. A greater "user-friendliness" will also be developed.

3. Past Accomplishments in Electronics

Our group has an established track record in creating modern and key electronics components for high energy physics experiments.

In 1980, we installed, in our experiment R608 at the CERN-ISR, a very successful large wire-chamber TDC system (16,448 channels) with highly paralleled readout. It had 40 high speed parallel output data paths into central memory, with a total data transfer rate of 2 Gigabyte/second [see "A 16,000 Wire......." in Proceedings of the 1983 DPF Workshop on Collider Detectors"; LBL-15973]. The design, construction and installation of this system was all done by our UCLA group and took slightly more than one year from start to finish. In a system of this size, with about 80,000 MECL 10,000 IC's, it was also necessary to create on-line diagnostic software to find and locate failures at the chip level.

After the closure of the ISR, we later (1986) used 20% of this TDC system to instrument the wire chambers in the four Roman-pot spectrometers of our next experiment, UA8, at the SPS-Collider. The cleanliness and speed of the readout electronics made it possible for us to append to it a data-driven trigger processor system, which we designed to calculate the momentum of tracks which traversed the Roman-pot spectrometers. A selection of good tracks with momentum in the desired range provided the second level trigger for the experiment.

Design work for the UA8 data-driven processor began in December 1985. By April 1986, a completed processor was installed and running at the SPS-Collider [J. Zweizig et al., Nucl. Instr. & Methods A263 (1988) 188]. Each of the four Roman-pot spectrometers had its own processor, with each processor providing the equivalent of 60 MIPS of computing power. Thus, the entire system furnished 240 MIPS equivalent. The momentum calculation took 450 ns to perform. Imbedded in the TDC system referred to above, the entire process from RF signal to trigger signal was 1.2 microsec. Along with the hardware development was an impressive array of on-line calibration, diagnostic and monitoring software. As far as we know, this was the first true data-driven processor to run on-line in a high energy physics experiment. The trigger suppression could be as high as a factor of several hundred and yielded on-line momentum spectra which were of off-line quality.

Finally, it may be noted that we did pioneering work in the area of parallel processing. In summer 1982 (before the advent of ACP's), two of our engineers, Jamie Ellett and Alan Russ, write a very advanced UCLA report in which they outlined such a system A description of a version of this system later imbedded in FASTBUS was described by Ellett [VIRTUS: A Multi-Processor Event Selector Using FASTBUS; Proceedings of the 1983 DPF Workshop on Collider Detectors; LBL-15973, p. 185].

4. Budget and Discussion

We are proposing a total 9-month budget of $413,500. This includes funding for 2 electronics engineers, 2 technicians and 1 postdoctoral research physicist to work with them. In addition, there is $20,000 for test equipment and $20,000 for prototype module construction. There is also a travel budget of $10,000 as well as $7,445 for S.&.E.

The senior members of our group, Schlein, Erhan, Medinnis and Zweizig, are very experienced at interfacing to and working with electronics engineers and successfully obtaining needed results. Our collective experience with advanced digital systems and real time processing will allow us, together with the rather powerful electronics group implied by our budget, to create the necessary electronics systems which will provide the heavy flavor trigger at SSC.

The budget page shows Erhan, Medinnis and Zweizig working at 20% time on this project. This is meant to show the fraction of their time which will be devoted to problems specifically related to the SSC version of the experiment. In fact, they are working 100% of their time on the beauty experiment.

Concerning milestones, we expect to be able to have the completed SPS version of the experiment ready in 3 years (i.e., before the end of 1992), so that some data could be taken during the 1992 collider run. Thus, all electronics will be completed and fully operational by then. As stated above, we expect to have the data-driven processor completed about 6 months from now.

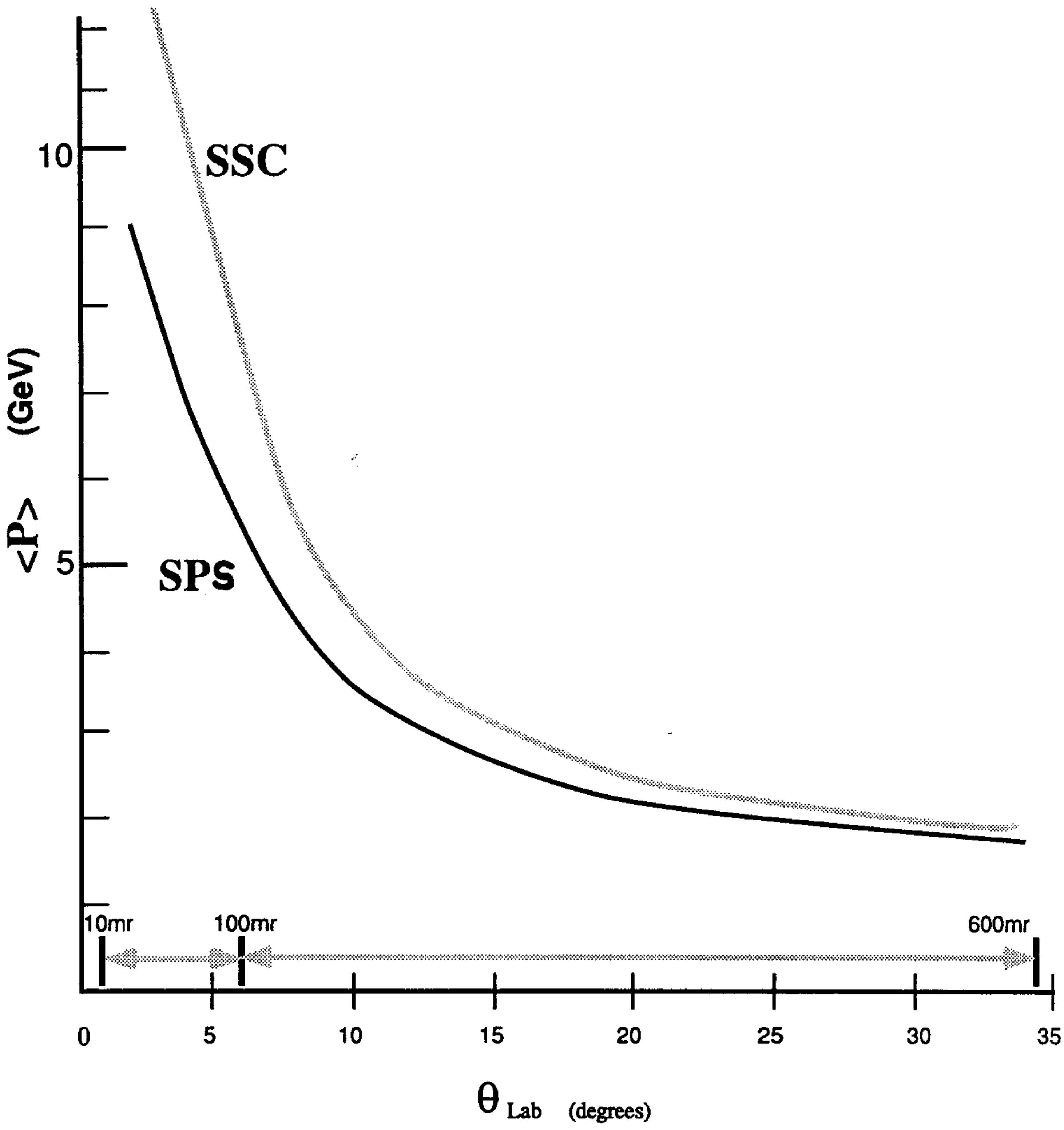

Figure 1: Average B decay track Momentum vs. Laboratory Angle.

Budget
1/1/90 to 9/30/90

1.) Salaries and Wages:

P. Schlein, Professor Principal Investigator 50% time on project		– 0 –	
S. Erhan Associate Research Physicist 20% time on project		– 0 –	
M. Medinnis Associate Research Physicist 20% time on project		– 0 –	
J. Zweizig Assistant Research Physicist 20% time on project		– 0 –	
Assistant Research Physicist I 100% time for 9 months Base Salary 1/1/90: $3,300/month		29,700	
Principal Development Engineer 100% time for 9 months Base Salary 1/1/90: $6,800/month		61,200	
Associate Development Engineer 100% time for 9 months Base Salary 1/1/90: $4,000/month		36,000	
Principal Electronics Technician V 100% time for 9 months Base Salary 1/1/90: $3,673/month		33,057	
Electronics Technician IV 100% time for 9 months Base Salary 1/1/90: $2,774/month		24,966	
	Total Salaries		$184,923

2.) Employee Benefits:

Academic @ 22%		6,534	
Staff @ 28%		43,463	
	Total Employee Benefits		$ 49,997

3.) Supplies and Services:

General Operating Supplies/Services		3,845	
Technical Illustration Service		1,800	
Telephone Expense		1,800	
	Total Supplies and Services		$ 7,445

4.) Equipment:

Test Equipment		20,000	
	Total Equipment		$ 20,000

5.) Travel:

Domestic Travel: 10 trips @ $700/trip		7,000	
Foreign Travel: 2 trips @ $1,500/trip		3,000	
	Total Travel		$ 10,000

6.) Fabrication:

Electronic Modules		20,000	
	Total Fabrication		$ 20,000

7.) Indirect Costs:

Overhead @ 48% on MTDC		121,135	
	Total Budget		$413,500

APPENDICES

A. **Letter of Intent for Forward Beauty Detector at SSC**

B. Proposed P238 to SPS-Committee:
Study of Beauty Physics at the SPS-Collider with Real-Time Use of Silicon Microvertex Data.

C. P238-Appendix 1:
Measurement of B_S-Mixing

D. P238-Appendix 2:
Request for Collider Test of Silicon Microvertex Detector.

APPENDIX A

APPENDIX A

UNIVERSITY OF CALIFORNIA, LOS ANGELES UCLA

BERKELEY · DAVIS · IRVINE · LOS ANGELES · RIVERSIDE · SAN DIEGO · SAN FRANCISCO SANTA BARBARA · SANTA CRUZ

DEPARTMENT OF PHYSICS
LOS ANGELES, CALIFORNIA 90024

24 September, 1989

Professor R. Schwitters
Directors Office
SSC Laboratory
2550 Beckleymeade Avenue
Dallas TX 75237

Dear Roy,

A collaboration, for which I am spokesman, recently submitted a proposal to the SPS-Committee for a new collider detector, dedicated to the study of Beauty physics (P238 and P238-Addendum appended). Since this proposal embodies a new approach to the study of B physics at hadron colliders, and by now has more than 6 physicist-years of trigger and detector Monte-Carlo simulation work behind it, I believe it has important implications for the SSC. I am writing to bring to your attention the essential arguments we have developed and to draw preliminary conclusions of the implications for B physics studies at SSC.

The first point is that the production of B-Mesons from gluon-gluon fusion is markedly polar in laboratory production angle at high energies. For example, the following figure (from ISAJET) shows the angular distribution of B-Meson decay products at the SSC.

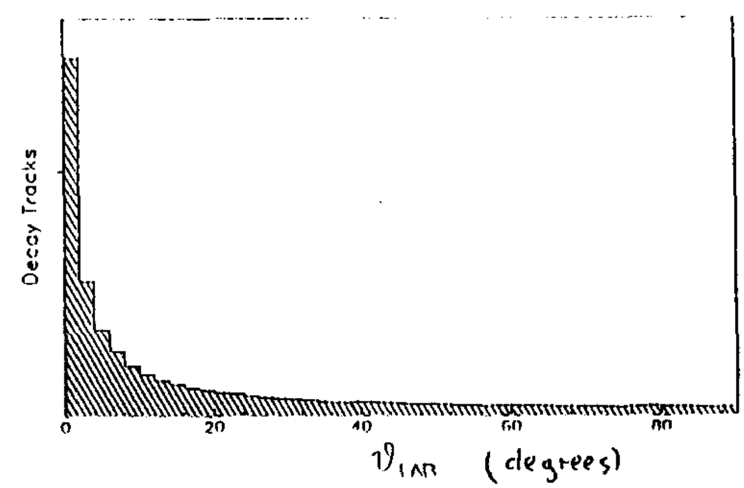

This peaking argues for forward detectors (on both arms). For the apparatus proposed in P238, which is an extension of devices pioneered at the ISR, apertures of ±600 mrad around the beam pipes lead to about 60% of all $B\bar{B}$ events at the SSC having all the decay products of at least one of the B's fully contained in the detector aperture.

In a forward SSC spectrometer with aperture 2-600 mrad, the average momentum of the accepted B-mesons, $<P_B>$ = 270 GeV/c, while central B's accepted in a rapidity range of, for example, −2 to +2 have $<P_B>$ = 7 GeV/c. There are many clear experimental advantages of working with higher momentum samples of B-mesons in a forward planar detector, such as in particle identification with RICH counters, measurements of B proper decay time, reconstruction of exclusive final states with photons, etc.

The second essential point is that reconstruction of exclusive final states in B-decay with minimal background is made possible with the use of a somewhat unorthodox silicon micro-vertex detector, whose planar elements are perpendicular to the beam and installed inside the vacuum pipe (actually inside a secondary vacuum, to provide RF shielding and avoid contaminating the main machine vacuum). The detector planes are spaced every 4 cm throughout the ± 30 cm (at the SPS) of the interaction region. The detectors, which are normally 2 mm from the beam, would be retracted about 10 cm from the beam line when the machine is not in "stable beam" state.

Triggering is another essential point. With extensive and careful Monte-Carlo calculations, we have shown that data acquisition can be efficiently triggered by the results of sophisticated real-time computation of data from the micro-vertex detector. We anticipate being approved by CERN to perform a silicon test run in the SPS-Collider in 1990 in order to be certain that event-unrelated signals from beam halo and other "noise" will be at a manageable level. The results of these tests, if successful, should be of great import to B physics programs at all future hadron colliders.

Extrapolation of the proposed SPS experiment to the SSC involves several important considerations:

- There is a natural limit to the useable luminosity which is determined by pileup considerations, complicated by the need for real-time pipelined calculations, and also by radiation damage to the silicon detectors due to the beam-beam interaction rate. We are currently studying this question for the SSC, although we think that, for this type of experiment with elaborate silicon systems close to the beams and in which exclusive final states are reconstructed, one probably will not want to run with luminosities larger than 10^{31} $cm^{-2}s^{-1}$.

- Our present two-spectrometer system (with θ_{min} = 10 mrad) and total length of ± 11 meters would have to be supplemented by an additional spectrometer in order to extend coverage down to smaller θ_{min}. Our preliminary estimate (using ISAJET) is that the addition of a third spectrometer with aperture from 2 to 10 mrad will result in less than a 10% loss of B-mesons due to lost small angle particles in the beam pipe.

We estimate that, due to a number of reasons (mainly: larger B cross section, σ_B/σ_{total} ratio, available luminosity and forward collimation of B decay products), a factor of at least 500 times larger event samples should be obtainable at the SSC than at the SPS-Collider. This should place such an experiment well over the threshold to perform quality CP-violation studies in B decay.

I anticipate that, by the time of your May 1990 deadline for letters-of-intent, a new collaboration will have formed around the ideas developed by the P238 collaboration and summarized in this letter. Some fraction (to be determined) of our existing SPS collaboration will likely form the nucleus of such a new collaboration. Until then, I would like to request that the SSC laboratory consider an experiment of the type discussed here as one of the possible options for future SSC experiments.

Peter E. Schlein
Professor of Physics

APPENDIX B

APPENDIX 1

EUROPEAN ORGANIZATION FOR NUCLEAR RESEARCH

CERN-SPSC/88-33
SPSC/P238
16 January 1989

PROPOSAL to the SPSC

STUDY OF BEAUTY PHYSICS AT THE SPS-COLLIDER WITH REAL-TIME USE OF SILICON MICROVERTEX INFORMATION

A. Brandt, S. Erhan, D. Lynn, M. Medinnis, P. Schlein*, J. Zweizig
University of California, Los Angeles, U.S.A.

T. Ypsilantis
College de France[1], Paris, France

G. Borreani
University of Ferrara and INFN[2], Italy

M. Calvetti
University of Perugia and INFN[2], Italy

J.B. Cheze, J. Zsembery
Centre d'Etudes Nucleaires – Saclay[3], Gif-sur-Yvette, France

R. Dznelyadin, Y. Guz, V. Kubic, V. Obraztsov, A. Ostankov
IHEP-Serpukhov, Protvino, U.S.S.R.

C. Biino, R. Cester, A. Migliori, R. Mussa, S. Palestini
University of Torino and INFN[2], Italy

ABSTRACT

We propose a high statistics study of the physics of Beauty particles with a new detector at the SPS-Collider. Data obtained from a silicon micro-vertex detector installed inside the vacuum chamber throughout the interaction region are used by an on-line system of Data-Driven Processors to trigger on events containing secondary vertices from short-lived particles. With our proposed triggering scheme, more than 2×10^5 B-mesons can have reconstructable exclusive final states with low background per 10 $pbarn^{-1}$ integrated luminosity.

---

*) Spokesman
[1]) Pending approval of the Laboratory and IN2P3
[2]) Pending approval of INFN
[3]) Pending approval of CEN-Saclay

TABLE OF CONTENTS

APPENDICES

1. INTRODUCTION

This document is a proposal for a Forward Beauty Spectrometer to study the physics of Beauty quark systems at the CERN SPS-Collider. Although hadron colliders are prolific sources of b-quarks and are, in fact, "B-Factories", the efficient isolation of such events from the much larger minimum bias background will require real-time vertex calculations based on silicon micro-vertex detector data. We plan to achieve the necessary computing power with the use of Pipelined Data-Driven Processors.

For the following reasons, we have chosen to focus our attention in the forward direction of the $p\bar{p}$ system:

- The solid angle density of b and $\bar{b}$ quarks resulting from gluon-gluon fusion is considerably larger in the forward direction than at 90°.

- The momenta of B-mesons in the forward direction are much larger than at 90°. Thus, the decay products are easier to track reliably and vertex and overall topology definition is improved. Moreover, B's travel further thereby facilitating B-$\bar{B}$ oscillation studies. Particle identification is easier. Calorimetric reconstruction of π^0 and γ detection are enhanced.

- Λ_b and Λ_c baryons can be studied in the forward direction. These may provide very effective flavor tagging for the accompanying B-mesons.

- Because of the relatively small solid angle coverage compared with an apparatus at 90°, the cost of our proposed experiment is relatively modest. Moreover, design and construction of a forward planar geometry detector is easier and therefore, also for this reason, less expensive.

- The forward peaking of heavy flavor particles should be even more pronounced at the higher energy UNK, LHC and SSC colliders. Thus, we believe that our proposed experiment would be a first example of an important class of future experiments.

In the body of this proposal we present details of the trigger design and detector which could furnish more than 2×10^5 reconstructed B-Mesons per 10 pbarn^{-1} integrated luminosity at the CERN SPS-Collider with $\sqrt{s}$ = 630 GeV. The actual number of reconstructed events which we obtain will depend on whether one or both collider arms are instrumented with spectrometers (the proposed silicon and trigger systems are bi-directional and will serve either situation) and whether or not the desired π^0 and γ detection capability is implemented. Possible strategies on how to proceed with these decisions are discussed in the last chapter of this proposal. However, all rate estimates in the proposal assume a two-spectrometer system and π^0,γ capability in order to demonstrate the full potential of this type of experiment.

In Chapter 2 we discuss the physics goals of the experiment and the capabilities of other existing or planned Beauty experiments. Chapter 3 contains a discussion of the general acceptance properties of our proposed apparatus, a performance summary of the trigger, based on real time calculations of silicon micro-vertex detector data as detailed in Chapter 4, and the expected data acquisition rates.

The silicon micro-vertex detector is described in Chapter 4. This chapter also contains the results from a Monte Carlo simulation of the response of this detector to minimum bias, $b\bar{b}$ and $c\bar{c}$ event samples, as well as the results of a detailed simulation study of a trigger algorithm which can suppress the minimum bias events by a factor of 1/500.

Chapter 5 contains a description of a large aperture forward detector consisting of two coaxial spectrometers, each optimized for the angular range it covers (10-100 mrad and 100-600 mrad, respectively). The particles emerge from the vacuum pipe into the spectrometers through thin windows and are tracked through a large aperture quadrupole magnet in the first spectrometer or through a large aperture dipole magnet in spectrometer 2. There are gas and liquid RICH counters in each spectrometer for particle identification and there are plans to install excellent electromagnetic calorimetry for π^0

and γ detection (see Appendix D) if the collaboration expands further. This system is based on our combined experience with forward collider detectors (R603 and R608 at the ISR), with experiment UA8 at the SPS-Collider, and with the development of Ring Imaging Cherenkov (RICH) counters.

Chapter 6 describes how the silicon data will be analyzed in real time by a Pipelined Data-Driven Processor[2,3,4] which can perform the enormous number of instructions needed to reject more than $\approx$99.8% of the minimum bias events without incurring any appreciable dead-time. The successful development of this type of real-time processing capability adapted to the specific problems of μVertex detectors will make it possible to perform very high rate $b\bar{b}$ experiments at hadron colliders. The experience of some of us with a Data-Driven Processor in experiment UA8[4] gives us confidence that we can proceed with the more ambitious project discussed here. The readout system will read all the event data from the detectors in the 3.8 μsec between bunch crossings, and store it in pipelined buffer memory while the processor is making a decision.

Chapter 7 deals with the off-line reconstruction problems using several typical B^0-meson decay modes. Analysis results are given using reconstruction software written to analyze and find signals for five different B decay modes from Monte Carlo generated event samples. Quantitative estimates are given of the combinatoric background which is expected. The well defined B vertex determines its momentum direction, thus allowing the use of transverse momentum balance with respect to that direction to greatly suppress combinatoric background. Realistic trigger and reconstruction efficiencies are obtained for the five decay modes.

In Chapter 8, we present a detailed evaluation of the total B yields which are possible with the proposed detector both with and without π^0 and γ detection. Based on these results, we also evaluate our sensitivity to B-$\bar{B}$ mixing studies.

Finally, in Chapter 9 we discuss the proposed time scale for the experiment and our estimates of the costs involved.

2. *PHYSICS GOALS*

The physics of the beauty sector is extremely rich and can be subdivided into two main areas.

(a) The study of the mixing matrix of weak interactions. In principle, enough information can be extracted from the study of the decays of the lowest mass states of hadrons with a b quark to determine the five unknown elements of the mixing matrix. Major goals here are the detection of possible deviations from the predictions of the 3-generation version of the Weinberg-Salam model and of CP-violation effects. Direct violations of CP-invariance in the decay matrix could give rise to large asymmetries between rates for a given decay process and its CP conjugate. Such violations would be flavour dependent while a violation in the mass matrix (as is the case if it originates from a superweak interaction) would produce effects of the same order of magnitude, independent of flavour.

(b) The measurement of lifetimes, branching ratios and especially the detection and detailed study of suppressed channels, will shed light on the decay mechanism through quark graphs other than the spectator ones. Moreover, the fact that the decaying quarks are not free particles, but are bound by the strong force implies that the study of the weak decays of particles with heavy flavours is a testing-ground for the understanding of QCD effects in the perturbative regime.

A full account of (a) and (b) are contained in many recent reviews and will not be repeated here. Instead, we would like to emphasize the areas where the proposed experiment can give substantial, and possibly unique, physics contributions. This, of course, depends on the time scale of the experiment.

We assume that the low energy e^+e^- machines will continue to produce data with improving luminosity, such as envisaged at CESR, and that the Fermilab fixed target program will follow the proposed lines. We also assume that our proposed experiment will get on the air and produce results before a new detector for the upgraded Tevatron is operational, before LEP is operated in the high intensity mode and before a low energy e^+e^- machine with a luminosity of 10^{34} cm^2s^{-1} becomes available. In other words, we assume that our detector is ready to take data not later than 1992.

The proposed experiment has several major strong points. The SPS-Collider can indeed be considered a Beauty factory. As discussed in the following chapter, it should be possible to achieve the production of more than 10^8 $b\bar{b}$ events each year. With the proposed setup, more than 2×10^5 of these can yield reconstructed exclusive final states with at least one B-meson. Specific low multiplicity channels will however be reconstructed with much higher efficiencies, allowing the detection of interesting channels below the 10^{-5} branching ratio level.

Our emphasis in design of the proposed experiment has been to provide a means for triggering on displaced vertices alone and to have 100% hadron identification and good invariant mass resolution. The detector design includes a system of calorimeters of superb quality which would allow the efficient reconstruction of π^0's, the precise measurement of their energies and, together with the Ring Imaging Cherenkov Counters, provide excellent electron identification.

In order to fully evaluate the potential of this experiment we must first review the program for Beauty experiments at machines which will be active in the next few years (Table 1).

Table 1: A Comparison of Beauty Factories

		E_{CM} [GeV]	$\int\mathcal{L}dt$ [$pb^{-1}y^{-1}$]	$\sigma_{b\bar{b}}$	$N_{b\bar{b}}$ [y^{-1}]	$\sigma_{b\bar{b}}/\sigma_{incl}$
This Proposal (SPS Collider)	$p\bar{p}$	630	10	10 μb	10^8	2×10^{-4}
DORIS	e^+e^-	10.6	200	0.9 nb	2×10^5	0.19
CESR	e^+e^-	10.6	1000	1.1 nb	10^6	0.23
LEP	e^+e^-	93	100	5 nb	5×10^5	0.14
HERA	ep	300	100	4 nb	4×10^5	10^{-3}
TeV−II	pW	~50	100	~1 μb	~10^8	10^{-6}
TeV−I	$\bar{p}p$	2000	10	45 μb	4.5×10^8	3×10^{-4}
TeV upgrade	$\bar{p}p$	2000	500	45 μb	2.3×10^{10}	3×10^{-4}
SSC	pp	40000	10000	0.5 mb	5×10^{12}	5×10^{-3}
PSI	e^+e^-	10.6	10000	1.1 nb	10^7	0.23

e^+e^- Machines: The existing machine which has the highest potential is CESR with a projected luminosity in excess of 10^{32} and a corresponding integrated luminosity of 1000 pb^{-1}/year. With a $b\bar{b}$ cross section of 1.1 nb at the $\Upsilon(4S)$, it will produce about 10^6 $b\bar{b}$ events per year. The ratio of $b\bar{b}$ to total cross section is large, 0.23. In spite of this, up to now the reconstruction efficiency has been only 10^{-3}. This low efficiency can be traced back to two factors; the difficulty of resolving secondary vertices in this low energy regime and the large combinatorial background made much worse by the fact that the decay products of the two B's overlap over the entire solid angle (B's are emitted nearly at rest at the $\Upsilon(4s)$) and by the incomplete coverage of particle identification detectors. The CLEO detector is presently undergoing a major upgrade that will result in better π/K separation and improved momentum and energy measurements. Electron identification will be close to 100%. With this in mind, one can anticipate that CESR will dominate the scene in the study of semi-leptonic decays and time integrated decay asymmetries in semi-leptonic and inclusive hadronic channels. By identifying the semi-leptonic decay of one of the B's, an unbiased sample of decays from the $\overline{B}$ can be obtained; assuming 10^{-2} tagging efficiency, the number of events before reconstruction is about 10^4. Interesting results may come from measurements at the $\Upsilon(5s)$ resonance which should be above threshold for B_s formation. The production cross section for B_s is expected to be approximately 10% that for $B_{u,d}$.

LEP: When LEP reachs its design performance, about 5×10^5 $b\overline{b}$ events will be produced per year at each detector. The ratio of $b\overline{b}$ production to total cross section is 0.14. The advantages in this case come from the fact that there is considerable energy release in the reaction and therefore that the B flight path is quite long. Moreover, the B decay particles and those from the $\overline{B}$ tend to be separated in opposite hemispheres, therefore reducing the combinatorial background. The four LEP detectors are equipped with electromagnetic and hadronic calorimetry which will make lepton identification relatively easy. Of the four detectors, DELPHI will probably give the best results on exclusive decay channels. Vertex analysis is made difficult by the relatively large pipe diameter of LEP, although that may be improved with time. It may be noted, however, that with our average reconstructed B-meson momentum of about 35 GeV (see Chapter 3), we may do at least as well as LEP in decay time measurements.

Fixed Target Experiments at Fermilab and CERN: Elementary cross sections for $b\overline{b}$ production are of the order of 2-20 nb. With heavy targets, one can in principle achieve $b\overline{b}$ production rates comparable to those obtained at existing colliders. However the limiting factor in these experiments is the high background to signal ratio, $\approx 10^6$, and the difficulty of handling the correspondingly high rates. For example, taking into account spill duration and repetition rate, a typical run averages of the order of 10^6 sec at CERN and reached 3.5×10^6 sec during the 7 month 1987 run at FNAL. The experiments can be characterized by the accepted intensities which range from 10^4 to $>10^7$ interactions/sec, with the low intensity ones featuring an open trigger that allows the collection of an unbiased sample of $B\overline{B}$, and the high intensity ones restricting their acceptance to specific decay channels (2μ or exclusive 2 charged bodies).

The large majority of these experiments is equipped with sophisticated vertex detectors to separate out secondary vertices. These experiments are likely to yield the most accurate measurements of particle lifetimes.

Beauty Physics at Colliders, with Existing Detectors: At this time, the large collider detectors are concentrating on the search for heavy objects: top, higgs, supersymmetric particles etc. and any upgrade to increase the probability to detect B's is really addressed to an effort to improve on the signature for these heavy objects. Future upgrades involve the construction of vertex detectors, with no provision of using them in the trigger process. The trigger scheme used so far to select B final states is based on the identification of μ's with a typical efficiency of 10%, useful only for high p_t μ's where the background from light particle decay can be handled. Also, none of these detectors has high quality hadron identification. In conclusion, one expects that these high rate experiments will only contribute to the study of inclusive semileptonic decays and of mixing by measuring the ratio (r) of B^0 decays to $\overline{B}^0$ decays, integrated over time and over the flavour of the light quark bound to the b quark.

In the following paragraphs, we discuss some of the important measurements that we plan to carry out, their relevance to the physics objectives and the impact that our proposed experiment can have, and also evaluate for each case, the expected performance of competing experiments.

a) Production Cross Sections for b−hadrons from a $p\overline{p}$ initial state: The measurement of the $b\overline{b}$ production cross section over the kinematical range of the experiment will provide information on the gluon structure function and on the production mechanism, at collider energies, allowing a significant test of QCD. (Here the only competitors are the big collider experiments, which however can produce an accurate measurement only in a small kinematic domain where the $b\bar{b}$ event sample is not dominated by background). Moreover, this experiment will allow us to study the mechanism of fragmentation of heavy quarks into hadrons, included the controversial area of baryon formation.

b) Spectroscopy of low lying b states: (B_u, B_d, B_s, B_c and their antiparticles; $\Lambda[bdu]$, $\Sigma[buu]$, etc..) This field is wide open with only B_u and B_d firmly established. The main requirements here are the capability to fully reconstruct individual decay channels and the ability to precisely determine the reconstructed masses; the proposed experiment is optimally suited to cover this area. Since the identification of b-particles does not require large statistics, it is conceivable that even low intensity, fixed target experiments like WA-82 or WA-84 will soon discover some of the states most copiously produced and that the B_s be identified at CESR or DORIS in the study of the (5S) Upsilon. In any case this will remain an open field in 1992 with some of the most interesting states, (such as the B_c, the bound state of heavy quarks of different masses) probably still undiscovered.

c)Masses and Lifetimes: With the proposed experiment it will be possible to directly measure the life time of meson and baryon ground-states (B_s, B_c, Λ_b etc.). This is a non trivial experiment and will require the full power of a detector of the kind we are proposing. Some partial results in this area are likely to be obtained by fixed target experiments.

d) Mixing: A very important measurement is that of the mass difference between the two lifetime eigenstates in the $B_d{}^0$ and $B_s{}^0$ systems. In the hypothesis that direct $\Delta S=2$ transitions do not exist, the mass difference,

$$\Delta m = m_H - m_L = < \bar{B}^0 \mid H \mid B^0 >$$

is given by the amplitude of second order weak interactions quark graphs. The evaluation of these graphs yields the amplitude:

$$\Delta m = (G_F{}^2/6\pi^2) B_b\, f_b{}^2\, m_b\, \tau_b\, |V_{tq}|^2\, m_t{}^2\, F(m_t{}^2/m_W{}^2)\, \eta_{QCD}$$

with a direct dependence on V_{tq} ($q=d,s$).

The parameters Δm and $\Gamma = (\Gamma_H + \Gamma_L)/2$ characterize the time evolution of the eigenstates of flavour, as produced in strong interactions:

$$|B_{phys}{}^0(t)> = e^{-i(m_H + m_L)t/2}\, e^{-\Gamma t/2}\, [\cos(\Delta m\, t/2)|B^0> + i \sin(\Delta m\, t/2)|\bar{B}^0>]$$

The appearance of an antiparticle from an initially pure particle state is a phenomenon well known from K physics, which is referred to as 'mixing'. Clearly if $\Delta m \ll \Gamma$, very little mixing can take place before the particle decays. Mixing can be studied by measuring the time evolution of B^0 ($\bar{B}^0$) and fitting the distribution with the appropriate values of the parameters Γ and Δm or by measuring the ratio (r) between the number of B^0 decays to the number of $\bar{B}^0$ decays, obtained by integrating over the decay region. In practice, for B lifepaths of $\approx(340 \times \gamma_B)$ μm, the large majority of experiments will only perform the second kind of measurement which is less sensitive than the first one and will give only the ratio of the parameters: $\Delta m/\Gamma$. A dramatic loss of sensitivity in the time integrated measurement occurs when $\Delta m/\Gamma \gg 1$, since in this case both particle and antiparticle amplitudes undergo a large number of oscillations within a lifetime, so that, by integrating over time, the probability of detecting the particle is equal to that of detecting the antiparticle. It is now expected that B_s will show precisely this behaviour and therefore it will be very important to measure the time evolution of this state.

The ratio $\Delta m_d / \Delta m_s$ gives directly the ratio of the mixing decay matrix elements $|V_{td}/V_{ts}|$, since all other factors cancel in the ratio of amplitudes for the corresponding quark box diagrams.

Since one must separate, on an event by event basis, the flavour of the light quark (either d or s) bound to the b quark, this measurement requires the ability to identify B_s and B_d mesons either with an accurate determination of the mass or by the identification of unambiguous decay channels. Therefore measurements based on the detection of inclusive semileptonic or charmed final states do not provide sufficient information. We believe that the proposed experiment will be able to perform a significant measurement in this area.

c) Detection of Rare Decay Channels: In a run with 10 $pbarn^{-1}$ integrated luminosity, it is shown in Chapter 8 that $\approx 6.4\times10^{7}$ B-mesons (per year) have all decay tracks fully contained in the spectrometer. With a combined 10% efficiency for triggering and reconstruction (this efficiency may be larger) and a 68% pileup efficiency (see Chapter 3), one event with a branching ratio of 2.3×10^{-6} can be seen (with a two-spectrometer system). At this level of sensitivity, a search for rare decays will be one of the interesting goals of the experiment.

B decays are the optimal sector to study the effects of loop diagrams. As for K's, they can only decay with a generation jump: in the case of K's the dominant quark transition is $s \rightarrow u$ while B-mesons decay predominantly through $b \rightarrow c$; in both cases we are dealing with Cabibbo-suppressed transitions. In this situation it is easier to detect the effects of loop diagrams which proceed through Cabibbo-allowed transitions. Loop diagrams are dominated by the heavier exchanged masses and are therefore sensitive to the effects of higher flavours. The classic example was the hypothesis of charm and the estimate of the charm quark mass obtained from the study of $K \rightarrow \mu\mu$ and of the K_L - K_S mass difference well before the discovery of charmed particles.

B decays are favoured for three reasons: a) the larger phase space available allows many more final states then for K's, b) the ratio of loop to tree graph is controlled by the value of the relevant elements of the mixing matrix, and is proportional to:

$$|(V_{ts})^{*}V_{tb}/V_{cb}|^2 \approx 1 \qquad \text{for the B system}$$
$$|(V_{td})^{*}V_{ts}/V_{us}|^2 \approx 10^{-5} \qquad \text{for the K system}$$

and c) calculations of branching ratios for B decays are less affected by uncertainties on QCD corrections.

There are three types of "penguin" loop diagrams shown in Fig. 1, corresponding to the emission of a gluon, a photon or a Higgs particle. These give rise to charmless decays with strange particles in the final state, a good signature for our detector where hadron identification is excellent and where tertiary vertices can be found. Interesting final states which are likely to have a controllable background level in our experimental situation are: $B \rightarrow \phi K$ as an example of the elementary transition: $b \rightarrow s+$gluon, and $B \rightarrow Ke^{+}e^{-}$ as an example of an electromagnetic penguin. In both cases the branching ratios show a strong dependence on the existence of a fourth family of quarks. In the 3-family version of the Standard Model, they depend on the mass of the t quark and on V_{ts}.

The study of decay channels which can proceed through penguin quark diagrams is very important also in preparation for experiments to measure the violation of CP in the B sector. A necessary condition for the detection of CP violation in a decay channel is the presence of two amplitudes with different phases, leading to the same final state. It is the interference term between such two amplitudes that changes sign when one goes over from the decay channel to its CP conjugate, giving rise to a rate asymmetry. A possible way to have a second path to a final state is through a penguin loop (as is believed to be the case in $K \rightarrow \pi\pi$). A systematic search for these decay channels can give the key to an early discovery of CP violation in the B sector.

Another area, where the capability of accessing low branching ratio channels is important, is in the detection of decays resulting from $b \rightarrow u$ transitions. At present, there is evidence that this kind of decay might have been discovered at DORIS, yielding a surprisingly large value for V_{bu}. If this early discovery is not confirmed, our proposed experiment will have a good chance of detecting decays of the type $B \rightarrow p\bar{p}\pi\pi$ even if they occur at the 10^{-5} level.

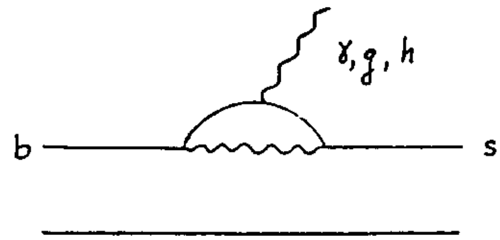

Figure 1: Penguin diagrams for B decays

Finally, a good sensitivity to rare decays will allow us to set limits on flavour-changing neutral currents, for example in the channel $\bar{B}^0 \rightarrow e^+e^-$.

We would like to stress the fact that we have only mentioned the highlights of the physics that can be studied with this detector, omitting areas (for example that of semileptonic decays) that are accessible to this experiment but might have been understood by the time we get our first results.

3. ACCEPTANCE & TRIGGER RATES

3.1 Acceptance

Fig. 2(a) shows the angular distribution in the laboratory of b and $\bar{b}$ quarks in a sample of gluon-gluon fusion events generated for $\sqrt{s}$ = 630 GeV $p\bar{p}$ interactions using the PYTHIA 4.8 Monte Carlo program[5]. In Fig. 2(b) is shown the corresponding distribution in pseudo-rapidity. Although the distribution of the decay products of the B-mesons themselves tend to smear out the forward peak, as is evident from part (c) of this figure, it is clear that a major fraction of the desired signal is found in the forward direction.

The curve labeled "All" in Fig. 3 shows the fraction of events in which all decay products of either B^0 or $\bar{B}^0$ are completely contained within the aperture of a single arm spectrometer in the forward direction as a function of the maximum angle of the spectrometer aperture, θ_{max}. The other curves in this figure show the same fraction except now demanding a momentum of at least the value (in Gev) which labels each curve for each track in the decay (for the purposes of this figure, charged particles and π^0's are treated identically). We choose θ_{max} = 600 mrad for our proposed detector. This yields a two-arm geometric acceptance of about 54% for B^0 or $\bar{B}^0$ (we discuss the loss of low momentum tracks below). This is summarized in Table 2, which also shows the overlap or correlated B and $\bar{B}$ acceptance given by the gluon-gluon fusion calculation in PYTHIA. Using the ISAJET generator, the geometrical acceptance for single B-mesons results in an acceptance ≈30% lower, while the correlated $B\bar{B}$ acceptance remains approximately equal to the PYTHIA result.

Table 2 shows that, of all $B\bar{B}$ events produced, the B is fully contained in the 600 mrad apertures 22 + 10 = 32% of the time. Of those B events fully contained, 10/32 = 31% of them also have the $\bar{B}$ contained. The same is also true for the $\bar{B}$. Clearly, if only a single arm spectrometer is constructed there is a loss of 50% of all statistics. However, it is expected that B and $\bar{B}$ mesons are rarely produced in opposite hemispheres so presumably no fundamental loss in physics would result.

Another loss of acceptance comes from the minimum angle cutoff, θ_{min}, which is an inherent characteristic of a forward collider detector due to losses in the beam pipe. Fig. 4 shows the geometric

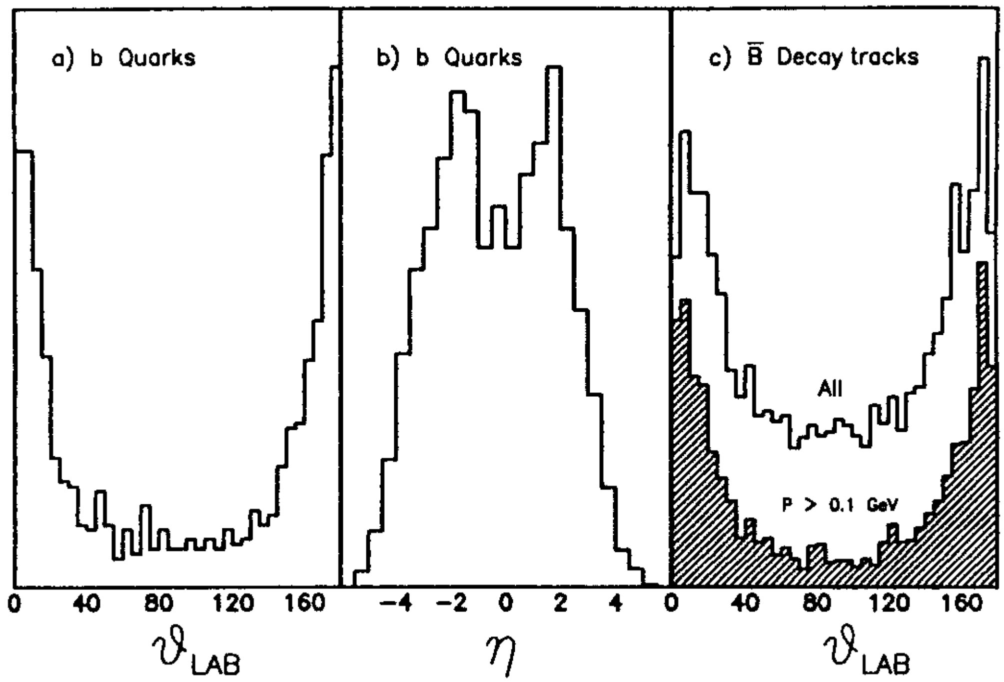

Figure 2: (a,b) θ_{lab} and η distributions for b quarks The production is via gluon-gluon fusion using the PYTHIA Monte Carlo event generator for $p\bar{p}$ interactions with $\sqrt{s}$ = 630 GeV. (c) θ_{lab}distribution of the decay tracks of B mesons. The shaded portion is the distribution of decay tracks with momentum greater than .1 GeV.

acceptance for a 600 mrad spectrometer, of the decay products of $\Lambda_b \rightarrow pD\pi\pi$ produced with momentum transfer p_t = 0.2 GeV/c as a function of the Feynman-x_F of the Λ_b for different assumed values of θ_{min}. We note that the properties of the curves are are essentially independent of the decay mode or even whether it is a B or Λ_b.

In Fig. 4 we see two major acceptance effects. At larger x_F (perhaps relevant for Λ_b, but not for B-mesons) and $\theta_{min} > 0$, the acceptance is seen to decrease because particles are lost inside θ_{min}. This loss increases with increasing θ_{min}. At small x_F, on the other hand, the second type of acceptance loss sets in, having to do with θ_{max}. Slower B's (or Λ_b's) tend to produce larger angle and lower momentum tracks. Thus, the minimum momentum cutoff plays a role here, an effect already seen above in Fig. 3 for B-Mesons which are generated predominantly with low x_F.

To further illustrate this point, we show in Fig. 5, the distribution of momentum of the lowest momentum B decay track from the $D^*3\pi$ decay mode. In Chapter 7 we discuss the offline reconstruction of this decay mode in more detail. We note that the requirements of the trigger and reconstruction tend to pick events which have relatively fast tracks so that a low momentum cutoff of ≈200 MeV would have much less effect on the acceptance of events which we can actually reconstruct than is implied by Figures 4 and 3.

We see from Fig. 4 that the θ_{min} choice for the spectrometer will weigh heavily on the acceptance of heavy flavor baryons, whose production will presumably not be confined to small x_F (we note

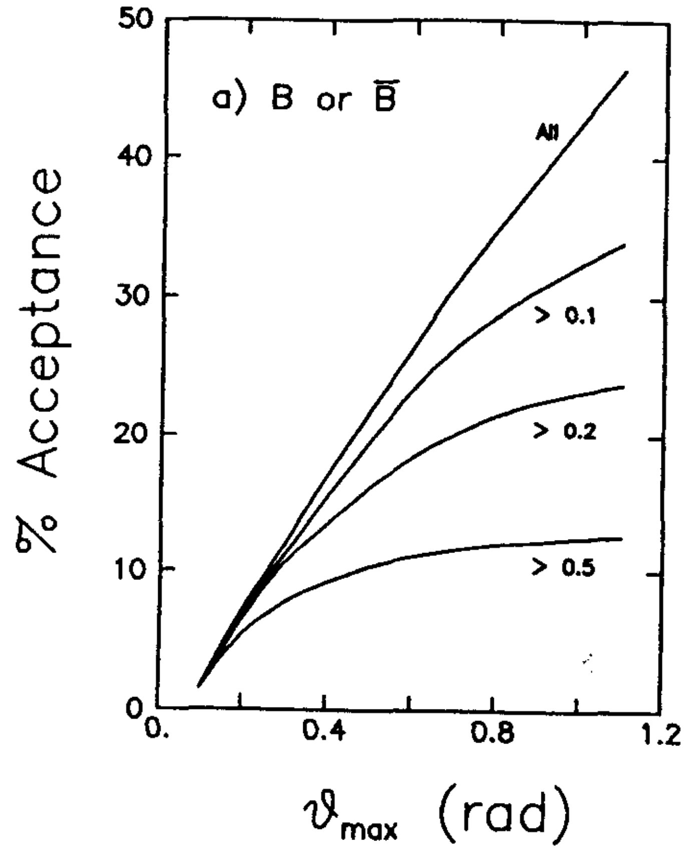

Figure 3: Single-arm B-Meson Geometric Acceptance vs. θ_{max}: A B^0 or $\bar{B}^0$ is assumed to be accepted if all the final state particles in its decay have laboratory polar angle less than the abscissa value of θ_{max}. The event sample used is the natural production and decay distribution of all $B\bar{B}$ mesons produced via gluon-gluon fusion in PYTHIA. θ_{max} is the spectrometer aperture. (the curves are parameterized by the minimum momentum (in GeV) accepted by the spectrometer).

that there exists ample evidence for large x_F production of the Λ_c[6]). We thus choose θ_{min} = 10 mrad as a reasonable compromise between physics and technical feasibility. The technical consequences of this choice are discussed below in Chapter 5.

The unshaded histogram in Fig. 6(a) is the momentum distribution of all B-mesons generated by PYTHIA according to the gluon-gluon fusion process at $\sqrt{s}$ = 630 GeV. The shaded histogram is the distribution only for those mesons whose laboratory angle, θ, is less than 600 mrad. Fig. 6(b) shows the momentum distribution of B-mesons which have been reconstructed as discussed in Chapter 7. We see that the B-Mesons inside the aperture of our spectrometer possess much larger momentum and are therefore much easier to measure, as pointed out in Chapter 1. Furthermore, our trigger and reconstruction algorithms have zero efficiency for B's with momenta below 10 or 12 GeV/c. Finally, we note that the mean flight path, $D = c\tau(p/m)$, is approximately 1 mm per 15 GeV/c momentum, as shown on the figure. Thus, the average flight path for our reconstructed B sample is about 2 mm. Our resolution in this quantity is less than 0.2 mm, as shown in Section 8.2.

Table 2: *Geometric Acceptance(a) for B and $\overline{B}$ Mesons*

	B yes	B no
$\overline{B}$ yes	10%	22%
$\overline{B}$ no	22%	46%

(a) Gluon-gluon fusion calculation by PYTHIA 4.8 for $p\bar{p}$ interactions at 630 GeV. B-mesons are considered accepted if all decay tracks fall within the 600 mrad aperture of either collider arm.

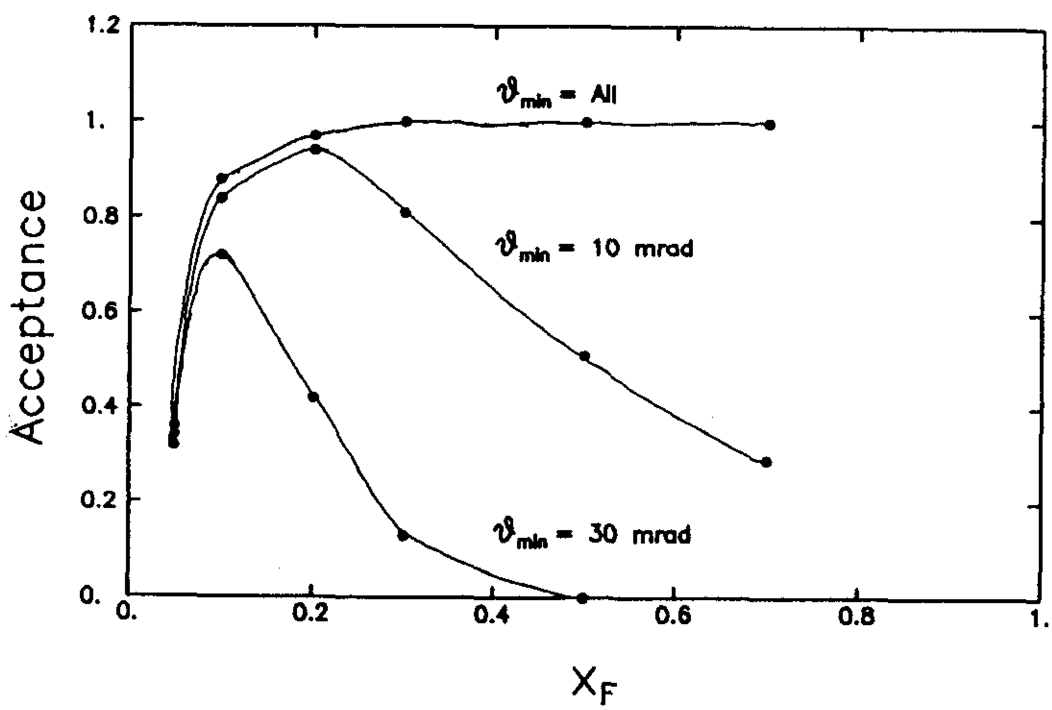

Figure 4: Geometric Acceptance vs. x_F and θ_{min} for $\Lambda_b \rightarrow pD\pi\pi$. For all but the upper curve, events are only considered accepted if all tracks have momentum larger than 0.5 GeV/c.

Fig. 7 shows the provisional layout of a Forward Beauty Spectrometer with θ_{max} = 600 mrad and with θ_{min} = 10 mrad. The various components are described below in Chapter 5.

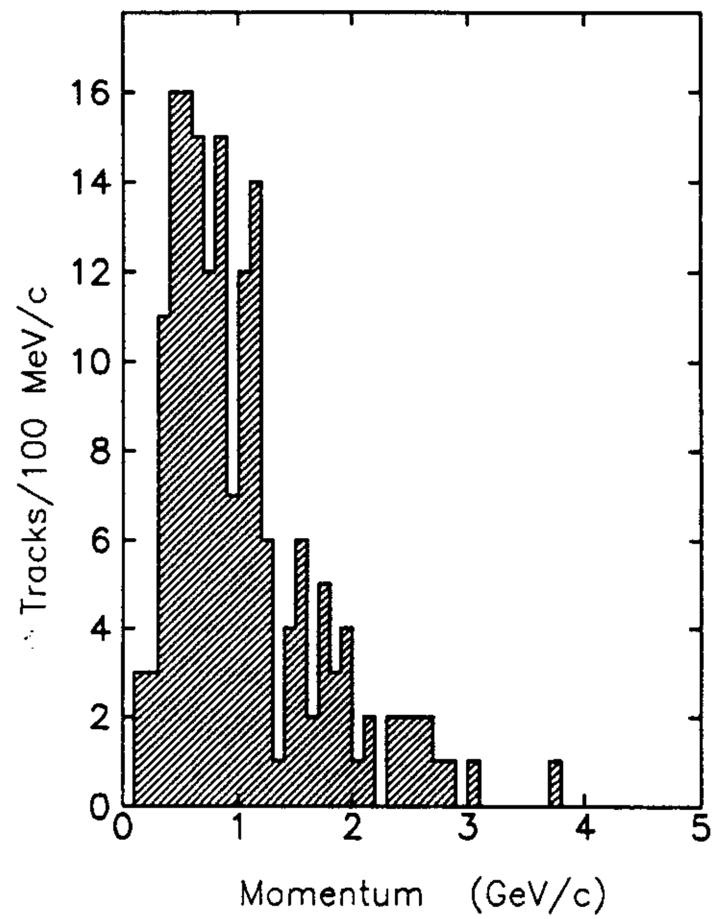

Figure 5: The momentum distribution of the lowest momentum track from the decay $B \rightarrow D^{*-}\pi^+\pi^+\pi^-$ with $D^{*-} \rightarrow \bar{D}^0\pi^-$ and $\bar{D}^0 \rightarrow K^+\pi^-\pi^+\pi^-$. This decay is further discussed in Chapt. 7.

3.2 Trigger Rates

We assume a $p\bar{p}$ total inelastic cross section of about 50 mb at $\sqrt{s}$ = 630 GeV and a cross section for $b\bar{b}$ production of $\approx$10 μb via gluon-gluon fusion. This leads to a ratio of total inelastic to $b\bar{b}$ events of $\approx$5000/1 and defines the level of minimum bias suppression which is required. Most of this is accomplished on-line, as discussed in Chapters 4 and 6. The remaining background is suppressed by the offline reconstruction procedure.

The expected trigger rates are shown vs. $Sp\bar{p}S$ luminosity in Fig. 8 for the individual trigger components: σ_{total} or Minimum Bias (MB), $b\bar{b}$ and $c\bar{c}$ events. For $b\bar{b}$ and $c\bar{c}$, the raw rate at a given luminosity is multiplied by the online trigger efficiency (discussed in Section 4.4) for that component. For example, $R(b\bar{b}) = \sigma(b\bar{b}) \times \mathscr{L} \times \varepsilon(b\bar{b})$, where $\sigma(b\bar{b})$ = 10 μb and $\varepsilon(b\bar{b})$ = 1/8 (note that, as discussed in Section 4.4, the trigger efficiency for those B-Mesons that are accepted by the spectrometer is much larger). We assume that the charm cross section, $\sigma(c\bar{c})$, is 10% of the total inelastic cross section, or 5 mb. In Section 4.4, $\varepsilon(c\bar{c})$ is shown to be 1/100.

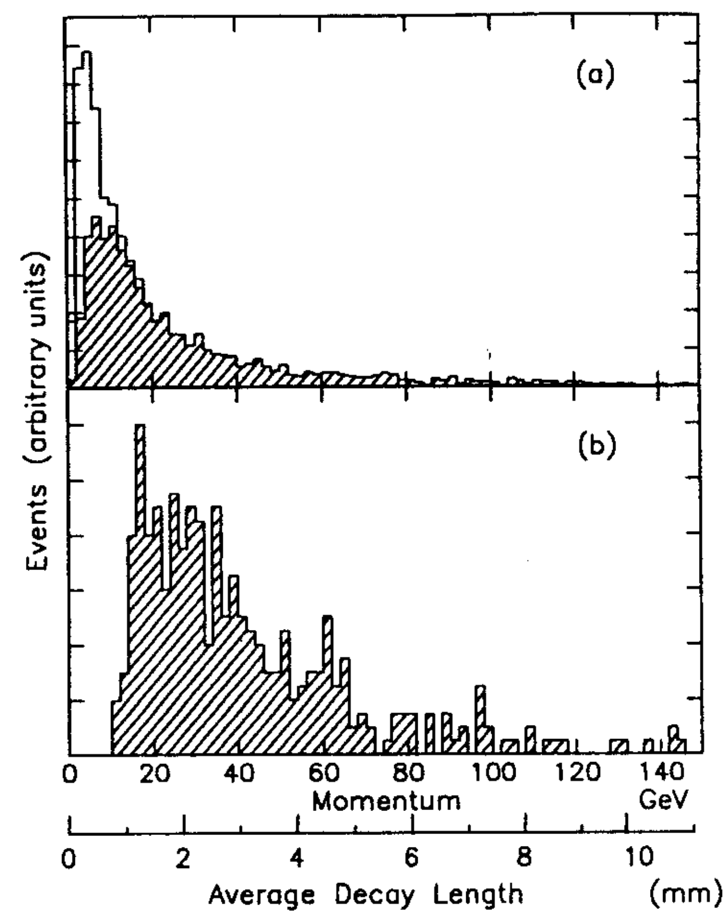

Figure 6: Momentum Distributions of B-Mesons. (a) Unshaded: All B-mesons generated according to gluon-gluon fusion; Shaded: Those with laboratory $\theta < 600$ mrad. (b) Those B-mesons which have been reconstructed and appear in invariant mass plots in Chapter 7. The distance scale shows the correspondance between the B momentum and its mean flight path in mm.

For the much larger total or minimum bias event rate, we consider separately those events which are alone in a bunch crossing ($n = 1$), and those for which there are multiple ($n > 1$) interactions[1] in a crossing ("pileup"). The $n = 1$ and $n > 1$ minimum bias rates are given by the bunch crossing rate (1/3.8 μsec) multiplied by the corresponding bunch occupancy probability of the Poisson distribution.

In the pileup case with 2 or more interactions in a crossing ($n > 1$ in Fig. 8), it is not unlikely[2] to find 2 vertices close enough to satisfy the trigger conditions discussed in Chapter 4. For this reason, Section 4.4 also contains the results of a simulation of the effect of the trigger algorithm on such $n >$

[1] The average number, $\bar{n}$, of inelastic interactions per crossing is given by: $\bar{n} = \mathcal{L}\,\sigma\,t$, where $\mathcal{L}$ is the luminosity, σ is the inelastic cross- section and t is the time interval between bunch crossings, 3.8 μsec. The number distribution of interactions per crossing (n) is Poisson: $P(n,\bar{n}) = (\bar{n}^n e^{-\bar{n}}) / n!$

[2] For example, M. Albrow has calculated that, with luminosities of 2×10^{30} and 4×10^{30}, the rates for bunch crossings which contain 2 or more interactions, whose vertices are separated by less than 1 cm, are 440 Hz and 2100 Hz, respectively.

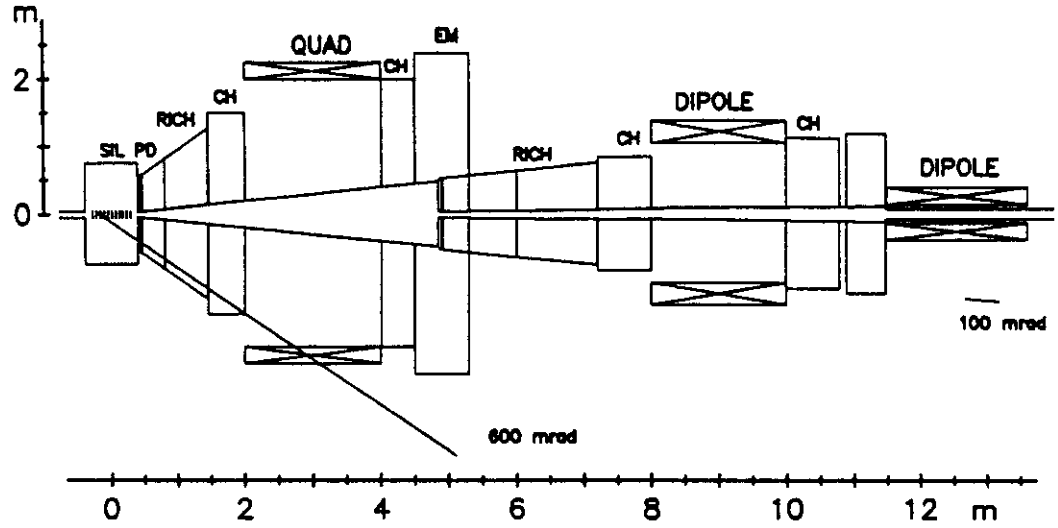

Figure 7: Provisional Layout of one Forward Beauty Spectrometer. The small dipole magnet at the end of the spectrometer, together with two dipole magnets on the opposite arm serve to compensate for the use of the large spectrometer dipole magnet.

1 events. A trigger efficiency, $\varepsilon(n > 1) = 1/60$, is found. For non-pileup events the efficiency is found to be $\varepsilon(n=1) = 1/500$.

Fig. 8 summarizes the results of these calculations as well as the summed rate of all components in the trigger. We see that, at the higher luminosity of 4×10^{30}, the pileup component overtakes the others and dominates the event sample which passes through the online Level-1 filter. Two points are to be noted, however. First, these pileup events can be disposed of offline. Second, the average luminosity for data taking is likely to be considerably lower. For example, if the $Sp\bar{p}S$-Collider is run 5×10^6 seconds during the year, it takes an average luminosity of only 2×10^{30} to reach 10 pb^{-1} integrated luminosity.

We conclude that, even with a running luminosity of 4×10^{30}, the total Level-1 trigger rate will not be larger than about 1 kHz. At this rate, two options are available for further data handling. The events can be passed into a parallel processor system for further analysis and selection or stored on a system of 8 mm Video cartridges, as discussed in Chapter 6.

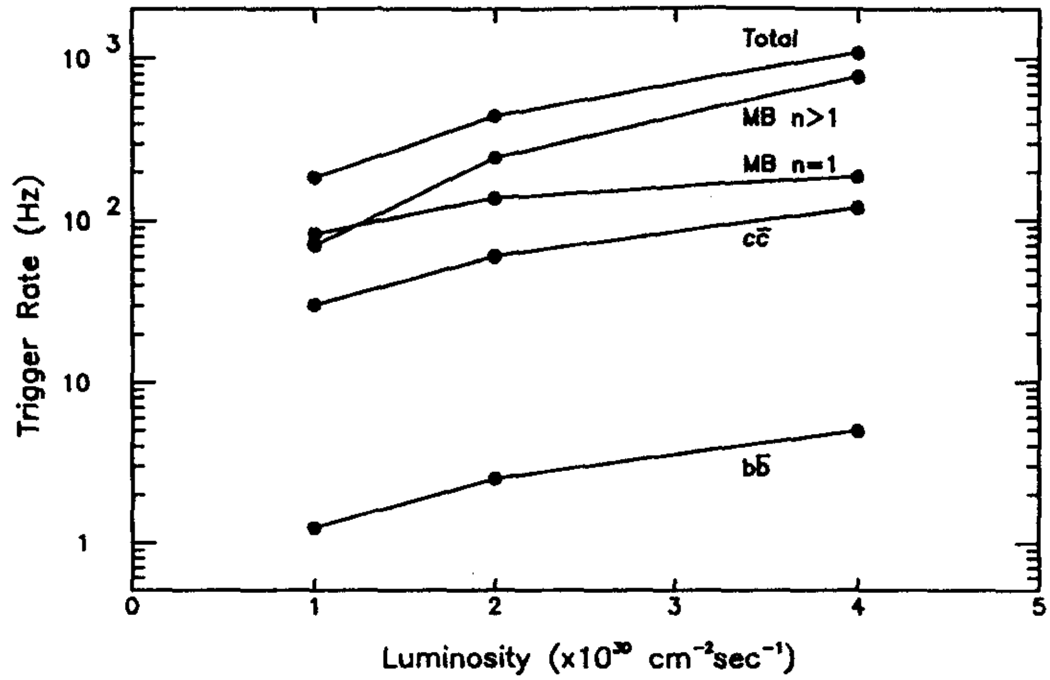

Figure 8: Trigger Rates (Hz) vs. Luminosity. Rates are given separately for . The rates are calculated based on the simulated efficiencies of the Level-1 Filter for each of these samples, as described in Section 4.4. The pileup ($n > 1$) and non-pileup ($n = 1$) components of the minimum bias sample are both shown as is also the total trigger rate.

4. TRIGGER & SIMULATION

Since the effectiveness of the trigger in suppressing the minimum bias background events is such an important aspect of our proposed experiment, we have studied the problem in some detail. As summarized in Appendix A, we have compared our minimum-bias event generator with UA5 results in order to be certain of its reliability. We have done a full simulation of the silicon detector response for these events and have created and tuned a trigger algorithm which has the desired properties (a minimum-bias suppression of 500 in the trigger with good efficiency for retaining the desired B events). The implementation of the trigger algorithm in hardware is discussed in Chapter 6.

The overall strategy of the trigger is to use only the silicon information to search for events which are inconsistent with having a single vertex. Before opting for this strategy, we looked for other properties of Beauty events which would allow a more rapid and easier-to-implement trigger, such as increased transverse momentum, higher mass in the forward direction or the presence of a high transverse momentum electron. We were unable to find any such cut which does not also entail an unacceptable loss in efficiency for Beauty events.

Requiring that an event be inconsistent with having a single vertex is clearly much weaker than requiring the presence of a secondary vertex nearby to the primary vertex. However, as shown below, this strategy results in a sufficiently large suppression of the minimum bias background to allow efficient transfer of accepted events either to a mass storage medium or to a processor farm where a more elaborate analysis can be applied. The algorithm sketched below is sufficiently concise as to allow easy implementation in the data-driven processor described in Chapter 6.

4.1 Silicon Micro-vertex Detector

The need to minimize the extrapolation distance from measured track points in the silicon to the interaction vertex has led us to a detector design in which the silicon planes are distributed along the intersection region as shown in Fig. 9(a). For the simulation, we have chosen a configuration consisting of 11 detector planes spaced 6 cm apart, so that all tracks which enter the spectrometer aperture of 600 mrad pass through at least two silicon planes.

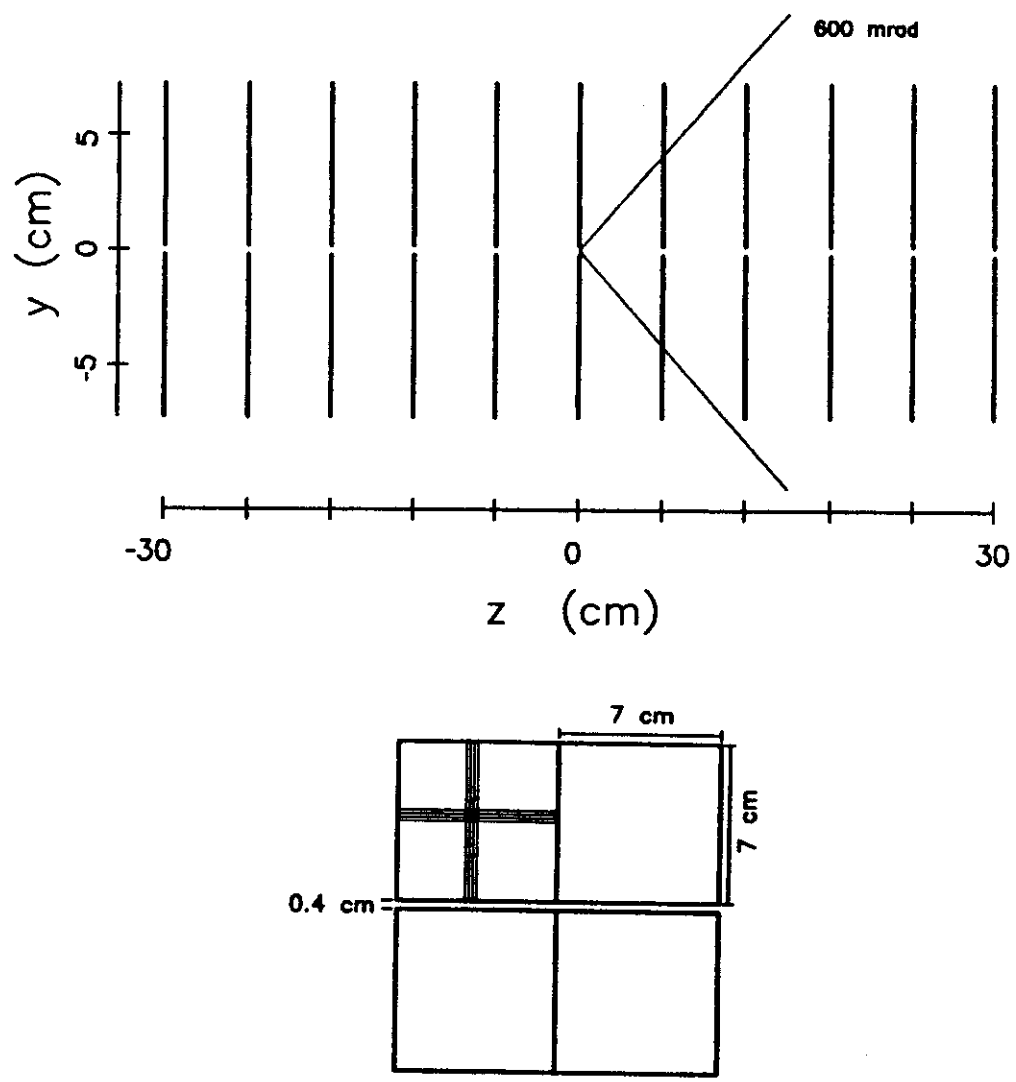

Figure 9: Silicon Vertex Detector Geometry

This choice of detector spacing involves a compromise between simultaneously minimizing the errors in extrapolating the tracks to an event vertex and the secondary interactions and photon conversions in the material of the detector. With 6 cm spacing, the extrapolation errors are dominated by the strip pitch of 25 μm for tracks with momenta above about 1 GeV/c. The combination of detector spacing and strip pitch is still under discussion and depends to some extent on manufacturing constraints.

With the 11 planes shown, the detector is sensitive to events which have primary vertices within ± 18 cm of the center of the interaction region. This entails a 19% acceptance loss. The addition of two more planes at ± 36 cm would reduce this loss to about 5%.

Each plane of the detector is divided into four independent 7 x 7 cm^2 silicon squares as shown in Fig. 9(b). Each silicon square is assumed to be a double-sided 25 μm pitch strip detector with 250 μm thickness, although two single sided detectors each with 150 μm thickness, which are presently available, would probably function as well. As is discussed below, in order to achieve faster readout speed of the silicon detectors, we do not plan to make use of the amplitude information in the signals, but only to use digital readout. We have opted for a strip geometry since it is not possible to read out a pad detector between beam crossings with present technology.

The 4 mm gap (± 2 mm) between the upper and lower detector halves allows for the passage of the beam. This is substantially larger than the machine aperture and should be adequate. New monitoring electronics for the currents in the low-beta quadrupole magnets and elsewhere will be necessary in order to dump the circulating beams in less than one turn should it be necessary for the protection of the silicon.

The sets of 11 upper and 11 lower detectors are each mounted on rigid but moveable supports which can be retracted during periods of machine filling (5 cm is said to be sufficient), and can be precisely positioned at ± 2mm from the beam for data-taking. The mechanics of the support system will make some use of the Roman pot technology which has been developed at the SPS. Fig. 10 shows a preliminary design sketch of one possible scheme. There is a double bellows system which allows the movement of the horizontal plate outside the vacuum tank to be coupled to the inner box.

From the experience of the Pisa group of Bellettini et al.[7], there are three problems with the use of silicon in vacuum. These are: (1) deterioration of the machine vacuum because of the use of unsuitable materials, (2) RF pickup in the silicon due to the passages of the beam bunches and (3) extracting the signals from the vacuum pipe. An elegant solution to these three problems has been suggested by Hartmuth Wahl of the SPS vacuum group. The idea is to enclose each silicon plane in a thin inner Beryllium envelope, as sketched in Fig. 10. The Beryllium serves not only as an RF shield but also as a means of isolating the ultra-high vacuum of the SPS from the effects of outgassing of materials in the silicon detector and also eases the requirements for the feedthroughs.

4.2 Silicon Data Simulation and Detector Response

In order to understand the properties of the silicon system, we have generated Monte Carlo event samples of different types (discussed below) using the Lund program, PYTHIA 4.8, imbedded in the CERN detector simulation Monte Carlo program, GEANT[1]. We have compared kinematical distributions of PYTHIA generated events with the corresponding distributions from UA5 data and have found reasonable agreement, as is summarized in Appendix A.

Silicon response data for the various classes of Monte Carlo events are simulated in GEANT. We have included the following effects into the generation:

- *Multiple Scattering:* We have tried both Gaussian and Moliere scattering. The Gaussian form results in a somewhat more pessimistic estimate of the trigger suppression for minimum bias events and we use it for the results presented below.

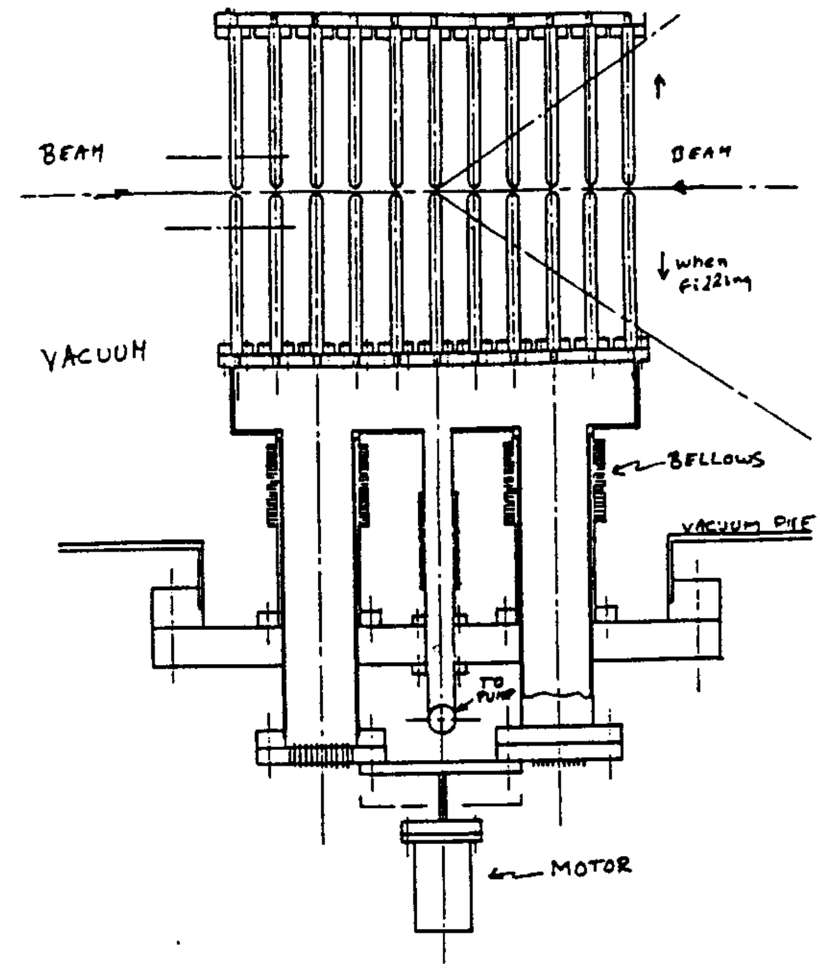

Figure 10: Sketch of the Vacuum Chamber and Silicon Positioning Mechanism

- *Nuclear Interactions:* We have tried both the Tatina and Geisha packages[1] but see little difference between the two. The samples discussed below were generated with the Tatina package.

- π^0 *decays:* π^0s are allowed to decay into either $\gamma\gamma$ or γe^+e^-.

- $\gamma \rightarrow e^+e^-$ *conversions in the detector:* Here, as above, the electrons are added to the track list and are followed through the detector as far as they go.

- δ-*rays:* Charged particles traversing the detector are allowed to generate electrons with energies above 10 keV, which are subsequently tracked until they stop.

The first step in generating the silicon response is to assign a quantity representing the amount of energy deposited in the detector by each charged track in an event. For example, Fig. 11 shows the distribution of energy generated for tracks with momenta greater than 10 GeV which impinge on the detector at normal incidence. The energy deposited by delta rays associated with the tracks is included.

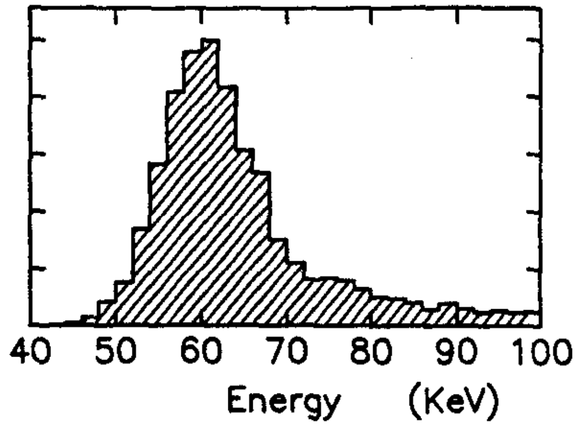

Figure 11: Energy Deposition in 200 μm of Silicon

The energy is divided between strips based on the path length spent in the depletion layer of each strip. Next, the number of electron/hole pairs is calculated assuming 270 pairs per KeV of deposited energy. Detector noise is accounted for by generating a normally distributed random number with a width (σ) of 1000 electrons and adding it to the signal. The resulting total charge is then compared to a threshold of 4000 electrons, and a yes/no response is generated for each strip. We have decided not to make use of pulse height information, since it is currently impossible to read out such information from a real detector at a high enough rate to satisfy the requirements of our on line trigger calculations (see Chapter 6). This algorithm results in a detector which is essentially fully efficient for tracks impinging at angles less than about 500 mrad, but rapidly loses efficiency for larger angle tracks.

4.3 Trigger Algorithm and Simulation

Fig. 12 shows the flow diagram of the proposed trigger. We describe each step of the algorithm in detail. We refer to a coordinate system in which z is along the beam direction, with x (horizontal) and y (vertical) perpendicular to z.

- *POINT FINDING:*

First, the raw silicon hit information is transformed into points independently in the xz and yz planes. The problem here is to dispose of the clusters (contiguous hit strips). Fig. 13(a) is the distribution of the number of contiguous hit strips generated in the Monte Carlo simulation. The average cluster width is 1.6 strips. A point is defined as the geometrical center of a cluster. A comparison of the points found in this way with the original track coordinates shows that they have a resolution of 16 μm (full width half maximum) as demonstrated in figure 13(c).

The distribution of the number of points per silicon detector (i.e. one quadrant of one plane) is shown in Fig. 13(b). Although the charged track multiplicity is high (see Appendix A), one quadrant sees on average, less than 1/8 of the total, resulting in the rather modest mean multiplicity of 2.5 points per quadrant.

- *TRACK FINDING:*

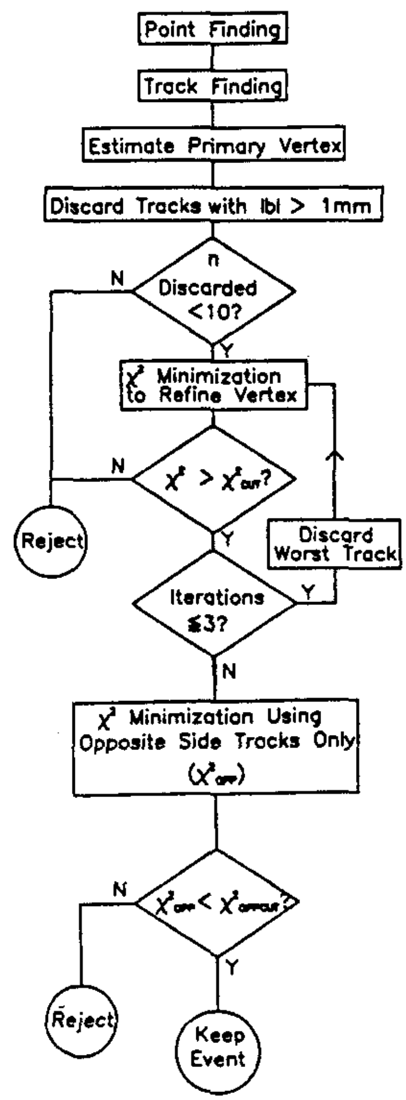

Figure 12: The Trigger Algorithm

Next, straight lines in both hemispheres, which traverse at least three planes of silicon, are found independently in their xz and yz projections. We demand that the points be collinear to better than $\pm 25\ \mu m$. This rather stringent cut corresponds to the multiple scattering of a 2 GeV/c track and thus tends to reject tracks with lower momentum which could degrade the vertex algorithm. Figure 14(a) shows the number of tracks found in the xz vs. yz projections using this procedure. The correlation is clear, although mainly because of the loss of lowest momentum tracks, there is a smearing. On average, the algorithm finds about 13 tracks in each view. Fig. 14(b) is a histogram of the number of particles which have traversed at least 3 detector planes minus the number of tracks found per event. As can be seen from this figure, the algorithm usually finds fewer tracks than are actually present (the

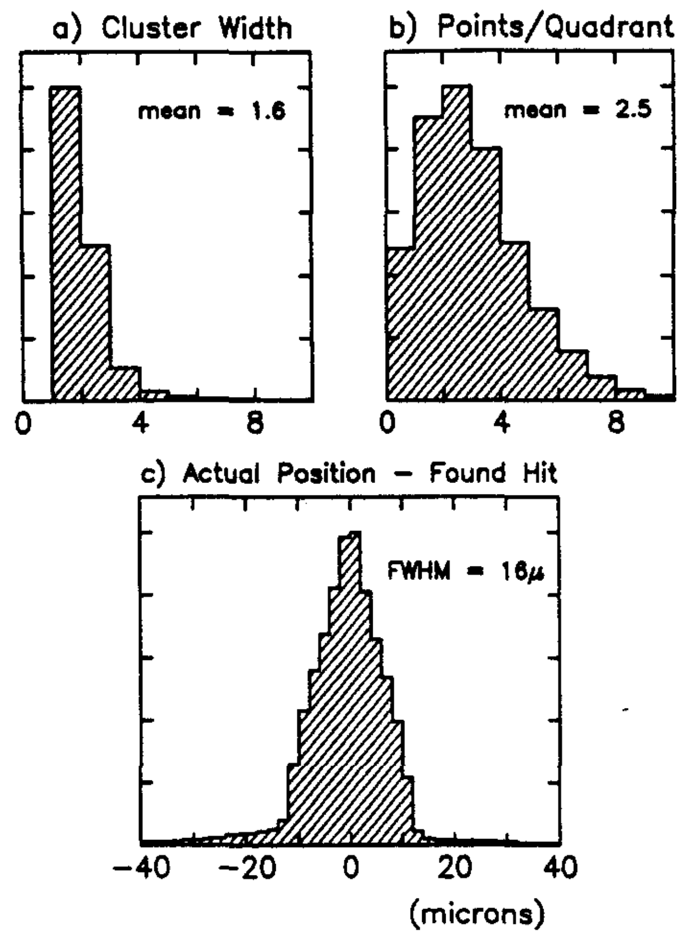

Figure 13: Point finding details

overall efficiency is about 80%) because of the loss discussed above of tracks with momentum less than 2 GeV which fail the collinearity test.

- *ESTIMATE PRIMARY VERTEX:*

We use the tracks found above to estimate the position of the vertex. As shown below, this step is mainly needed to define the subset of found tracks whose origins are near the primary vertex.

We histogram together in 5 mm bins the z intercept of all found tracks in both the xz and yz views. (We use only the two hits closest to the beam to estimate the track parameters.) A z-intercept histogram of a typical event from the minimum bias sample is shown in Fig. 15(a). Part (b) of this figure contains a histogram from a typical B event. For both events, most tracks are contained in two bins. There is seen to be very little difference on this scale between minimum bias events and B events.

We next loop over the histogram bins and find the two adjacent bins which contain the most hits. For our first estimate of the event vertex, we assume that the z coordinate is the average position of

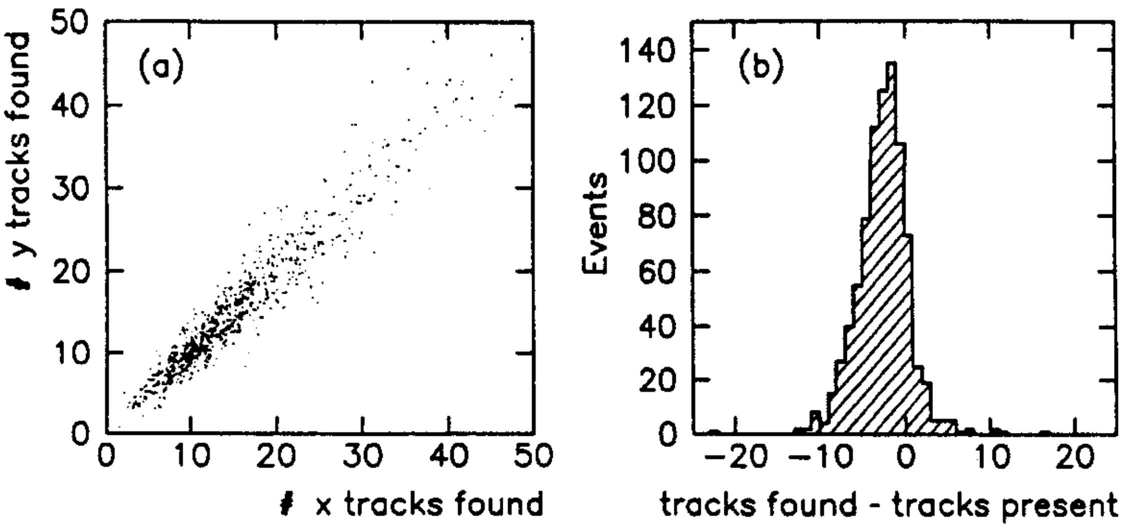

Figure 14: (a) The number of y-view tracks found, vs. number of x-view found. (b) the number of tracks found minus number of tracks present.

these 2 bins, weighted by the number of hits in each bin, and that $x=y=0$. Using this method, the vertex is located with a precision of 1 mm along the z axis.

- *EXCLUDE TRACKS WITH IMPACT PARAMETERS > 1 mm:*

This cut serves the dual purpose of discarding tracks which come neither from the primary vertex nor a B decay vertex (such as strange particle decay products or spurious tracks) and as a basis for rejection of pileup (multiple interactions in a bunch crossing) as is discussed below and earlier in Section 3.2.

We define the impact parameter as the distance between the point on the track at the z of the first vertex estimate and the z axis. Fig. 16 shows the impact parameter distributions for various classes of tracks. Fig. 16(a) is for tracks from the primary vertex only. Most of these tracks are in two 200 μm bins. Very few are actually outside the 1 mm cut. On the other hand, Fig. 16(b) shows that tracks from K^0 and Λ decay have a considerably broader distribution. Roughly half of all K^0 and Λ decay tracks are thrown out by this cut. The impact parameter distribution for tracks from B decays is somewhat broader than that of primary vertex tracks as can be seen in Fig. 16(d). On average the 1 mm cut discards about 1 more track from B events than from minimum bias events.

- *REJECT EVENT IF MORE THAN 10 TRACKS HAVE b > 1 mm:*

This cut is aimed at pileup suppression. Fig. 16(c) shows the impact parameter distribution obtained from Monte-Carlo generated double events (two minimum bias events in one bunch crossing). Except for the broad tail, the distribution is very similar to Fig. 16(a). The histograming method used to find the first vertex estimate usually picks out one or the other vertex when two events occur at the same time. The tracks from the found vertex are mainly in the $b=0$ peak, while the tracks from the second vertex form a broad background, also centered at $b = 0$.

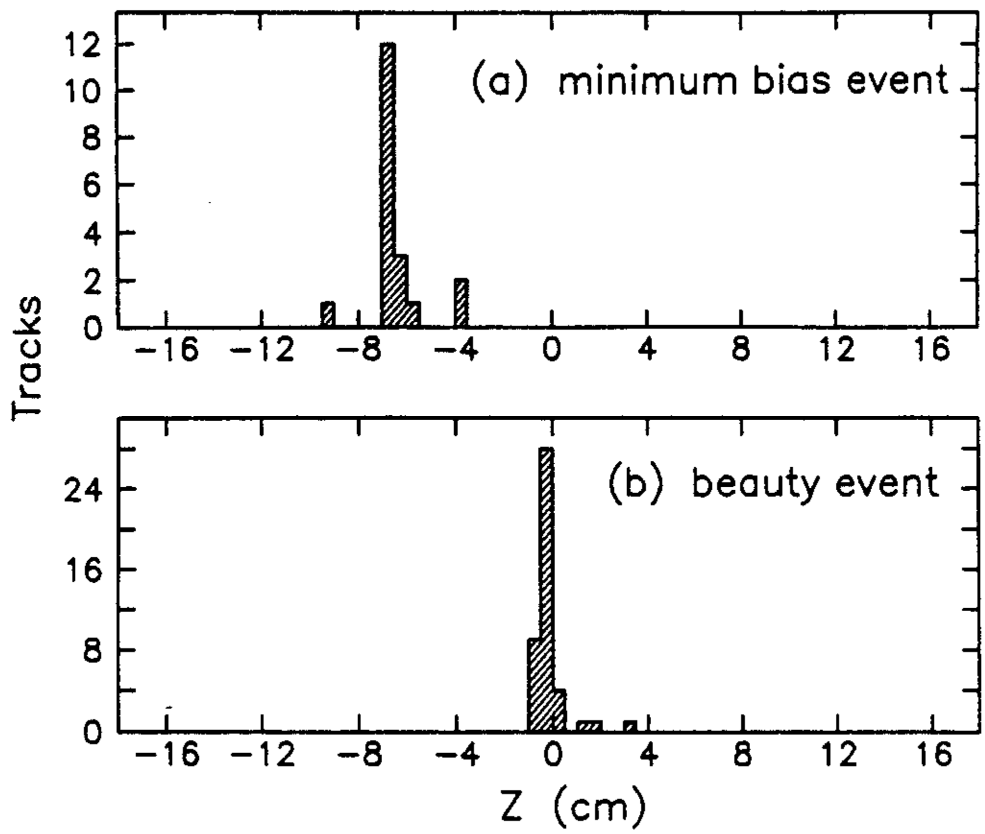

Figure 15: z-Intercept Distributions for (a) Typical Minimum Bias Event (b) Typical $B\bar{B}$ Event

Fig. 17 shows the number of tracks per event whose impact parameters exceed 1 mm for three classes of events. Demanding that fewer than ten tracks be excluded results in a loss of a few percent of B events while suppressing pileup by a factor of ten.

- *VERTEX FINDING BY χ^2 MINIMIZATION:*

Events which pass the above track cut proceed to the next phase which consists of refining the vertex estimate by minimization of the χ^2 given by:

$$\chi^2 = \sum_{i=1}^{N_x} \frac{b_{xi}^2}{\sigma_{xi}^2} + \sum_{i=1}^{N_y} \frac{b_{yi}^2}{\sigma_{yi}^2}$$

This equation contains independent sums over x and y view tracks. b_{xi} (b_{yi}) is the impact parameter of the i'th track in the x (y) view. Here, the impact parameter is the distance between the point on the track at the z of the vertex and the vertex point which is no longer constrained to be at $x=y=0$.

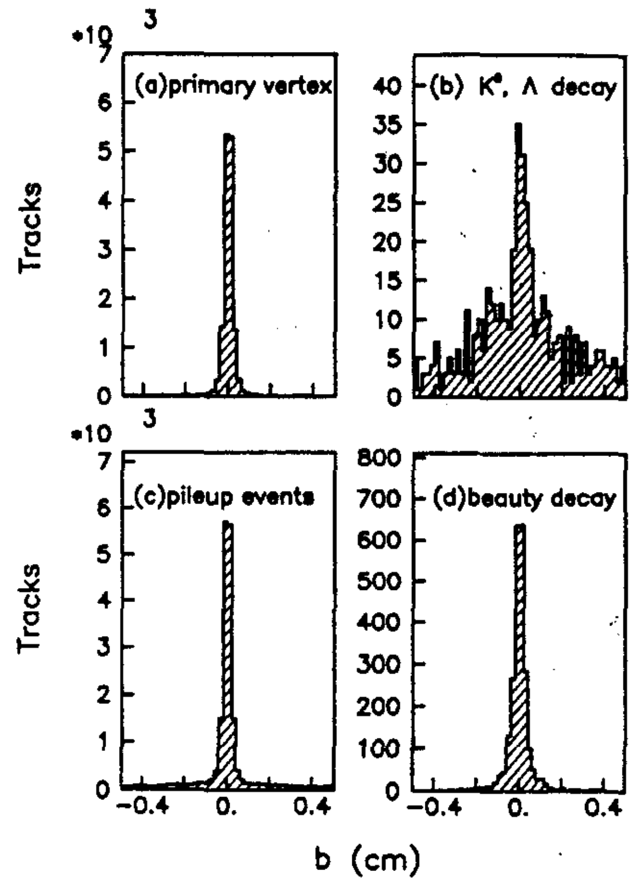

Figure 16: Impact parameter distributions (a) tracks from the primary vertex. (b) tracks from K^0 and Λ decay. (c) tracks from two superimposed events. (d) tracks from B-meson decay.

Track parameters are estimated using the two measured points closest to the first vertex estimate. A weight, σ_{xi} or σ_{yi}, is assigned to each impact parameter based on the track's slope (which gives a very rough indication of the track's momentum) and the extrapolation distance between the vertex and the closest measured point on the track.

Fig. 18 shows the χ^2/DOF (Degree of Freedom) distribution obtained from a sample of minimum bias events. The distribution is far from the ideal χ^2/DOF distribution. It peaks at $\chi^2/DOF = 4$ and has a tail extending to very high values. This is due in part to the presence of non-vertex tracks in the sum and to the rather crude estimate of track momentum that is used in evaluating the weight.

- *χ^2 CUT AND ITERATION:*

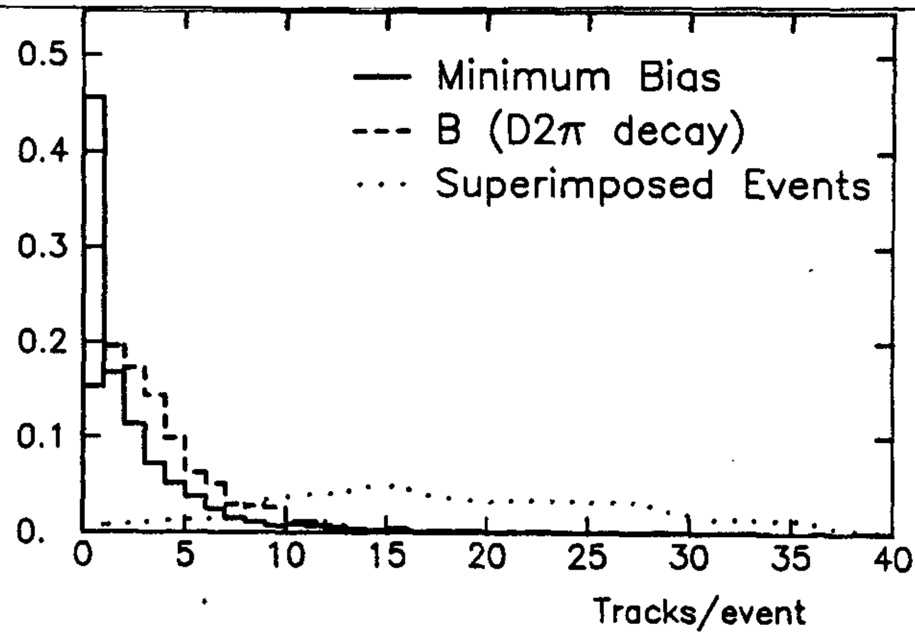

Figure 17: Number of tracks/event with impact parameter > 1 mm

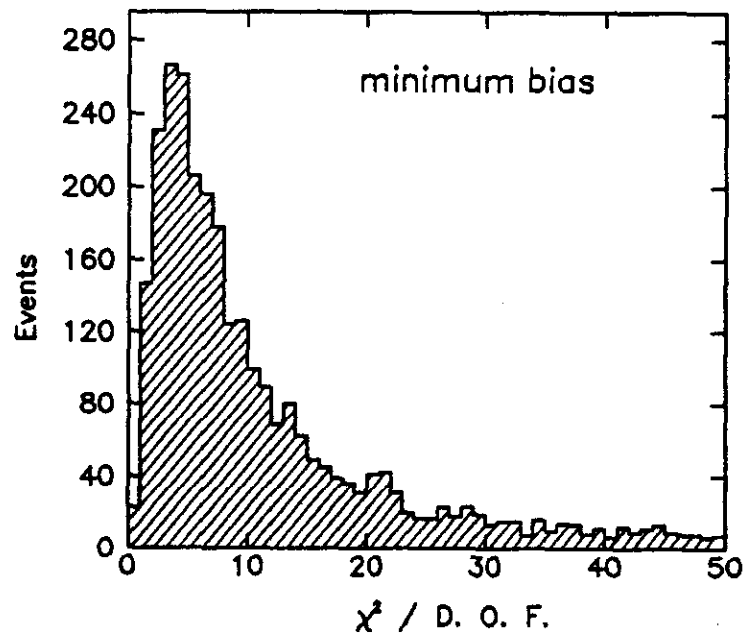

Figure 18: χ^2 *Distribution for Minimum Bias Events.* This χ^2 is obtained from the first minimization, before discarding worst tracks and iterating.

The χ^2-distribution shown in Fig. 18 with its very long tail (not shown) is insufficient to obtain the required suppression of minimum bias events without simultaneously rejecting an unacceptably large portion of the B events. However, we find that if we discard the track with the largest contribution to the χ^2 and refit, we can obtain substantially greater minimum bias suppression with acceptable additional losses of B events. The procedure is optimized by iterating and discarding up to 3 tracks. The results of applying this procedure to minimum bias, $b\bar{b}$ and $c\bar{c}$ event samples are shown in the next section.

Additional suppression of minimum bias events relative to B events can be obtained by using only the tracks which point in the hemisphere opposite the spectrometer and forming a χ^2_{opp}. The basic rationale behind this is the observation that if a B meson is produced and decays into the spectrometer, the accompanying $\bar{B}$ meson is very likely to be in the same hemisphere and therefore χ^2_{opp} should be small. However, a minimum bias event which happens to have a large χ^2 is equally likely to have its largest contributions from tracks in either hemisphere. Thus, an additional factor of two suppression should be obtainable by requiring that χ^2_{opp} is small. Moreover, since two superimposed (pileup) events with a large χ^2/DOF are likely to have a mix of tracks from both events going into both hemispheres, a χ^2_{opp} cut will yield a similar suppression here as well. Thus, for events which have a χ^2 larger than the cut value and which have at least 2 opposite-arm tracks in each view, we make one more iteration of the vertex minimization procedure, using only those tracks.

4.4 Trigger Performance

For each of the Monte Carlo data samples, minimum bias, $b\bar{b}$ and $c\bar{c}$, Figs. 19(a-c) show the trigger efficiency as a function of χ^2 cut for each of the four iterations and for the final χ^2_{opp} cut. By selecting events with χ^2/DOF larger than about 30, we see that we can achieve suppressions of 1/500, 1/8 and 1/100, for the three data samples, respectively. These are the values assumed in the rate estimates given in Chapter 3.

We note that the on line minimum bias suppression is only 1/500 out of a required 1/5000. However, from a Monte Carlo sample of 4000 minimum bias events, 8 events survive the trigger cuts described in this chapter. None of these events was found to contain a secondary vertex. We conclude that minimum bias background can be suppressed to the required level.

Although the trigger efficiency for the $b\bar{b}$ sample is 1/8 or about 12%, the effective efficiency for events in which a B-meson is accepted by the spectrometer is actually much larger since an accepted B meson usually has higher momentum and therefore a longer flight path than the "average" B meson and also since accepted events are unlikely to have B decay products in the hemisphere opposite the spectrometer and thus have a low probability to fail the χ^2_{opp} cut. This is demonstrated in Fig. 20 which shows the same trigger efficiency plot using a sample of a specific decay mode from Chapter 7 in which all the final state tracks are included in the spectrometer acceptance. We see that the trigger efficiency for these events is almost 50%, considerably larger than the 12% obtained for the entire $b\bar{b}$ sample. This is true in general for all modes which are actually accepted by the spectrometer although the level of acceptance depends on decay multiplicity as well as whether or not a D meson is produced in the decay. More will be said on this point in chapter 8, where several specific decay modes are discussed.

Finally we consider the effect of the trigger algorithm on pileup events. To accomplish this, we combine two events randomly from the minimum bias sample and pass the combined "event" through the trigger simulation software. Fig. 21 shows the results. First, we see that the zeroeth order χ^2 corresponds to an efficiency of about 10%. This is due to the approximately 1/10 suppression from rejecting events in which more than 10 tracks are discarded because their impact parameters are larger than 1 mm. Second, discarding the three worst tracks and imposing the χ^2_{opp} cut introduces an additional 1/6 suppression bringing the total suppression to 1/60. This the is value used in the rate estimates given in Chapter 3.

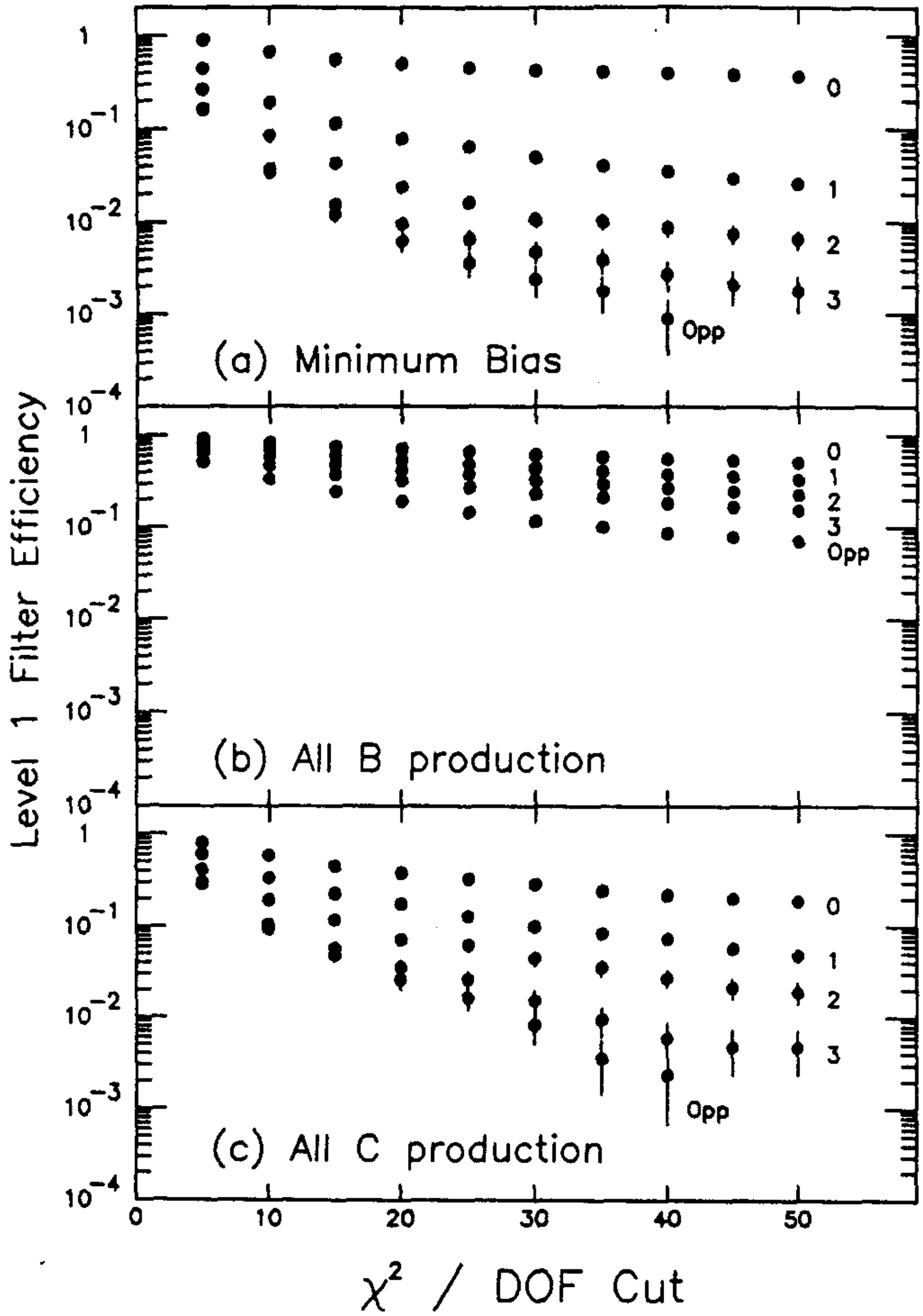

Figure 19: Trigger Efficiency vs. χ^2/DOF cut (a) minimum bias sample; (b) $b\bar{b}$ sample; (c) $c\bar{c}$ sample. The five sets of points correspond (from top to bottom) to discarding 0, 1, 2 and 3 tracks, respectively, which contribute the largest contributions to the χ^2 and, finally, imposing the cut on χ^2_{opp}.

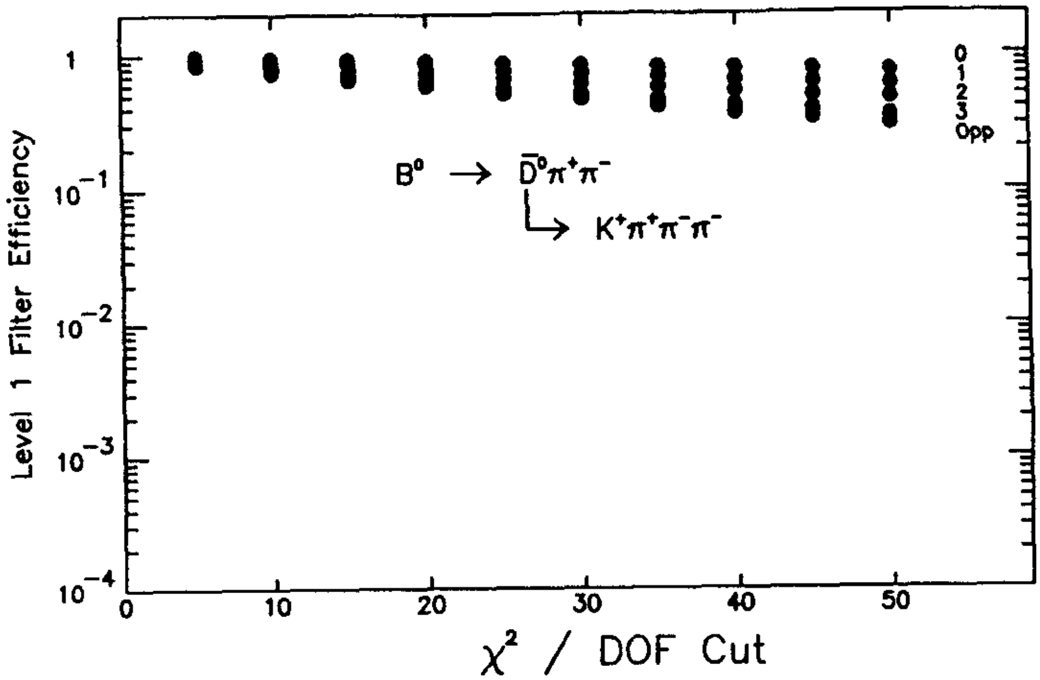

Figure 20: Trigger Efficiency vs. χ^2/DOF cut. The data here are 1000 examples of $B^0 \rightarrow D^0\pi^+\pi^- \rightarrow K^-5\pi$ generated according to gluon-gluon fusion but for which all final state tracks are contained within the 600 mrad aperture of the spectrometer, as discussed in Chapter 7.

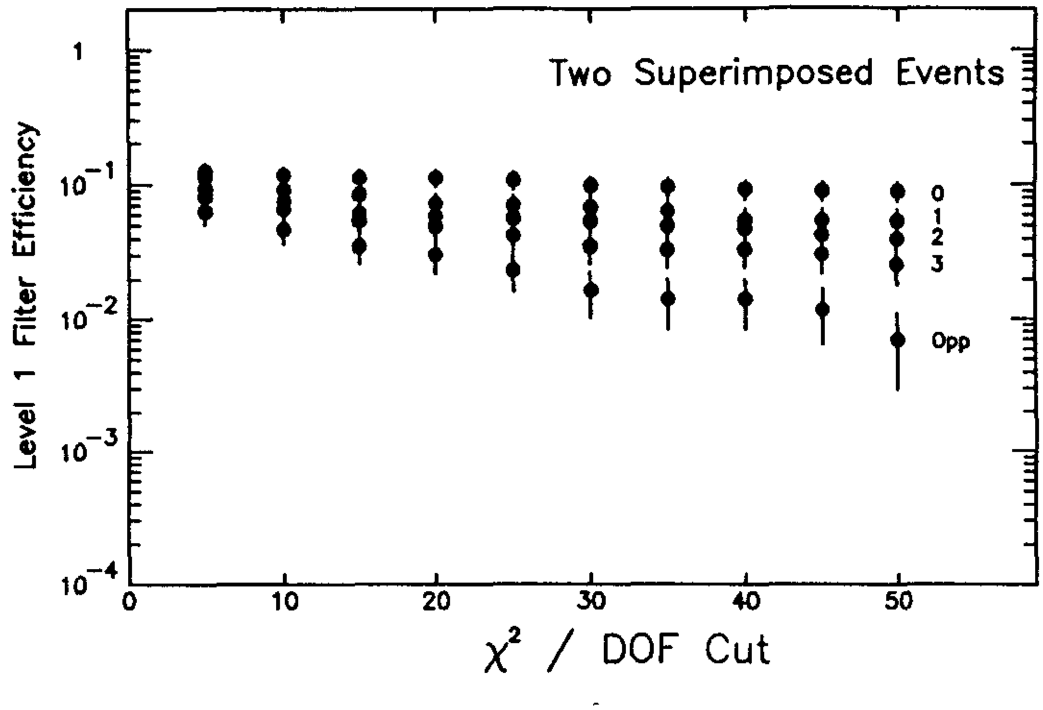

Figure 21: Trigger Efficiency vs. χ^2/DOF for Pileup Events. The data sample consists of a random addition of two minimum bias events to simulate a pileup situation in which there are two interactions in a bunch crossing.

5. SPECTROMETERS

The spectrometer layouts are shown in Figure 22 and Figure 23. The angular acceptance of Spectrometer 1 is from 100 to 600 mr, and for Spectrometer 2 is from 10 to 100 mr. The fractional solid angle ($\Delta\Omega/4\pi$) are 8.3% and 0.25%; for $B\bar{B}$ pairs produced within the 600 mr cone, the fraction of charged decay products contained in the detector is equal to 43% and 57% respectively for the two spectrometers. The fractions of $e^\pm$, $\mu^\pm$, $\pi^\pm$, $K^\pm$, and $p^\pm$ from accepted B decays are 6.2%, 6.2%, 68.1%, 19.1%, and 0.4% respectively. The charge multiplicity in hadronic decays of B mesons is 6.0$\pm$0.3 and in semileptonic decays is 3.8$\pm$0.4 hence for a fully contained hadronic decay of a $B\bar{B}$ pair we expect 12 charged particles and 10.5 gammas in the spectrometer in addition to the tracks from the underlying event. In spectrometers 1 and 2 about 95% of the pions are above 0.5 GeV/c and 5% are above 45 GeV/c, while for the kaons the momentum interval is between 1.5 GeV/c and 55 GeV/c.

5.1 Vacuum Pipe

The vacuum pipe contains two thin windows, one at z $\approx$30 cm and one at 475 cm, which correspond to the apertures of the two spectrometer segments shown in Fig. 7. A conical section with an angle of 100 mr connects the windows. The last vacuum pipe section after z = 475 cm is also a conical section, but with an angle of 10 mr, corresponding to the minimum angle of the second spectrometer aperture. Construction of the vacuum chamber from aluminum or carbon fibre (or both) will limit multiple scattering of the particles and reduce interactions of particles with material near the

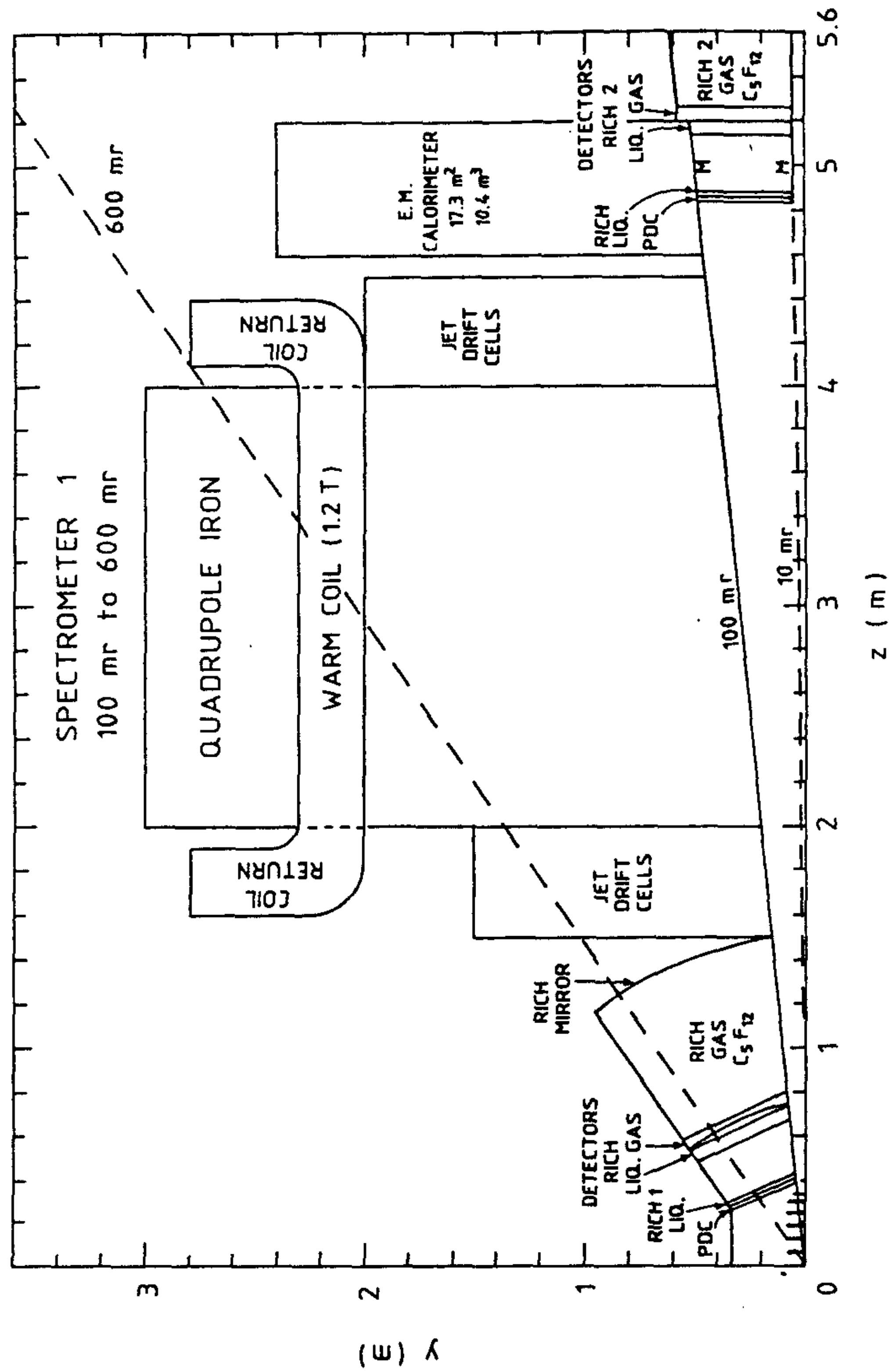

Figure 22: First spectrometer layout.

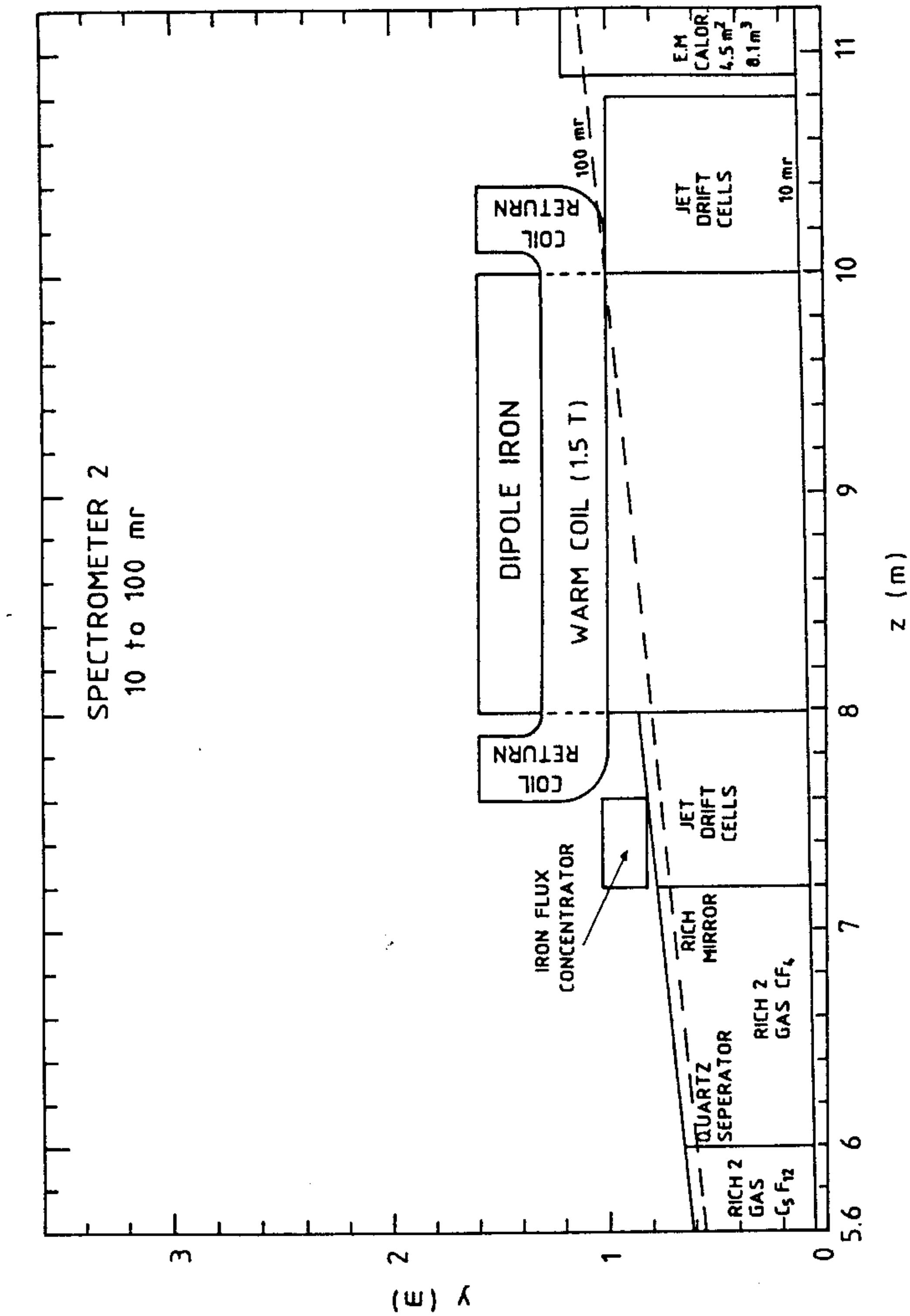

Figure 23: Second spectrometer layout.

beam. Both of these materials have been used successfully at CERN for construction of beam pipes. Recent improvements in aluminum welding techniques used at CERN make aluminum an attractive, cost effective material for the construction of these parts where the amount of material must be minimized. Although carbon fibre is more expensive, it could provide additional immunity to secondary interactions in critical areas such as near the window of the last spectrometer where the beam pipe reaches its minimum diameter (5 cm) in the spectrometer.

5.2 Magnets

The first spectrometer magnet, shown in Fig 22, is a normal conducting quadrupole magnet of 2 m radius and $L_1 = 2$m magnetic length (3m overall length) with a pole tip field of 1.2 T and a gradient of $B_1' = 0.6$ T/m. Several years ago, T. Taylor of the LEP division suggested to us the use of such a large aperture quadrupole magnet as an alternative to the large dipole spectrometer magnets with septum plates which he had previously designed for our experiments R603 and R608 at the ISR. A quadrupole magnet has the advantages that there is no material near the beam and, furthermore, that there is negligible field near the beam. This latter point is extremely important for us, in that we wish to have straight lines in our silicon detector, thus minimizing the complexity of the online trigger. The lack of material near the beam is extremely important to avoid interactions of outgoing particles.

The average $\int B_1 dl$ seen by a charged particle produced at the origin at polar angle θ is $<BL>_1 = B_1' L_1 z_1 \tan\theta/\cos\theta$ where z_1 is the middle z location of the quadrupole. The momentum resolution is given by $\sigma_p = kp^2$, where $k = \sigma_{\theta,b}/0.3 <BL>_1$, and $\sigma_{\theta,b}$ is the error in the bending angle θ which, for equal errors σ_θ on the incident and outgoing tracks, is given by $\sigma_{\theta,b} = \sqrt{2}\sigma_\theta$. For this quadrupole, $z_1 = 3$m, $L_1 = 2$m, $B_1' = 0.6$ T/m. Hence $k_1 = \sigma_{\theta,b} \cdot \cos\theta/1.08 \cdot \tan\theta$. The aperture covered by this quadrupole is 600 mr if a track sensitive detector is instrumented at the pole position (r = 2m) to detect particles which are deflected into the pole.

In the second spectrometer, covering 100 mr, as shown in Fig 23, a normally conducting dipole is chosen with magnetic length $L_2 = 2$m (geometrical length 3m) and uniform magnetic field of 1.5 T. The average $<BL>_2 =$ 3.0 Tm. The corresponding magnet constant is given by $k_2 = \sigma_{\theta,b}\cos\theta/0.9$. The sides of the dipole will be instrumented with a track sensitive detector in order to measure low momentum particles which are deflected by the magnetic field into the iron side wall.

5.3 Pixel Detectors

Three x-y pixel devices are included in the spectrometer to match the two views in the silicon tracks and to provided a middle measurement for use in matching tracks found by the vertex detector to those measured by the spectrometers. Two such detectors are needed to perform these functions for the second spectrometer since extrapolations over the 5m to the window of the second second spectrometer would result in large errors. Simulation shows that approximately 8% of all tracks lie within 1 cm of another track at the first spectrometer window, and about 4% at the window of the second spectrometer. This indicates that in order to effectively match tracks, the pixel resolution should be less than 1×1 mm^2.

The first drift chamber in the first spectrometer (100 mr $< \theta <$ 600 mr), shown schematically in Fig 22, is a pixel drift chamber (PDC) in which the two dimensional position of the track traversing the 20 mm thick gap is measured without ambiguity. The sense wires of the PDC are strung in an approximately radial (r) direction parallel to the outgoing tracks. The detector is approximated by an annulus of inner radius 4 cm and outer radius 32 cm (see Figure 24). The annulus is in turn approximated by an octagon with the sense wire array in the x direction (as defined in the figure). Each wire plane is 150 mm wide with 75 wires at 2mm spacing for a total of 600 wires. Two such arrays are needed per octant, to resolve ambiguities, for a total of 1200 channels. Outgoing tracks parallel to the sense wires (z) will produce ionization charge in the drift gap which will drift and, neglecting diffusion, trigger one wire only. The drift time $t = y/v_d$ and wire address (x) provide the unambiguous coordinates (x,y) of the track at the drift gap plane. Choosing 3 μsec as the maximum allowable drift time and a relatively fast ($v_d = 5.4$ cm/μsec) but low diffusion gas ($\sigma_\ell = \sigma_t = 180\mu m/\sqrt{cm}$) establishes the maximum drift distance $D = v_d \times t_{max} = 16$ cm. With wire spacing s=2 mm and 8-bit TDCs, the spatial resolution is $\sigma_x = 580$ μm and $\sigma_y = 180$ μm without diffusion. With diffusion, averaging over the 16 cm long drift distance, the pixel size increases to $\sigma_x = 750$ μm by $\sigma_y = 500$ μm.

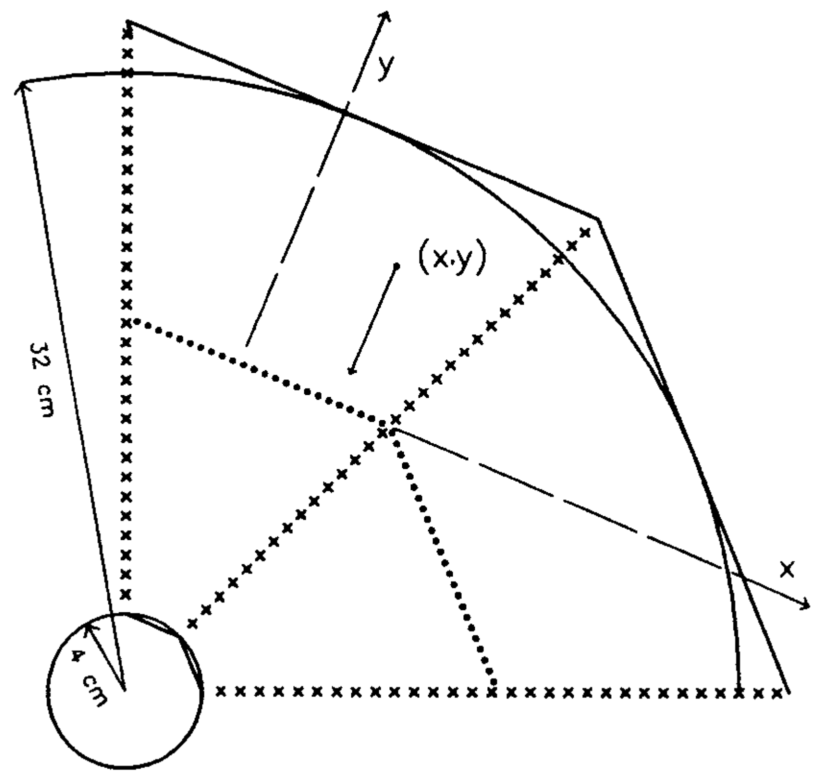

Figure 24: Front view of one quadrant of a pixel drift chamber. Circles are sense wires and crosses are potential wires. The second detector plane and the cathode planes are not shown.

A similar detector forms the first element of the second spectrometer (see figure 23), with a larger cylindrical radius of 48 cm. To keep the simple drift geometry of fig 24 will require 22 cm drift in 3μs or a drift velocity of 8cm/μs. Methane with about 10% ethane or isobutane can give the required velocity with somewhat increased diffusion ($\sigma_\ell = \sigma_\tau = 200\mu m/\sqrt{cm}$). The x resolution, without diffusion, is $\sigma_x = 580\mu m$ but $\sigma_y = 270\mu m$ because of the increased drift velocity. The resolution, with diffusion averaged over the 22 cm drift distance, is $\sigma_x = 850\mu m$ and $\sigma_y = 680\mu m$, sufficient to resolve ambiguities in track matching. The two arrays of wires in this detector total to 1700 channels, with unambiguous reconstruction. The total for the two PDCs is therefore 2900 sense wires.

Another pixel device will be used to match SVD tracks in the θ interval 10 to 100 mr. This will be a disk shaped Silicon Pad Detector located inside the beam pipe, at a distance of 35 cm from the average interaction point. It will allow coupling the track projections provided by the SVD and hence facilitating the match with the track segments reconstructed by the elements of the second spectrometer, which are 5 m or more from the interaction point. The SPD disk will be divided into four sectors, each covering approximately $\pi/2$ rad in ϕ. The upper and lower halves will be mounted on the respective vertex detector positioning mechanisms so they will also be removed during beam filling. The pixel size will be 1×1 mm^2, for a total of 11300 channels. The detector will have the shape of a disk with 6 cm radius, 250 μm thick.

Both track segments from the silicon detectors and from the spectrometer will be projected onto the pixel D.C. with spatial resolution better than 1 mm, in each projection, for momenta larger than 5 GeV/c.

5.4 Wire Chambers

Jet-type drift cells will be used to measure the position and direction of charged tracks before and after each magnet. Each chamber will be divided into 8 modules measuring the tracks in 3 (or 4) different views, and further subdivided into ±2 cm drift cells containing 16 (or 10) samples per module.

Drift Cell Structure

The drift cell geometry is shown in Fig. 25. The sense wires and equipotential wires are strung in planes which include the intersection region center ($x=y=z=0$). Thus, the average particle direction is perpendicular to the drift direction in all cells (implying a Jet-type geometry), so that isochronous charge collection will result. The wires will be staggered by 100 μm for unambiguous drift distance reconstruction. The maximum drift distance will be 2 cm.

We intend to use 70% Helium and 30% DME because of the long radiation length of this mixture (667 m) compared to that of CO_2 (197 m), while the diffusion characteristics and drift velocity are similar. This mixture results in an unsaturated drift velocity of 10μm/nsec in an electric field of 2 kV/cm with a diffusion coefficient of $\sim$80 μm/$\sqrt{}$cm. The corresponding maximum drift time is 2 μsec for ±2 cm cells. At atmospheric pressure this mixture will produce 21 primary electrons / cm. The wire spacing will be 6.25 mm, corresponding to 13 primary electrons per hit.

In order to estimate the resolution achieveable with these chambers, we note that the techniques proposed here are similar to those used by the NA-34 (Helios) experiment [8] at CERN and the SLD central drift chamber [9] at SLAC. The Helios chambers have a similar Jet-cell geometry and they used a CO_2 and 10% ethane gas mixture which gives a similar drift velocity to the He/DME mixture we propose to use. In order to optimize track separation and reduce space-charge, field wires were used to limit the length of the charge segment collected by a sense wire, obtaining a more isochronous charge collection. Their electronics made use of pulse clipping and shaping, and multihit TDCs. In a test beam, the chamber was found to have a resolution of 60μm averaged over the 2cm drift distance, and a 600μm two track separation.

The SLD collaboration used 92% CO_2 and 8% isobutane and a cell geometry which collected 16 primary electrons per sample. Their average drift distance resolution is 55μm in ±2.5 cm cells.

A drift distance resolution similar to those measured by these two experiments should be achieveable. However, since our chambers will have substantially larger dimensions and will operate in a nonuniform magnetic field, we infer a final accuracy of 100μm averaged over the drift distance, and a two track separation of 3mm. In order to reach such a precision, a laser alignment and calibration system will be used, together with a complete monitoring system of gas temperature and pressure, drift velocity, and electric field.

Geometry of the Chambers

Figures 22 and 23 shows the position and dimension of the four chambers used to measure the particle momenta. The four chambers all have a similar cellular structure. Chamber 1 and 2 in Spectrometer 1 are organized as a succession of 8 modules with 10 track samples each. Four different wire orientations are used, namely 0°, ±45°, and 90°. The sequence is repeated twice, ending up with a total of 80 measurements along each track. In Spectrometer 2 the chambers 3 and 4 are formed by 8 modules, each with 16 track samples, oriented as 0°, 45°, 0°, and −45° (from the vertical) repeated twice, for a total of 128 measurements, equivalent to 96 measurements in the bending plane. Table 3 gives a general overview of the properties of the chambers.

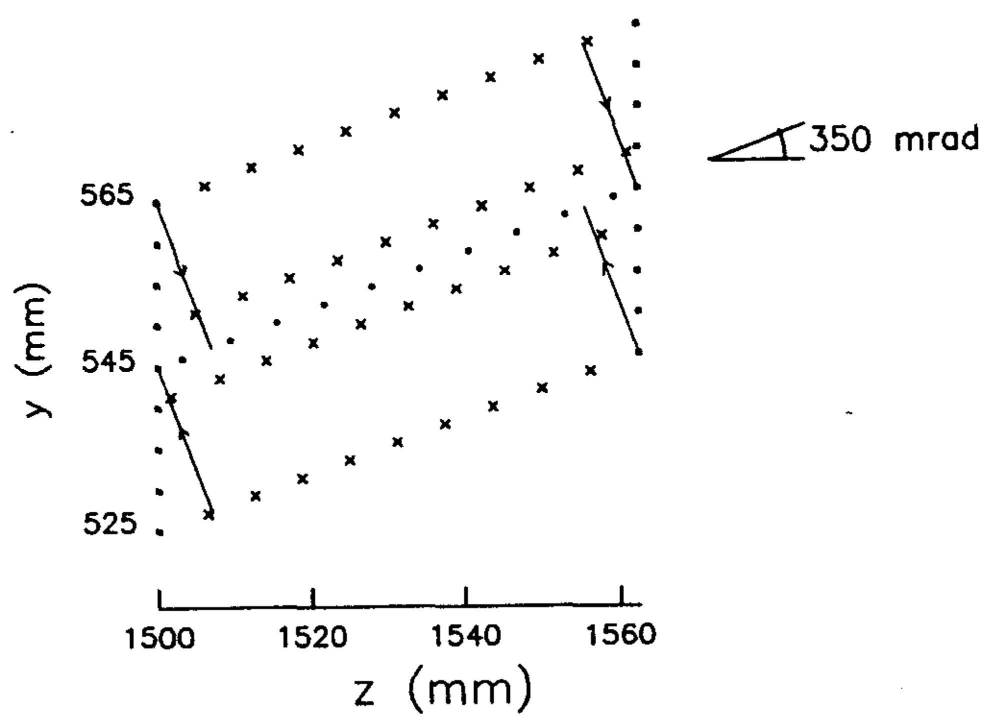

Figure 25: A Jet drift cell in one module of Chamber 1 at $\theta = 350$ mr. The circles are sense wires, crosses are equipotential wires, and squares are field shaping wires.

Electronics

A low noise preamplifier is mounted directly on the chamber frame. Ten meters away a two stage amplifier is used where a 2 nsec clipping and integration (1/t cancellation) is performed. A discriminater (with threshold set at 2 electrons on the sense wire) drives an 8-bit TDC with multihit readout. No pulse amplitude analysis is performed.

Momentum Measurement

The error in the track direction, θ, is given by the relation

$$\sigma_\theta = \sqrt{[(\sigma_x/L)^2(12N/(N+1)(N+2)) + (0.67\times.015/p)^2(L/X_0)]}$$

Table 3: Chamber Properties

	Chamber 1	Chamber 2	Chamber 3	Chamber 4
Diameter × Length (m^2)	3×0.5	4×0.5	1.6×0.8	2×0.8
Sense wires	7000	9600	5700	7100
Orientation	x,y,u,v	x,y,u,v	x,u,x,v	x,u,x,v
Samples per Track	80	80	128	128
Drift Distance	±2cm	±2cm	±2cm	±2cm
S.W. Staggering	100μm	100μm	100μm	100μm
Drift Velocity	10μm/nsec	10μm/nsec	10μm/nsec	10μm/nsec
Drift Field	2kV/cm	2kV/cm	2kV/cm	2kV/cm
Gas	He/DME	He/DME	He/DME	He/DME

where σ_x is the accuracy of a single drift cell measurement and L is the distance over which the uniformly distributed N+1 measurements are made and $X_0 = 667$ m for the He/DME mixture. In the dipole field (Spectrometer 2) we have 96 measurements (in the bending plane) over 80 cm of track length with a single hit accuracy of 100μm. With this geometry we obtain

$$\sigma_\theta = 44\mu r \sqrt{(1+p_2{}^2/p^2)}$$

where $p_2 = 7.9$ GeV/c is the momentum below which multiple scattering dominates. The error on the bending angle $\sigma_{\theta,b} = \sqrt{2} \times \sigma_\theta$ and the error on the momentum measurement is given by the dipole magnet constant $k_2 = \sigma_p/p^2 = 6.9\times10^{-5}\cos\theta\sqrt{(1+p_2{}^2/p^2)}$ for the 3 Tm magnet. (where we have used the expression for σ_p from Section 5.2) For Spectrometer 1 we have 40 measurements over 50 cm with 100 μm precision in the bending plane. Hence, $\sigma_\theta = 107\mu r\sqrt{(1+p_1{}^2/p^2)}$ with $p_1 = 2.6$ GeV/c. The quadrupole magnet constant is then $k_1 = \sigma_p/p^2 = 1.4\times10^{-4}\cos\theta\sqrt{(1+p_1{}^2/p^2)}/\tan\theta$.

A Monte Carlo simulation has been performed to evaluate the invariant mass distribution of the reconstructed B's using the properties of the spectrometer described before. The results for some decay channels of the beauty particles are described in Chapter 7.

5.5 Ring Imaging Cherenkov (RICH) Counters

Description

The RICH detectors for the spectrometers are designed to identify all the hadrons from B decays (≤50 GeV/c) as well as most of the leptons (≤10 GeV/c). Above 10 GeV/c, lepton identification will be guaranteed by the electromagnetic calorimeter. Each of the two spectrometers has a C_6F_{14} freon liquid radiator of 10 mm thickness and a C_5F_{12} freon gas radiator of 750 mm path length. In the second spectrometer we have left 1200 mm free for a higher threshold CF_4 freon gas radiator, although it is not yet clear that this should be implemented. The two gas volumes are separated by a 3 mm thick fused quartz window and both ring images are detected at the focal plane located 1950 mm upstream from the spherical reflecting mirror.

The liquid and gas radiator geometry is shown in Fig. 22 and 23 and the proposed RICH detector geometry is shown in Fig. 26. The liquid radiator is contained by a 3 mm thick fused quartz window followed by a 25 cm Helium-filled flight path to the RICH liquid image detector. This is immediately followed by the RICH gas image detector. Each detector consists of a 3 mm thick fused quartz win-

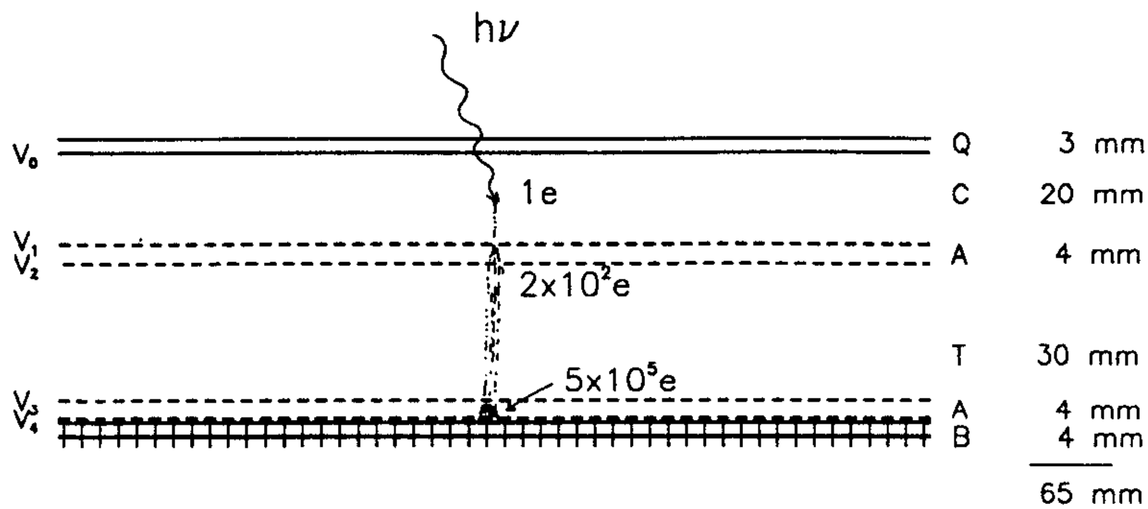

Figure 26: RICH Detector Geometry. A Cherenkov photon transmitted by the quartz window Q is converted in gap C. The primary photoelectrons are then amplified in gap A, before passing through gap T and being further amplified in the second gap A. The pad readouts cover the chamber body B. The average electron charge is indicated at various points.

dow whose inner surface is coated with a 20 to 30 Angstrom thick tungsten film which is UV transparent and serves as an equipotential surface V_0. A photon conversion gap of thickness t_C is defined by a first wire mesh plane at potential V_1. The thickness of the conversion gap is $t_C = 20$ mm which is equal to three absorption lengths ($\ell_{ph} = 6.7$ mm) when the photosensitive gas is TMAE at 40°C. This will require the entire detector and radiator ensemble be maintained at 45°C to prevent TMAE condensation in the detector. The conversion gap is followed by a 4 mm thick parallel amplification gap, a 30 mm thick transfer gap and a final 4 mm thick amplification gap. All gaps are separated by electroformed high transmittivity meshes on which are applied the appropriate potentials (V_1, V_2, V_3) to obtain electric fields of about 1 KV/cm in the conversion (C) and transfer (T) gaps and up to 10 KV/cm on the amplification (A) gaps. The gas filling is a mixture of Helium (90%) and Hexane (10%) and TMAE (1.7 torr) at 1 atmosphere total pressure. The conversion gap has an approximately triangular quantum response between 5.6 and 7.1 eV with the upper edge controlled by the transmission limit of Hexane. A total signal of about 5×10^5 electrons per incident photon is collected on one or more 3x3 mm^2 metallic pads which comprise the downstream cathode (V_4) of the second amplification gap. Each of these pads is read with a fast digital VLSI chip "RICHIP" [11] which is now in the middle stages of design. The total thickness of the RICH detector is 65 mm including quartz window and the detector body.

The RICH detector surface area is 0.9 m^2 in Spectrometer 1 and 1.1 m^2 in Spectrometer 2, for a total of 2.0 m^2 corresponding to 2.2×10^5 pads (3x3 mm^2) and pad readout channels. The use of the multistep avalanche amplification structure severely suppresses photon feedback effects and eliminates binning effects due to wires. The transverse radius of a single electron avalanche is expected to be about 0.6 mm. Hence it covers a surface area of 1.1 mm^2 compared to the 9 mm^2 surface area of a pad and results in an average of 2 pad hits per detected photoelectron. The readout electronics (RICHIP) has a fast (25 ns) analogue chain (Preamplifier, Amplifier, Discriminater, Delay + Memory) followed by a fast two dimensional digital shift register with priority encoding capable of readout of $2^6 \times 2^7$ pads in less than 3 μs.

Resolution and Particle Separation Ranges

The chromatic error $\sigma_{\theta c}(E)$ in the determination of the Cherenkov angle θ_c may be expressed as

$$\sigma_{\theta c}(E) = (\partial\theta_c/\partial n)(dn/dE)\sigma_E.$$

For the C_6F_{14} liquid radiator (refractive index $n = 1.278$ at $E = 6.5$ eV and dispersion $dn/dE = 9.28 \times 10^{-3} eV^{-1}$) the proximity focused image is characterized by (see Appendix C):

$$\partial\theta_c/\partial n = (n\tan\theta_c)^{-1}(n^2\beta^2)(\cos\theta_p/\alpha).$$

The first factor is the canonical factor obtained from the Cherenkov relation $n\beta\cos\theta_c = 1$, the second factor $n^2\beta^2$ is due to refraction at the liquid surface and the last factor $\cos\theta_p/\alpha$ depends on the particle incidence angle θ_p with respect to the normal to the radiator plane. α depends on the Cherenkov azimuthal angle ϕ_c via the relation:

$$\alpha = \cos\theta_p - \sin\theta_p\tan\theta_c\cos\phi_c.$$

Therefore, this last factor is unity for normal incidence and averages to 0.9 at $\theta_p = 20^0$. The energy error σ_E of a triangular response detector is $\Delta E/\sqrt{24}$ where ΔE is the base energy width. Combining these factors gives

$$\sigma_{\theta c}(E) = (1/1.02)(1.63)(.9)(9.28\times10^{-3})(1.5/\sqrt{24}) = 4.1 \text{ mr}.$$

At the chosen distance between the liquid radiator and detector (250 mm) the angular error σ_ℓ due to a radiator of thickness 10 mm is about $\sigma_\ell = 2.9$ mr when averaged over the accepted azimuthal angles ϕ_c. With pad dimensions of 3x3 mm^2 the measurement errors on the photon conversion point (x_1,y_1,z_1) are $\sigma_{x_1} = \sigma_{y_1} = .9$ mm and $\sigma_{z_1} = \ell_{ph} = 6.7$ mm and contribute to the angular error $\sigma_{\theta c}$ by the amount of 1.2 mr, 0.6 mr and 5.4 mr respectively. The image is approximately parabolic when $\theta_p \neq 0$. Hence, even for equal errors σ_{x_1} and σ_{y_1}, their respective contributions to $\sigma_{\theta c}$ are not equal. Multiple scattering in the liquid radiator and quartz window contribute 2.8 mr/p to $\sigma_{\theta c}$ and finally the contribution due to the incident particle direction θ_p is small, i.e. 0.7 mr for $\sigma_{\theta p} = 1$ mr. Summing, in quadrature, the above errors gives a total angular error $\sigma_{\theta c} = 7.5$ mr per detected photon.

The allowable average magnetic field inside a RICH radiator is

$$B < (\pi/2)\sigma_{\theta c}(tot)\sqrt{12p}/.3L$$

to insure that particle deflection inside the radiator does not cause additional smearing of the image. In the liquid radiator, $\sigma_{\theta c}(tot) = 7.5$ mr and $L = 1$ cm. Hence, $B < 8.7T$ at $p = 1$ GeV/c, which is clearly satisfied. The relevant derivatives are given in Appendix C and summarized in Table 4.

The momentum p at which particles of mass m_1 and m_2 are discriminated at the level of n_σ standard deviations is given by the formula:

$$p^2 = (m_2^2 - m_1^2)/(2n_\sigma k_c)$$

where

$$k_c = n\sigma_{\theta c}/\sqrt{(N_0 L)}.$$

Table 4: RICH Resolution

Measured variable	LIQUID RICH 1+2		C_5F_{12} GAS RICH 1		C_5F_{12} GAS RICH 2	
v_i	σ_{vi}	$\sigma_{\theta c}$(mr)	σ_{vi}	$\sigma_{\theta c}$(mr)	σ_{vi}	$\sigma_{\theta c}$(mr)
z (mm)	2.9	2.9	216.5	0.3	216.5	0.3
x (mm)	–	–	1.0	0.016	1.0	0.016
z_1(mm)	6.7	5.4	6.7	0.26	6.7	0.10
x_1(mm)	0.9	1.2	0.9	0.81	0.9	0.31
y_1(mm)	0.9	0.6	0.9	0.81	0.9	0.31
E (eV)	0.31	4.1	0.31	0.25	0.31	0.25
θ_p(mr)	1.0	0.7	0.5	0.35	0.5	0.35
TOTAL		7.5		1.29		0.69
k_c		1.18×10^{-3}		1.85×10^{-5}		9.88×10^{-6}

Experiments with the DELPHI barrel RICH prototype [12] have demonstrated ring images with 25 photoelectrons per liquid image (L = 1 cm), corresponding to $N_0 = 65$ cm^{-1} for the detector band base width $\Delta E = (7.1 - 5.6)$ eV. Taking $\sigma_{\theta c} = 7.5$ mr, $N_0 = 65$ cm^{-1}, L = 1 cm and n = 1.278 gives the Cherenkov constant $k_c = 1.18\times10^{-3}$. Hence, there is particle discrimination ($n_\sigma > 3$) up to momenta p = 1.25 GeV/c for $e\mu$, 1.65 GeV/c for $e\pi$, 1.1 GeV/c for $\mu\pi$, 5.6 for πK and 9.4 GeV/c for Kp.

The gas radiator in the first spectrometer consists of atmospheric pressure C_5F_{12} which has a Cherenkov threshold $\gamma_t = 17$ corresponding to momentum thresholds of 2.4, 8.4 and 15.9 GeV/c for pions, kaons and protons respectively. These thresholds overlap with the upper discrimination limits of the liquid radiator thus assuring complete coverage for particle identification in the low energy region.

The upper limits for particle separation in the gas radiator are determined by the Cherenkov angular resolution $\sigma_{\theta c}$ attainable. The relevant variables (v_i) are the photon emission point (z,x,0), the photon detection point(z_1,x_1,y_1), the photon energy E and the particle direction θ_p relative to the detector normal. The relevant derivatives are given in Appendix C. At zero impact parameter x (relative to the center of curvature of the mirror), the derivative $\partial\theta_c/\partial z$ varies between 0.2 μr/mm and 1.3 μr/mm for photon detection at the focal plane or 10 mm off the focal plane respectively. Since the error σ_z in photon emission point is large i.e. $\sigma_z = 750/\sqrt{12}$, the error $\sigma_{\theta c}(z)$ varies between 0.043 and 0.28 mr. For x≤50 mm $\sigma_{\theta c}(z)$ is ≤ 0.30 mr. The chromatic error $\sigma_{\theta c}(E)$ is ≃.25 mr for this radiator gas and detector. The impact parameter derivative $\partial\theta_c/\partial x$ is ≤16 μr/mm for x≤50 mm. Hence, for $\sigma_x = 1$ mm, the error $\sigma_{\theta c}(x)$ is ≤16 μr, which is negligible. The corresponding derivatives for the detected points are (for x = 0):

$$\partial\theta_C/\partial z_1 \simeq \sin\theta_C/2f$$
$$\partial\theta_C/\partial x_1 = \cos\theta_C\cos\phi_C/f$$
$$\partial\theta_C/\partial y_1 = \cos\theta_C\sin\phi_C/f$$

Thus for detection point errors $\sigma_{x_1} = \sigma_{y_1} = 0.9$ mm and $\sigma_{z_1} = 6.7$ mm we find corresponding angular errors

$$\sigma_{\theta C}(x_1) = \sigma_{\theta C}(y_1) = 0.81 \text{ mr}, \ \sigma_{\theta C}(z_1) = 0.26 \text{ mr}$$

in Gas Rich 1. The particle direction error is $\sigma_{\theta C}(\theta_p) = 0.35$ mr for $\sigma_{\theta p} = 0.5$ mr. Summing, in quadrature, all these seven error sources gives $\sigma_{\theta C}(\text{tot}) = 1.29$ mr. Multiple scattering in the C_5F_{12} radiator gas contributes a term $\sigma_{\theta C}(\text{m.s.}) = 1.55$ mr/p which is negligable at momenta above threshold ($p_\pi = 2.4$ GeV/c). The corresponding Cherenkov constant $k_C = n\sigma_{\theta C}/\sqrt{(N_0 L)}$ is equal to 1.85×10^{-5} for $N_0 = 65$ cm^{-1}, $L = 75$ cm, $n \cong 1$ and $\sigma_{\theta C} = 1.29$ mr. We then can calculate the 3σ momentum limits for particle identification as 10 GeV/c for $e\mu$, 13 GeV/c for $e\pi$, 9 GeV/c for $\mu\pi$, 45 GeV/c for πK and 76 GeV/c for Kp. This easily covers the range of particle momenta from B decays in the first spectrometer (95% of the π/K's are less than 12/15 GeV/c) and almost covers the range in the second spectrometer (95% of the π/K's are less than 45/55 GeV/c). The longer focal length (f = 1.95 m) in the second spectrometer's RICH reduces the detection point errors to $\sigma_{\theta C}(x_1) = \sigma_{\theta C}(y_1) = 0.31$ mr and $\sigma_{\theta C}(z_1) = 0.10$ mr giving a total error $\sigma_{\theta C}(\text{tot}) = 0.69$ mr. This translates to $k_C = 9.88\times10^{-6}$ and particle identification limits of 13, 18, 12, 60, 101 GeV/c for $e\mu$, $e\pi$, $\mu\pi$, πK, Kp respectively. The average magnetic field allowable in RICH 1 is B < 312 gauss × p, or 0.09T at 3 GeV/c (just above π threshold) and 0.3T at 10 GeV/c. The shielding of the quadrupole field at the position of RICH 1 (0.5m to 1.25m from the quadrupole entrance plane) appears feasible, since the field direction is azimuthal and can be easily channeled by iron plates mounted on the outer part of the RICH gas box. In RICH 2, with its better resolution, only 0.05T and 0.16T are allowable (at 3 GeV/c and 10 GeV/c, respectively). However, it is further away from the entrance plane of the dipole (2.0 m to 2.8 m i.e. 2.0 to 2.8 half gaps). However, the field direction is more difficult to shield and some loss of resolution seems likely at low momenta, where it is acceptable, since many σ's ($n_\sigma > 10$) are available for particle discrimination.

The momentum resolution of the RICH detectors is given by the relation, $\sigma_p = k_C p^3/(m^2\beta)$, where k_C is the Cherenkov factor calculated above. For example, $\sigma_p \leq 100$ MeV at $p_\pi \leq 4.7$ GeV/c and $p_K \leq 11.0$ GeV/c in the first spectrometer and $\sigma_p \leq 100$ MeV at $p_\pi \leq 5.8$ GeV/c and $p_K \leq 13.5$ GeV/c in the second spectrometer. It appears that for the heavier particles (K,p), the momentum resolution of the RICH detectors can be useful.

6. *DATA-DRIVEN TRIGGER PROCESSOR & DETECTOR READOUT*

The demands made on the readout system and trigger processor by the proposed experiment are particularly severe. The lack of an effective fast trigger criterion (one that can be calculated in less than the bunch crossing time) means that all detector information must be read out between bunch crossings, and stored until a more time consuming calculation can be completed. Moreover, the large number of computations needed for the trigger decision must be made in the shortest possible time, in order to minimize the number of events which must be stored, and by the fewest number of processors in order to minimize the complexity of the channel used to distribute the data from the detectors to the processors. Clearly, the obvious approach of using a farm of commercial μProcessors to make the trigger calculation fails both these criteria: a complicated network is necessary to route the data from the detectors to the μPs; and the milliseconds of processing time would require that thousands of events be stored while waiting for the trigger calculation to be made.

We propose to solve these problems by building both the readout system and the trigger processor with a pipelined structure. Data read from the detectors is transferred to FIFO memories in a very high speed data transport crate system. Meanwhile the silicon vertex detector hit data are entered into the first stage of a data driven processor. The data driven processor, which will be described in the following section, is itself a pipeline. Data entering the first stage is quickly processed and sent on to the following processor segment. This frees the starting set of processor modules for the subsequent event. The results of the trigger calculation are used to direct the transfer of data through the transport system. Events emerging from the transport destination modules are sent to a VME or Fastbus based data acquisition system for possible further processing as well as data monitoring and recording.

6.1 The Data Driven Trigger Processor

The on-line search of the silicon data for evidence of a secondary vertex requires the execution of some 10^4 instructions per event. These instructions must be performed at the average rate of one event per bunch crossing ($\approx 4\ \mu$sec). This implies the prodigious processing rate of 2.5×10^9 instructions per second, which is beyond the capability of even the most advanced general purpose supercomputers. However, such a rate is within the capability of a data-driven processor of the type used by Knapp et al. [2,3] and by the UCLA group for experiment UA8[4].

Data-driven processors differ fundamentally from the traditional Von Neuman processor in number of different respects.

- A Von Neuman machine is a general purpose machine, capable of performing (at least in principal) any calculation without the need for reconfiguring the hardware. A data-driven processor is built to perform a particular calculation. A change in the algorithm necessitates a change in the hardware.

- A Von Neuman machine is capable of performing only one calculation at a time, whereas a data-driven processor can easily be configured (parallelized) to perform a large number of calculations simultaneously.

- In a data-driven processor, instruction execution is initiated by the arrival of the necessary operands. This contrasts with the Von Neuman architectures where a predetermined sequence of instructions (a program) is followed. Thus, an algorithm written for a data-driven processor does not contain explicit information on the sequence of operations, but only specifies the dependence of the intermediate and final results on the input data and on the results of intermediate calculations.

A problem not resolved by Von Neuman computing is that of how to parallelize a computation. The basic problem is to find for every operation, the set of all prerequisite steps which must be performed and then to distribute the various operations among the available processing elements. In data flow processing, the problem of division of the algorithm and distribution of the tasks among processing elements is implicit in the algorithm. Thus, once the algorithm is written, the sequence of operations and the degree of parallelism becomes obvious.

Data driven processors may in fact exhibit any degree of parallelism from a single multifunctional processor with tables describing how quantities are combined, to one in which each of the modules which make up the processor executes a unique function and is interconnected with the other functional building blocks by dedicated data paths as necessitated by the algorithm. It is the latter case of maximal parallelism which will be used in the processor for the proposed experiment. This implementation has several advantages for use in triggering High Energy Physics experiments. Foremost among these advantages is the existence of many independent data paths. These allow the rapid transfer of large amounts of data while eliminating contention for a common bus and data transfer bottlenecks. Since intermediate results are not stored, there is no need for global memories and the usual problems of multiple access.

The UA8 trigger processor (described in detail in Appendix B), developed by the UCLA group, is a simple example of a data driven processor which nevertheless illustrates the power of data driven architectures. This processor uses 40 examples of a single module to calculate the momentum and intercept position of fast protons traversing the UA8 roman pot spectrometers. This calculation and the final trigger decision are made in less than 1.5 μsec of which only $\approx$600 nsec is used for the actual calculation. A programmed machine would have to execute some 2×10^8 instructions per second to equal this computational performance, even with heavy utilization of table lookup techniques. Also, the use of a programmable processor would require an additional interface to the chamber readout system which would further complicate matters.

The processor for the proposed experiment will differ from the UA8 trigger processor in two major respects. The first of these is that all of the functional units will operate on variable length lists of data, and produce lists of results. Examples of lists which will be used in a trigger processor are lists of hits found in a vertex detector, and lists of found line parameters. The list operators which may be defined include vector arithmetic and boolean functions (e.g. element by element addition, multiplication, AND, OR, etc...), and more specialized list processing functions (sort, append, element extraction, etc...). Conceptually, a list processor is little different from the basic processor used for UA8, although it greatly improves the flexibility of the architecture while reducing the number of functional elements needed for a given algorithm. This generalization requires that the interconnect protocol be enhanced to accommodate multiple elements. To accomplish this, the list is sent over a single synchronous data channel one element at a time. An end−of−data flag included in the interconnect indicates when all the list elements have been transferred. Vectorization has the additional advantage that the functional units may be internally pipelined to perform different parts of the calculation on different elements concurrently.

The second enhancement is the longitudinal segmentation of the processor to allow the simultaneous processing of different parts of several events. By dividing the processing into several segments, the time that an event occupies any single part of the processor is proportionally reduced. This in turn reduces the minimum delay between successive events (which is the effective processing time) and increases the utilization of individual functional units. The segmentation of the processor is sketched in Fig. 27. The silicon detector data are read into the first segment of the pipeline, which performs a set of operations on the data, and then passes the intermediate results to the next unit in the pipeline. The segmentation will be made fine enough that the average processing for a single event done by any segment takes less than the time between successive bunch crossings. Thus, a constant, unrestricted flow of events can be maintained through the processor while fully utilizing all the constituent elements of the processor. The segments will be decoupled from one another by pipeline registers (FIFOs) which store the result vectors from a given segment until the following segment has finished with the previous event.

Detailed design of a processor for the collider beauty experiment can not proceed until a careful functional simulation of the vertex finding procedure has been performed. Functional simulation involves the calculation from Monte Carlo events of the quantities which will eventually be calculated by the processor in the manner used by the processor. This will provide information about the numbers and types of functional units which will be necessary, the size of the lists which may be expected at each step of the process, and therefore the calculation speed necessary for a processor segment to complete work on a given event before the 3.8μsec deadline.

Some considerations are already evident. For example, given a clock time of the order of 10−20nsec, only 150−300 element list may be processed. On the other hand, for finding lines in a vertex detector, a list of all valid pairs of hits in two planes must be generated. Since the number of pairs goes as the square of the number of hits, an event with 20 hits in each plane would require a list of 400 elements although less than 20 would correspond to valid tracks. It is clear, therefore, that the processor must be able to perform the generation of these combinations in a way which would minimize the list size.

One module that could be used to solve this problem would be the Limited Combination Generator (LCG). This module has two sorted lists as inputs. The first list is used to calculate the two limits in which a number from the second list must fall in order to form a valid pair. For each entry in the first list, the LCG module calculates the limits and then searches the second list for an entry which falls within the limits. The search starts with the first entry which passed the previous comparison, and

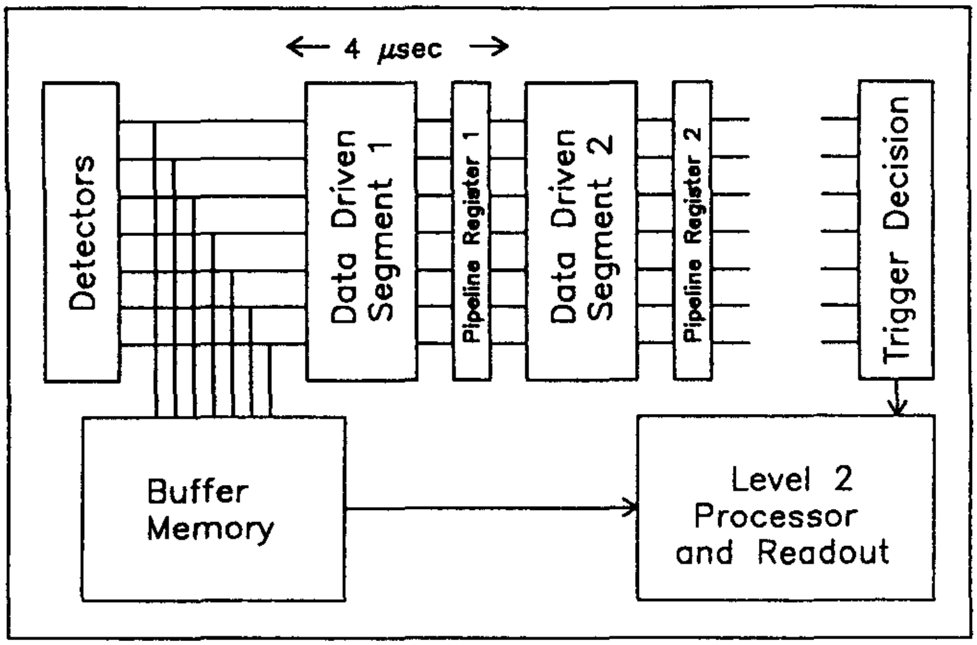

Figure 27: A Block Diagram of the Level-1 Filter System. The silicon data is read into the system of Pipelined Data-Driven Processors. The entire detector is read out on each bunch crossing into a large buffer memory where the data remain until the trigger decision is made. Events that pass the Level-1 Filter are transferred to the Level-2 Processor system.

proceeds until a element in the second list exceeds the current upper limit. A list of valid index pairs is produced at the output of the module.

Figure 28 shows how such a module could be used to find straight lines in three planes of a vertex detector. In addition to the LCG module, four other types of modules are needed:

- *Add (+):* The Add module adds its two input lists element by element.
- *Linear (α):* The Linear module multiplies each element of its input list by a constant and adds a second constant.
- *List (L):* These modules have two inputs. The first input is an arbitrary list. The second is a list of indices into the first list. The output of the list unit is the elements of the first list in the order specified by the indices in the second.
- *Sorter (SORT):* This module returns a list of indices which would sort the input list in ascending order.

The line finder works in the following way. Lists of hits in the first and second planes of the vertex are fed into the two lists of an LCG module. The limits calculated from the first list give the range of positions in plane 2 which could be reached by a track which originates in the dispersed interaction region and passes through the hit in the first plane. The index pairs are used to generate a list of plane 3 predictions by first using a list module to give lists of the first and second plane positions of the valid

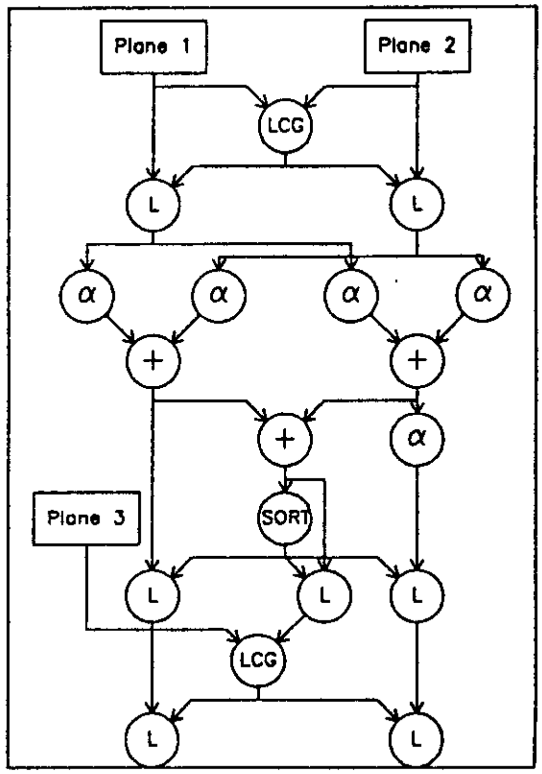

Figure 28: Block diagram of the data driven line finder.

combinations, followed by α and Add modules to extrapolate the line to the third plane. The predictions are sorted and sent to a second LCG module which matches the predicted values to the measured hits. Finally, lists of the line slopes and intercepts are produced by the list units controlled by the LCG.

Although the principles are similar to those of the Nevis Processor[2,3], a precision of 32-bits is needed for our vertex calculations. We also have a change in emphasis from optimization of the total speed to one of minimization of vector lengths at any given point in the processor. This new optimization criterion results from the requirement that the processing be segmented into units which may be executed in a few microseconds. Finally, the great advances in technology which have taken place in the last few years, particularly in the fields of Very Large Scale Integration (VLSI), and computer-aided design of Application Specific Integrated Circuits should allow the specification of some much more complex building blocks which will result in fewer system level interconnections, easier programming and lower overall cost.

Our program for developing this system proceeds along the following lines. A system emulator will aid us in evaluating proposed modules and the performance of the overall system when used as a trigger. It will also provide an exact cycle by cycle description of the hardware for module design studies. This will allow the specification of the set of 20 or so processor modules which are necessary to solve the stated problem. A system level design will be made in parallel with this study and the format of the module interconnections (including the data cables and a bus for diagnostics and table loading) will be defined.

Diagnostic software will be necessary to insure the proper operation of the processor and readout systems. From our experience with a data-driven processor in experiment UA8[4], the following types of diagnostic programs will be necessary:

- A detailed test program for each type of module.
- A program to verify the interconnections between modules.
- A data monitor.

6.2 Detector Readout System

Table 5 summarizes the quantity of data that will be read from each detector in a typical $b\bar{b}$ event. These numbers indicate the magnitude of the task faced by the readout system. Even assuming that the average occupancy per bunch crossing is one fourth of the typical B event sizes given below, the readout channels must sustain an average rate of 1.4×10^9 bytes/sec from the detectors. To achieve this total data transfer rate, many parallel data channels are employed. Detector digitizations are read out using sparse data scanning and zeros are suppressed where appropriate by the readout control electronics. High speed (50 MHz) FIFOs are used in most readout chains to average over bursts of data. Compacted and encoded data are sent from the experiment to the counting room over 1Gbit/sec optical fiber links.

Table 5: Detector Data Lengths

Detector	Elements	Occupation	Noise	Bytes
Silicon Vertex	264000	200	200	800
Tracking Chambers	29400	6240	500	13500
RICH	220000	1400	1000	5000
Pixel Drift Chambers	2900	50	50	400
Si Pixel Detector	11300	30	20	100

Total				19800

Data from the detectors is entered into digital pipelines (FIFO buffers) for storage until the trigger processor has completed its calculation. The FIFOs are imbedded in a synchronous data transport system which merges the many data streams from the individual detectors and fans out the resulting event block stream to consumers. Consumer modules in the Transport system make event data blocks available to the second level trigger, data acquisition, and detector monitoring subsystems.

Detector readout and other components will be built from Application Specific VLSI when possible in order to minimize the system cost and complexity. As is discussed in the following paragraphs, the development of VLSI readout electronics for the RICH and Silicon is already well underway. In addition to these chips, $1-8$ Chamber TDC channels could be integrated into an IC. Also, the extensive utilization of high speed FIFOs in the readout and data transport system makes the integration of such units an attractive possibility.

Silicon: The silicon detectors will be read out using a high density (128 channels per IC) VLSI chip which employs sparse data scanning to minimize the number of cycles needed to read the data. The Berkeley SVX chip[13], which was developed for the CDF silicon-strip vertex detector, would be well suited to this application, but the current version does not seem to be fast enough. It is hoped that this problem will be resolved in a future version of the SVX. The success of the present SVX, and other [14] chips gives us confidence that an IC which will meet our needs can be built within the time scale of this experiment.

The data readout from each plane will be controlled by a module which will also cluster the raw hits. This minimizes the number of hits which must be manipulated by the trigger processor.

Chambers: The chamber hit times will be encoded and recorded using a 8-bit, 10 nsec bin, multiple hit TDC system. In this system, each sense wire signal is tested every 10 nsec. If a wire has turned on in the last clock period, the time code is saved in one of two 4 word $\times$ 8-bit 100 MHz FILO stacks. At the end of the 3.8 μsec inter-bunch period, the data from the first stack are read back while hits from the next bunch crossing are being recorded in the second stack. Hit data from each chamber in the first spectrometer will be transferred over 20 parallel data streams, and those from the chambers of the second spectrometer will be sent over 32 other channels. Each of these channels will carry hit data from 4 wires of each cell in a given module. This division of data guarantees that each stream will carry approximately the same amount of data from every event.

RICH: The RICH photons will be detected on pad detectors which are segmented into 27 groups of 64 row $\times$ 128 columns for the purposes of readout. The detector signals will be amplified and shaped by a 16 channel VLSI chip currently under development. The discriminated signals produced by these chips are latched into a 50 Mhz shift register. Data readout proceeds by shifting out the hits a row at a time at a rate of 50MHz into a 128-bit row latch. Words which contain at least one set bit are latched in a second word from which the hit coordinates are encoded. The row number is given by counting the number of rows which have been shifted out, and the column number is determined by priority encoding. One hit is recorded and erased from the encoding register every 20 nsec until it is empty. Shifting of rows continues in parallel to the hit encoding unless a second non $-$ zero row is found while encoding of a previous row is still in progress. One or more additional row buffers may be added to decrease the likelihood of stopping the row shifting process.

Pixel Detectors: The Pixel Drift Chambers will be read out with the same sort of modules as are used for the tracking chambers. The silicon pixel detector will be read out with the same electronics as the silicon vertex detector.

Data Transport System: The data transport system is a crate oriented, 200 Mbyte/sec synchronous backplane through which all accepted events are passed. The extremely high throughput of this system allows the transfer of all accepted event data over a single channel, facilitating the dispersal of event data to acquisition, monitor, and high level filter processors. Modules connected to a backplane can be either data sources or data sinks. Each source module in turn transfers all the data for one event in a broadcast mode. Any sink modules which are enabled for the event may save the same event simultaneously. Multiple transport crates can be linked together in a tree structure for merging data from an arbitrary number of input sources or fanning out the data to an arbitrary number of destinations. A minimal programability will make it possible to configure the destination modules to select a subset of events.

6.3 Event Recording

Given a maximum event rate of 1KHz passing the level 1 (data driven processor) filter and assuming a 25% overhead in event size, the maximum data rate is 25 Mbytes/second. All events can therefore be written out to high bandwidth, high density digital video tapes.

Several such units are currently available including a low cost, low bandwidth (~250 Kbyte/sec) drive from Exabyte which writes 2 Gbytes of data on a cartridge, and a much higher bandwidth (~4 Mbyte/sec) drive produced by Honeywell which writes a 5 Gbyte cartridge.

While it is possible to store data at this rate, the sheer quantity of data as well as the enormous offline computing demands they represent, make such a solution unappealing.

An alternative solution would be to use a farm of high performance microprocessors to perform complete track reconstruction and to reject some of the more common false trigger sources such as some classes of pileup or strange particle decays. The second level event selection criterion would involve a tradeoff between the desire to keep as many events as possible to maintain good efficiency and to limit the difficulty in correcting for this stage of filtering, and the practical necessity of minimizing the total event sample. We expect that by using relatively simple selection criterion, which would reject > 50% of the triggers coming from pileup and minimum bias events, we will be able to reduce the 1kHz level 1 trigger rate to the level of 300 Hz.

Because of the jet-cell structure of the tracking chambers, and multiple bending views through the magnet, track reconstruction of even high multiplicity (30-40 track) events is relatively simple. We estimate that full track reconstruction of an average event can be completed in less than 100 msec of CPU time. An additional ~60-100 msec (equivalent to 1 second VAX CPU time) is available to select from completely reconstructed events.

The level 2 processors would be organized into ~8 farms, each containing of order 20 processors. Decision of the processor to be used and therefore the exact number needed will depend on the progress in a rapidly changing field, but we expect that by the time the experiment is approved, we will have a choice of 10 − 20 MIPS RISC architecture processors. Each farm would be located in an standard bus (e.g. Fastbus or VME) which transfers event data at a rate of at least 10 Mbyte/sec. The farms are fed by interface modules from the transport system.

7. RECONSTRUCTION OF B-EVENTS & BACKGROUND

In order to understand the problems of B-meson reconstruction, we have written software to search for the following decay modes:

$$B^0 \rightarrow D^{*-}\pi^+\pi^+\pi^- \rightarrow ((K^+\pi^-\pi^-\pi^+)\pi^-)\pi^+\pi^+\pi^- \quad (1)$$
$$B^0 \rightarrow \bar{D}^0\pi^+\pi^- \rightarrow (K^+\pi^-\pi^-\pi^+)\pi^+\pi^- \quad (2)$$
$$B^0 \rightarrow \psi^0 K^0 \rightarrow (e^+e^-)(\pi^+\pi^-) \quad (3)$$
$$B^0 \rightarrow p\bar{p}\pi^+\pi^- \quad (4)$$
$$B^0 \rightarrow \pi^+\pi^- \quad (5)$$

We generate event samples containing B^0 mesons using PYTHIA in the context of the CERN program GEANT, as described in section 4.2. In addition to the decay tracks from the B and $\bar{B}$ states, Pythia generates an underlying event which is similar in structure to a minimum bias event. In order to estimate the combinatoric backgrounds under the signals, we use the $b\bar{b}$ Monte Carlo event samples described in Section 4.2, in which the B and $\bar{B}$ mesons decay inclusively.

In the generation of the exclusive decay modes, events are retained only if all the decay products of the B^0 meson are inside the spectrometer aperture of 600 mrad. These events are then passed through the simulated online filter, as described in Chapter 4. Those events which survive are then used in the reconstruction analysis.

Before proceeding to the vertex-finding and event reconstruction, we first generate track parameters. Unit vectors describing track direction and position are derived either directly from the full silicon detector simulation, for tracks which leave at least two hits in the silicon, or are simulated by randomizing the generated Monte Carlo tracks in accordance with the assumed spectrometer resolutions. Momentum measurement errors are simulated by randomly varying the generated Monte Carlo momentum, also in accordance with assumed spectrometer resolutions. We assume that the RICH counters correctly identify all tracks and that x/y view matching as well as track matching between the spectrometer and silicon detector is done without error.

The vertex-finding algorithm consists of the repeated application of a vertex search among tracks that do not come from previously found vertices. First, a vertex is found using all available tracks. If the vertex χ^2/DOF is unacceptably large, the track with the worst contribution is removed and the process is repeated until either the χ^2/DOF becomes acceptable or only one track is left. If a vertex is found with this procedure, tracks which are used in the vertex are flagged and removed from further consideration. This vertex finding procedure is repeated until either no new vertex is found or the number of unused tracks is less than two.

The vertex-finding procedure is common to the analysis of all of the above final states. After the vertices have been found, each individual final state is handled separately. By way of illustration, we describe in detail the procedure used to isolate $B^0 \rightarrow \bar{D}^0 \pi^+ \pi^- \rightarrow K^+ \pi^- \pi^- \pi^+ \pi^+ \pi^-$.

We start by calculating the invariant mass for each $K^+ \pi^- \pi^- \pi^+$ track combination which is consistent with having a common vertex. For combinations with a mass near to that of the $\bar{D}^0$, we loop over the remaining $\pi^+ \pi^-$ pairs in the event which have a common vertex which is at least 500 μ downstream of the primary vertex but no further downstream than the $\bar{D}^0$ vertex. Finally, we reconstruct the momentum vectors of the B^0 and $\bar{D}^0$ and require that the $\bar{D}^0$ momentum vector be collinear with the line connecting the B^0 and $\bar{D}^0$ vertices and that the B^0 momentum vector be collinear with the line connecting the B^0 vertex with the primary vertex. For these events, the $\bar{D}^0 \pi^+ \pi^-$ invariant mass is calculated.

Fig. 29 shows the $K^+ \pi^- \pi^- \pi^+$ and $\bar{D}^0 \pi^+ \pi^-$ invariant mass spectra. In both Figs. 29(a,b), the unshaded histograms show all possible track combinations with no cuts on vertex topology. The shaded histograms show the effects of imposing the vertex topology and momentum conservation cuts referred to in the preceding paragraph. It is important to note that the Monte Carlo event sample on this figure contains only B^0 mesons which decayed according to Reaction 2 so that the figure does not reflect the true background level. We explain this further with reference to Table 6, which contains information relevant to the generation and acceptance of all five Reactions $(1-5)$.

For each decay mode entry in Table 6, we show the number of generated events (1000) that have all decay tracks accepted in a spectrometer aperture. The number in the preceding row is the number of generated gluon-gluon fusion events of that type which lead to 1000 accepted events (the $\approx$32% acceptance corresponds to the entries in Table 2 in Chapter 3). The top row in each case is the number of generated $b\bar{b}$ events for the assumed branching ratio from $\bar{B}^0$. For example, in the $D\pi\pi$ case, 4.1×10^6 $b\bar{b}$ events would result in 2969 $\bar{D}^0 \pi^+ \pi^-$ events over the full solid angle. Of these, 1000 events (34%) have all decay tracks accepted. Continuing down the column, we see that 40% of these events or 405 pass the Level-1 selection[3] and 71 events appear in the signal in Fig. 29 if a cut with Δm = 50 MeV is used.

---

[3] $\approx$160 of the 595 events which are lost here are cut because their primary vertices are outside of $\pm$18 cm from the center of the intersection. The true Level-1 efficiency is $\approx$ 50% for this mode.

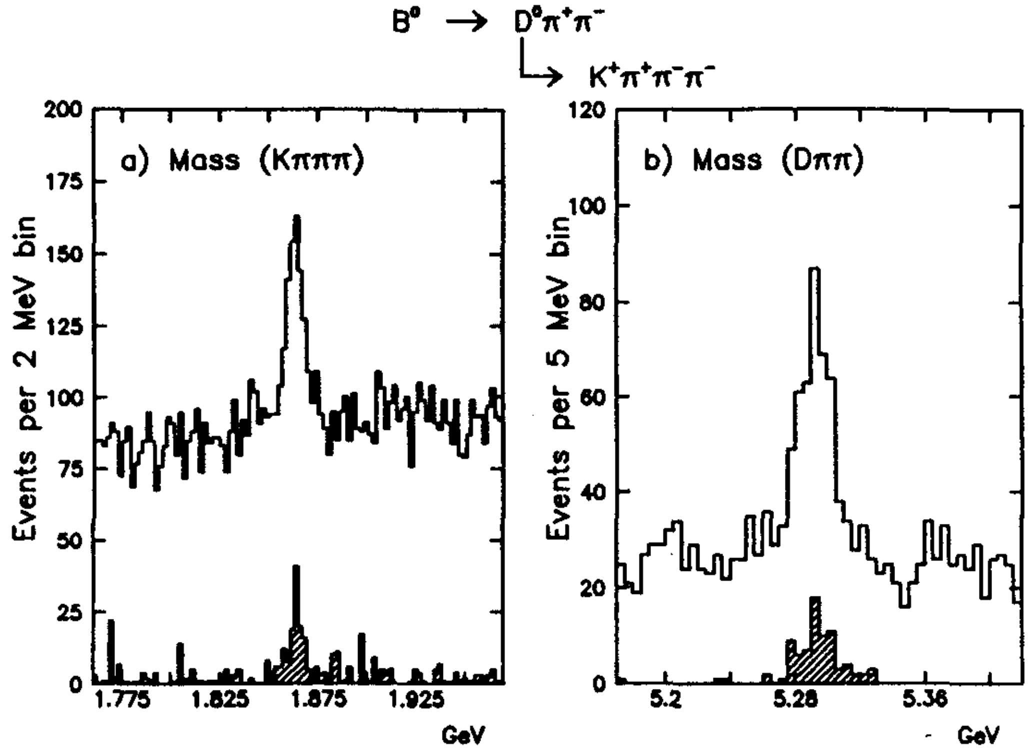

Figure 29: Invariant Mass Spectra for the Final State $\bar{D}^0\pi^+\pi^-$. (a) $\bar{D}^0$ signal in $K^+\pi^-\pi^-\pi^+$ spectrum; (b)B^0 signal in $\bar{D}^0\pi^+\pi^-$ spectrum, both with no vertex cuts. The shaded areas in each plot show the signals which remain after applying the vertex cuts discussed in the text.

The chief source of background under these signals will be from the vast majority of $b\bar{b}$ events which decay via modes other than the one under study. We estimate the background from this source by using the same reconstruction software on the general $b\bar{b}$ sample. In this way, we obtain an estimate of 3 background events under the signal from Reaction 2.

For the analysis of Reaction 1, we start by looping over all $K^+\pi^-\pi^-\pi^+$ mass combinations in an event and form their invariant masses. For each such combination which has a mass near to the $\bar{D}^0$ mass, we loop over all remaining π^- tracks in the spectrometer and form the invariant mass of the resulting $\pi^-K^+\pi^-\pi^-\pi^+$ combination. In fig 30(a) we show the distribution of the mass difference between these two combinations. The peak is from real instances of D^{*+} mesons. For combinations which are consistent with being from the decay of a D^{*-}, we search for instances of B^0 mesons decaying according to reaction 1. The resulting $(\pi^-K^+\pi^-\pi^-\pi^+)\pi+\pi+\pi^-$ mass distribution is shown in Fig. 30(b). In addition to demanding that the D^{*-}/D^0 mass difference be small, we use the same momentum conservation cut as was used for Reaction (2), but a somewhat less stringent cut on event topology. We believe that the $(D^{*-}) - (\bar{D}^0)$ mass constraint is sufficiently powerful that we should be able to further loosen these selection criteria and thus obtain a larger sample of B^0 mesons while maintaining a good signal to background ratio. This is currently under study.

The mass plots resulting from the algorithms developed to search for B^0 mesons decaying according to Reactions 3, 4 and 5 are shown in Figs. 31 and 32(a,b), respectively. The signal and background levels for the modes are summarized in Table 6. With the exception of the $\pi^+\pi^-$ mode, the

Table 6: B^0 Signal and Background Estimates[a]

B^0 Decay Mode	$D^{*+}\pi^-\pi^-\pi^+$ $K^-4\pi$	$\bar{D}^0\pi^+\pi^-$ $K^-3\pi$	$J/\psi K^0$ e^+e^-	$p\bar{p}\pi^+\pi^-$	$\pi^+\pi^-$
No. $b\bar{b}$ events	3.4×10^6	4.1×10^6	3.3×10^8	1.1×10^7	6.5×10^7
Assumed BR[b]	2.4×10^{-3}	1.8×10^{-3}	2.3×10^{-5}	6.0×10^{-4}	1.0×10^{-4}
No. this mode[c]	3230	2969	3001	2537	2599
No. accepted[d]	1000	1000	1000	1000	1000
Pass Level-1	472	405	156	220	139
Signal Evts.	169	71	61	70	27
Background[e]	< 30	< 3	< 13	< 14	< 83

(a) The acceptance numbers assume a two-spectrometer system. However, the percentages of accepted events which pass the Level-1 trigger and survive reconstruction cuts are independent of whether there are 1 or 2 spectrometers.
(b) These branching ratios also include the appropriate D, D^* or J/ψ sub-branching ratios. In columns 2 and 5, the values are only guesses.
(c) This number of PYTHIA events are generated in order to find the 1000 events in each case which have all decay tracks within a 600 mrad spectrometer acceptance.
(d) These events have all decay tracks within a 600 mrad spectrometer aperture.
(e) This is the combinatoric background from all B decay modes, some of which have ambiguous vertex assignments of tracks.

yield of reconstructed events per 1000 accepted events are similar to the yield obtained for the $D\pi\pi$ decay mode. However, the background levels differ widely. The $D\pi\pi$ decay mode is considerably less susceptible to background than either the $p\bar{p}\pi\pi$ mode or the $\pi^+\pi^-$ mode since the assumed branching ratio is higher and the presence of the D meson provides an additional constraint.

No vertex cuts have been applied to the events in Fig. 31 since the signal is already clean. The background estimate for the $J/\psi K^0$ provided in the table is limited by statistics and we believe that it is a considerable overestimate.

All of the signal and background estimates in the table should be regarded as approximations which will improve as we increase the level of sophistication of the reconstruction algorithms and optimize use of the silicon vertex detector.

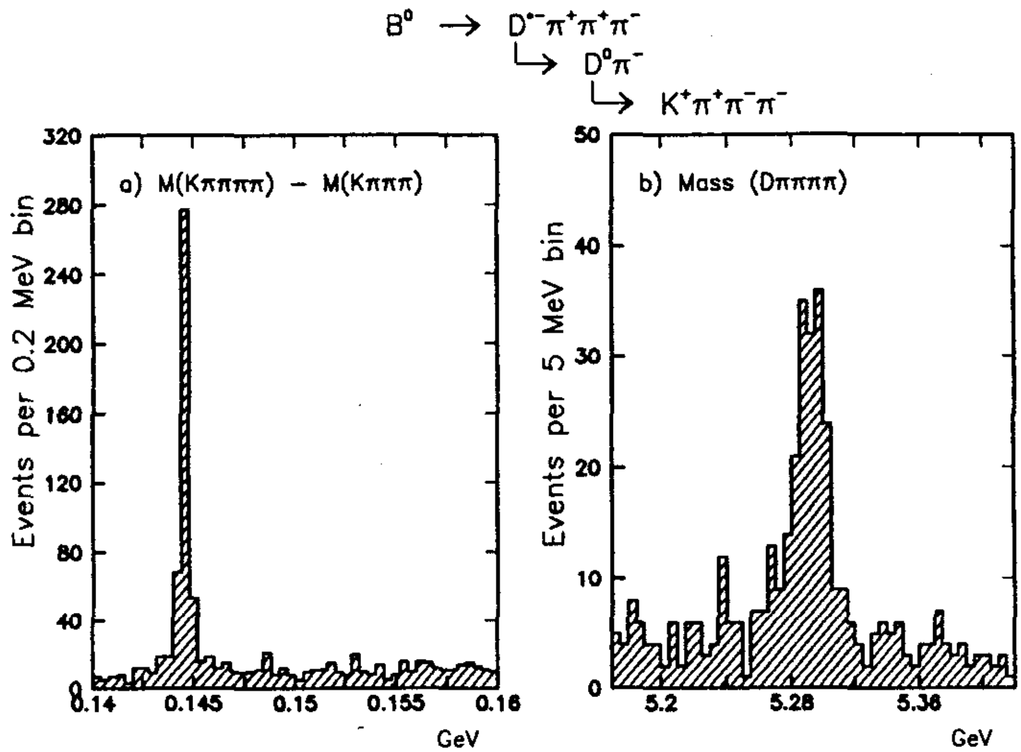

Figure 30: (a) The distribution of the difference in invariant mass between $K^+\pi^-\pi^-\pi^+$ combinations and $\pi^-(K^+\pi^-\pi^-\pi^+)$ as explained in the text. (b) The B^0 signal in the $(\pi^-K^+\pi^-\pi^-\pi^+)\pi^+\pi^+\pi^-$ mass spectrum when $\pi^-(K^+\pi^-\pi^-\pi^+)$ satisfies the $\bar{D}^{*-}$ mass constraint, $K^+\pi^-\pi^-\pi^+$ satisfies the $\bar{D}^0$ mass constraint and after topology and momentum conservation cuts have been applied.

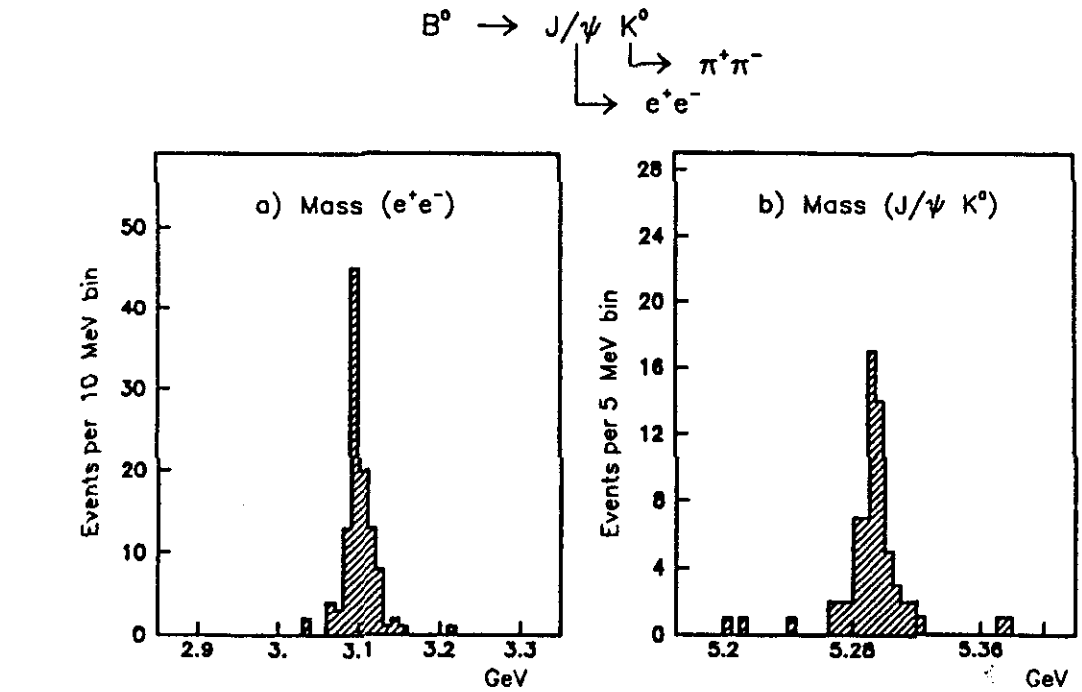

Figure 31: Invariant Mass Spectra for the Final State J/ψ K^0. (a) J/ψ signal in e^+e^- spectrum; (b)B^0 signal in J/ψ K^0 spectrum, both with no vertex cuts.

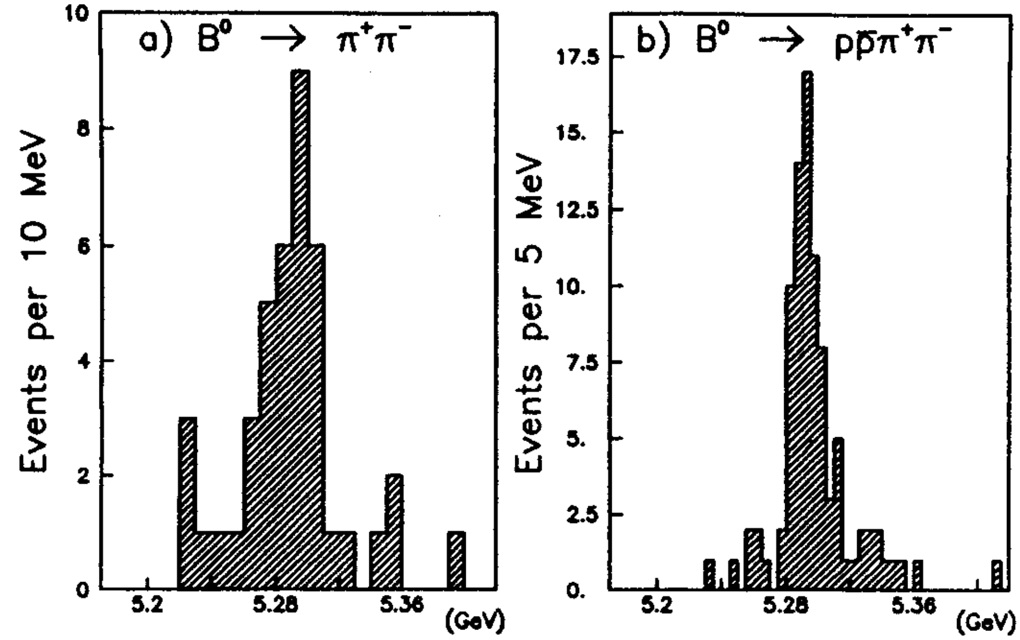

Figure 32: (a) Reconstructed Invariant Mass Spectrum for the Final State $\pi^+\pi^-$. (b) Reconstructed Invariant Mass Spectra for the Final State $p\bar{p}\pi^+\pi^-$. Topology and momentum conservation cuts were applied to the spectra in both (a) and (b).

8. ESTIMATES OF B YIELDS

8.1 Total B Yields

In estimating the total B yield of our proposed experiment, we assume that there are spectrometers on both outgoing arms and that π^0 and γ detection capabilities are available. This gives the true potential yield of this type of experiment. The strategies of what to construct and on what time scale are discusssed below in Chapter 9 on Time Scale & Costs.

The following overall rate factors enter into estimates of all yields.

- *Integrated Luminosity:* We base all estimates on an integrated luminosity $\int\mathscr{L}dt = 10$ pbarn^{-1} (or 10^{37} cm^{-2}). Since the SPS-Collider produced 3 pbarn^{-1} during the 1988 run, it seems quite reasonable to assume that, during the coming 3−4 years, improvements in $\bar{p}$ yields, beam lifetimes and overall system reliability should make 10 pbarn^{-1} a realistic annual integrated luminosity.

- *$b\bar{b}$ Cross Section:* We take a value of 10 μbarn for the total $b\bar{b}$ cross section. Measurements by the UA1 collaboration[16] and QCD parton-parton fusion calculations by Ellis et al.[17] are in essential agreement with this value in $p\bar{p}$ collisions with $\sqrt{s}$ = 630 GeV. With $\int\mathscr{L}dt$ = 10 pbarn^{-1}, this yields an annual $b\bar{b}$ production sample of 10^8 events.

- *Geometric Acceptance:* As discussed above in Chapter 3, 600 mradian apertures on both outgoing arms accept all the decay products of the B or $\bar{B}$ meson for 54% of all $b\bar{b}$ produced (we ignore here the production of Λ_b's). 22% of the time the B and not the $\bar{B}$ is accepted, 22% of the time the $\bar{B}$ and not the B is accepted and 10% of the time both are accepted. This is the purely geometric acceptance and does not consider the losses due to very low momentum tracks, which we discuss in Chapter 7 for $D^*\pi\pi\pi$ mode. Thus, there are the following total numbers of B and $\bar{B}$ mesons produced with all their decay products included inside the 600 mrad apertures.

All B	3.2×10^7 Events
All $\bar{B}$	3.2×10^7 Events
B and $\bar{B}$ Overlap	1.0×10^7 Events

If we assume that the probabilities of a b quark combining with $\bar{u}$, $\bar{d}$ or $\bar{s}$ quarks are in the ratios 40:40:20%, respectively, we have the following numbers of each type accepted:

B^-	1.28×10^7 Events
$\bar{B}^0$	1.28×10^7
$\bar{B}_s{}^0$	0.64×10^7
B^+	1.28×10^7
B^0	1.28×10^7
$B_s{}^0$	0.64×10^7

To proceed further in the yield estimate of total reconstructable events, we note that the ARGUS collaboration[18] has already presented evidence for 16 different exclusive channels, which together represent about 24% of the total decay rate for B^0 mesons and about 10% for B^+ mesons. Table 7 shows the ARGUS B branching fractions as well as the numbers of events of each type that we should obtain with and without π^0 and γ detection capability. In constructing Table 7, we have made use of the known D decay branching ratios[19]. shown in Table 8. In order to obtain the expected yields from our experiment, we have assumed (based on the discussion in the previous chapter) that the product of our trigger efficiency and reconstruction efficiency is 7% for all decay modes except those involving a charged D^*, for which the efficiency is 17%. In addition, there is a 32% overall loss due to pileup inefficiencies, as discussed in Chapter 3. We also allow for a 98% track finding efficiency (per track) and thus an additional $(0.98)^n$ efficiency for an n-track event.

We see in Table 7 that without π^0 and γ detection we can expect about 47,000 reconstructed events (in a two-spectrometer system), while with good electromagnetic capability the expectation is $\approx$280,000 events. Moreover, because our silicon micro-vertex detector completely alters the character of B event reconstruction as compared with the existing e^+e^- experiments, there is little doubt that we will find many additional decay modes not yet detected. For example, existing data suggests that the inclusive branching ratio of $B \rightarrow D^{*+} + X$ is about 35%, while only a little over 6% of this has actually been reconstructed exclusively in $\bar{B}^0$ and B^+ decay. The fact that the branching ratio for $\bar{B}^0 \rightarrow D^*n\pi$ is seen to grow with the number of pions suggests that $D^{*+}5\pi$ (and possibly higher multiplicity states as well) will be large and should be reconstructable by us. It should also be possible for us to reconstruct exclusive final states containing D_s's and Λ_c's, which have inclusive branching fractions of 17.5% and 8%, respectively.

8.2 Sensitivity to $B\bar{B}$ Mixing Studies

As was mentioned in chapter 2, one of the most interesting effects that can be studied in the proposed experiment is that of $B^0 \Leftrightarrow \bar{B}^0$ oscillations. The goal here is to directly measure the time evolution of the B^0 or $\bar{B}^0$ components from an initially pure state, and to do so both for $B^0{}_d$ and $B^0{}_s$ We first show that the measurement resolution on the B flight path is adequate. With the reconstruction simulation described in Chapter 7, we obtain a resolution on the B-meson flight path of 200 μm. This is shown in Fig. 33, which displays a distribution in the B flight path difference between the generated

Table 7: *Yields of Observed $\bar{B}^0$ and B^- Decay Modes*$^{(a,b)}$[18]

	Final State	B Branching Fraction * 10^{-4}	Total Branching Fractions Only Charged * 10^{-5}	Total Branching Fractions With Neutrals * 10^{-5}	Observed Events Only Charged	Observed Events With Neutrals
$\bar{B}^0 \rightarrow$	$D^{*+}\pi^-$	35	31	128	413	1,705
	$D^{*+}\pi^-\pi^0$	200	0	732	0	9,748
	$D^{*+}\pi^-\pi^-\pi^+$	430	378	1574	5,034	20,961
	$D^+\pi^-$	33	48	73	263	400
	$D^+\rho^-$	230	0	506	0	2,775
	$J/\psi K^*$	33	15	18	82	99
	$D^{*+}e^-\nu$	700	616	2562	8,203	34,118
	$D^{*+}\mu^-\nu$	700	616	2562	8,203	34,118
$B^- \rightarrow$	$D^{*+}\pi^-\pi^-$	60	53	220	706	2,930
	$D^{*+}\pi^-\pi^-\pi^0$	560	0	2050	0	27,300
	$D^0\pi^-$	21	38	109	208	598
	$D^+\pi^-\pi^-$	29	42	64	230	351
	$J/\psi K^-$	7	5	5	27	27
	$J/\psi K^-\pi^+\pi^-$	11	8	8	44	44
	$\psi' K^-$	22	2	2	11	11
	$D^0\rho^-$	210	0	1088	0	5,966
				TOTALS	46,848	282,302

(a) Totals include B^0 and B^+
(b) Yields assume two spectrometers

Table 8: *Observed D & D* Branching Fractions in Charged and Neutrals*[19]

	Only Charged Tracks	Including π^0 & γ Modes
D^0	0.180	0.518
D^+	0.144	0.220
D^{*+}	0.088	0.366
D^{*0}	0	0.518

a) only charged decay mode of K^0's are counted
b) we use the following D* final states:

$D^{*+} \rightarrow D^0\pi^+(49\%)$, $D^+\pi^0(34\%)$, $D^+\gamma(17\%)$
$D^{*0} \rightarrow D^0\pi^0(52\%)$, $D^0\gamma(48\%)$

and reconstructed events. The σ of this distribution is our measurement resolution of the B flight path. For a mean B-meson momentum of about 35 GeV/c, a 200 μm resolution corresponds to a resolution in B proper time of 10^{-13} s, compared with the B-meson life time of 13×10^{-13} s or so. Even for the slowest B-mesons reconstructed by our detector (see Fig. 6) of about 20 GeV/c, our resolution is not larger than about 1.7×10^{-13} (σ), which is more than adequate to detect the rapid oscillations expected for B_s.

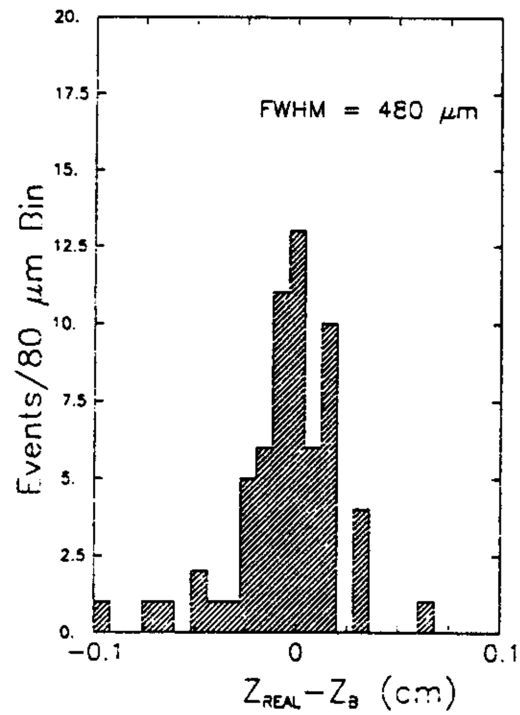

Figure 33: The distance between the generated and reconstructed vertex.

We now estimate the statistical significance of the measurement. In order to do this we discuss the "tagging" strategy; that is, which technique we use to determine the state the decaying particle was in at production time ($t=0$). We consider the following possibilities for tagging:

a) The determination of the charge of the B^+ or B^- produced together with the B^0 ($\bar{B}^0$) under study.

b) The charge of the lepton in the semileptonic decay of the second B.

c) the charge of the $B^{*\pm}$ or $\bar{B}^{**\pm}$, if the $B^0(\bar{B}^0)$ under study originated in the decay $B^{*\pm} \rightarrow \pi^{\pm}B$ (the $B^{**\pm}$ is mentioned because the $B^* - B^0$ mass difference may well be less than m_π).

These and other techniques require a careful analysis that we have not yet completed. For the moment we make the conservative assumption that complete reconstruction of the second B is necessary for good tagging, and that only events of the type

$$B^0, B^{\pm} \quad \text{with:} \quad B^0 \rightarrow D^{*\pm} + (n\pi)$$

can be used for precise measurements of oscillations. Then, under the assumptions of Section 8.1 (that is, only the decay modes of the charged B seen by ARGUS are taken into account) and using the results of Table 7, we arrive at the following event estimate. In one year, 207,848 B^0 and $\bar{B}^0$ are reconstructed, Of these, 31% or 64,433 have accompanying accepted B's, of which 40% or 25,773 are $B^\pm$. What fraction of these are reconstructable ? We take the summed branching fraction for B^- in Table 7 of 3.55% (with neutrals), the average reconstruction efficiency of 28.7% in Table 6 and an average event loss due to track finding inefficiency of 90%. This yields an average efficiency of 0.92% or 237 events in which the B^0 or $\bar{B}^0$ and its accompanying $B^\pm$ are both reconstructed. For the following reasons, this very small number of events is unnecessarily pessimistic.

- More decay modes will be found. There is at least a factor of 2.5 gain from the unobserved D^{*0} decay modes alone (see Table 8).
- The trigger efficiency is larger than assumed. The observed increase in trigger efficiency in Table 6 with charged multiplicity guarantees that the extra tracks of the $B^\pm$ will increase the trigger efficiency (by as much as a factor of two).
- It is probably not necessary to only use fully reconstructed B decays. The topology of the B decays is frequently unique and extra-ordinary.
- The experiment will run for more than a single year.

It seems very unlikely that oscillation measurements will be possible without the use of π^0, γ detection. On the other hand, given such a capability, it should be possible to carry out the necessary measurements with a sample of as many as 10,000 events after a running period of about three years.

9. TIME SCALE & COSTS

We believe that the present collaboration has the strength to construct one charged particle spectrometer with the proposed trigger processor system. However, we probably would require additional strength to build the electromagnetic calorimeters. Because of the obvious benefits of having good electromagnetic calorimetry, as demonstrated in Chapter 8, we plan to actively seek additional collaborators, either from within our institutions or with the addition of new institutions. In any case, because of the importance of proceeding immediately with the trigger processor design, we will not wait for these developments.

As for a second spectrometer, certainly a potential factor of two increase in statistics should not be discarded. It would be especially valuable in the search for rare decay modes. Thus, if additional groups join our collaboration, we shall plan the construction of a second detector, perhaps with modified design parameters. This latter possibility might allow us to improve the efficiency for certain rare modes. However, we will wait until additional groups express interest in joining before worrying about this second detector.

Assuming eventual approval of this proposal by summer 1989, we would attempt to have the experiment designed, built, tested, and in place by the summer of 1992. We realize that this will be very challenging, but it seems feasible.

The major items which we consider here are 1) The silicon vertex detector, 2) The tracking system (wire and pixel drift chambers), 3) RICH, 4) Magnets, 5) Trigger Processors, 6) Readout system, 7) Other computing needs, and 8) Mechanical devices for transport and support.

The first silicon microvertex detector tests have already begun in a UA8 Roman Pot, 13 meters from the interaction center. Although we find that the halo background rate 10 − 12 σ (beam widths)

Table 9: Experiment Cost Estimates (in SF)

Device	Quantity	Unit Cost	Total (kSF)
Silicon Vertex Detector System			
Si Detectors	50	10000	500
Readout electronics	2.5×10^5	2	500
Mechanical Support			250
VLSI Development			100
-------			---
Subtotal			1350
Wire Chambers (Tracking & Pixel)			
Mechanical	3.3×10^4	30	990
Electronic Preamp	3.3×10^4	10	330
Multihit TDC	3.3×10^4	40	1320
Cables, Housing, Power	3.3×10^4	10	330
Laser Alignment			130
Gas Transport			50
-------			---
Subtotal			3150
RICH System			
Quartz Windows	7 m^2	30/m^2	210
Detectors	2 m^2	50k/m^2	100
Gas System			50
Liquid transport & cleaning			50
Mirrors			20
Thermal Regulation			50
Mechanical Mounts			50
Liquids & Gasses			50
Electronics	2.2×10^5	5/ch	1100
-------			---
Subtotal			1680
Magnets			
Quadrupole (ϕ4mx2m)			2000
Dipole (2x2x2m^3)			1000
-------			---
Subtotal			3000
Data-Driven Trigger Processor			
Computational Modules	500	1000	500
Control, Power, and Housing	500	300	150
Development			250
-------			---
Subtotal			900

Table 9: Experiment Cost Estimates (in SF)

Device	Quantity	Unit Cost	Total (kSF)
	Readout System		
Detector Encoding	200	1000	200
Data Buffering/Transport	200	1000	200
Housing & Power	30	4000	120
--------			---
Subtotal			520
	Other Computing		
Online Host Computer			100
Monitoring/Selection μP Farm			1000
Video Tape Storage	4	50000	200
Tapes	3×10^4	8	240
--------			---
Subtotal			1540
	Mechanical		
Supports			100
Transport			100
--------			---
Subtotal			200
Contingencies	12.3×10^6	20%	2460
--------			---
Grand Total			14800

from the beam is sufficiently small to cause no problem to our proposed experiment, we would like to request that we be allowed to perform similar tests at the interaction center ($z=0$) at the earliest possible time. Available readout chips will be evaluated and tested relative to our specific needs. If a new VLSI design should be required, we must ascertain this as soon as possible. The estimated costs for the silicon system are shown in table 9 and include silicon detector, readout electronics, mechanics, and possible chip development costs.

The wire drift chambers contain about 30000 sense wires with building costs estimated at 30 SF/wire. The electronics costs add an additional 60 SF/wire giving a total of 90 SF/wire. The pixel drift chambers, which have about 3000 wires, will use the same electronics and have the same cost per wire. The total electronic and mechanical costs are thus estimated to be 2970 kSF. An additional 180 kSF will be needed for a laser alignment system and a gas delivery system for a system total of 3150 kSF.

The RICH detectors contain about 7 m^2 of quartz costing 210 kSF. Mechanical construction of the 2.0 m^2 of RICH detector is estimated at 100 kSF, The gas system at 50 kSF, liquid transport and cleaning system 50 kSF and mirrors 20 kSF. Other items include thermal regulation, Freon liquids and gasses, and mechanical mounts. The largest item is the readout electronics for 2.2×10^5 channels which is estimated to cost 5 SF/channel for the RICHIP. Development of this chip is currently being pursued and first models are expected at the end of summer 1989. Pad detectors have recently been tested and work as expected. A full scale operating detector is scheduled for september 1989, and full scale test of the combined radiator and detector system will be available early in 1990. Design and construction and testing during the ensuing two years appears eminently feasible. The total cost of the RICH system is estimated to be 1680 kSF.

The magnet costs have been estimated by T. Taylor of LEP division as shown in table 9. We estimate construction time to be 3 years.

General design of the trigger processor will be completed by the middle of summer 1989. We estimate that $\approx$500 modules will be required to provide the processing power necessary to perform the level-1 filter algorithm. An average price of 1 kSF/module is assumed. An additional cost of 300 SF per module is added for power, control and housing. The total development costs for the system (about 30 different modules) including VLSI integration of some of the more common functions is 250kSF.

We would like to request that CERN provide at least the following items: magnet power, vacuum chamber, civil engineering needs, silicon support structure and positioning mechanism, and all supports for detectors close to the beam.

APPENDIX A – Comparison of PYTHIA 4.8 Minimum Bias Events with UA5 Results

We have verified that the PYTHIA generated distributions faithfully reproduce the measured physics distributions at the collider. In particular, we compared several important distributions with the corresponding UA5 [20] measurements. Figure 34 shows the generated and measured rapidity distributions for all events in (a) and, in (b), the ilk for several multiplicity bins. Figure 35(a) shows the multiplicity distributions for all events. Figure 35(b) shows the rapidity distributions of K^0_ss. Finally, Figures 36 and 37 show the comparisons of the K_s and Λ^0 invariant cross sections, respectively.

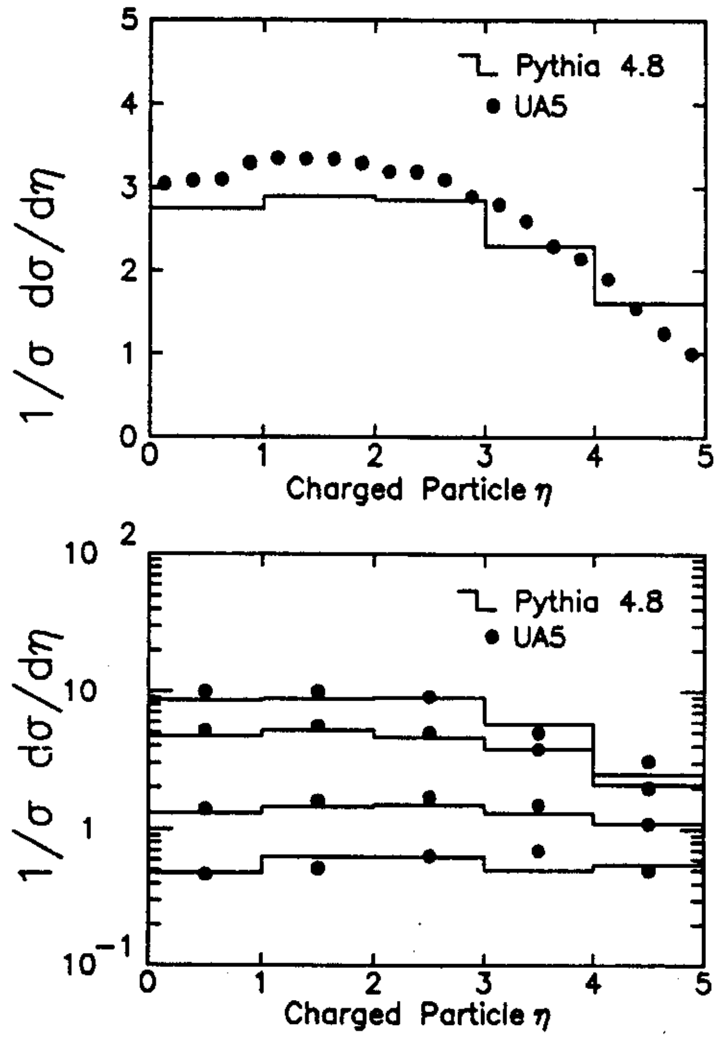

Figure 34: Comparison of charged particle rapidity distributions. Part (a) shows the charged particle rapidity distributions measured by UA5 (points) and those generated by PYTHIA 4.8 (histogram) for all events. (b) shows the same rapidity distributions for different total multiplicity ranges. From top to bottom these are: $N_{ch} \leq 10$, $12 \leq N_{ch} \leq 20$, $42 \leq N_{ch} \leq 50$, and $72 \leq N_{ch} \leq 80$.

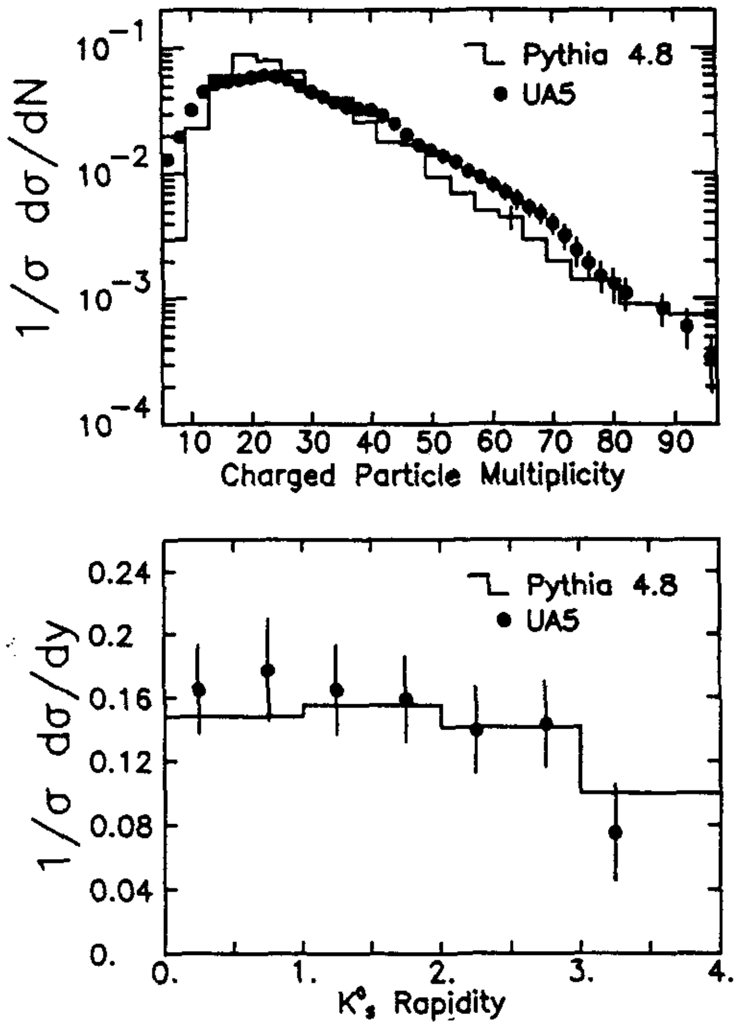

Figure 35: Part (a) shows the charged particle multiplicity distributions measured by UA5 (points) and those generated by PYTHIA 4.8 (histogram) for all events. (b) shows the rapidity distributions for K_Ss.

As can be seen from these figures, PYTHIA generated distributions agree reasonably well with the UA5 measurements of multiplicity, angular distribution, and frequency of occurrence of strange particles.

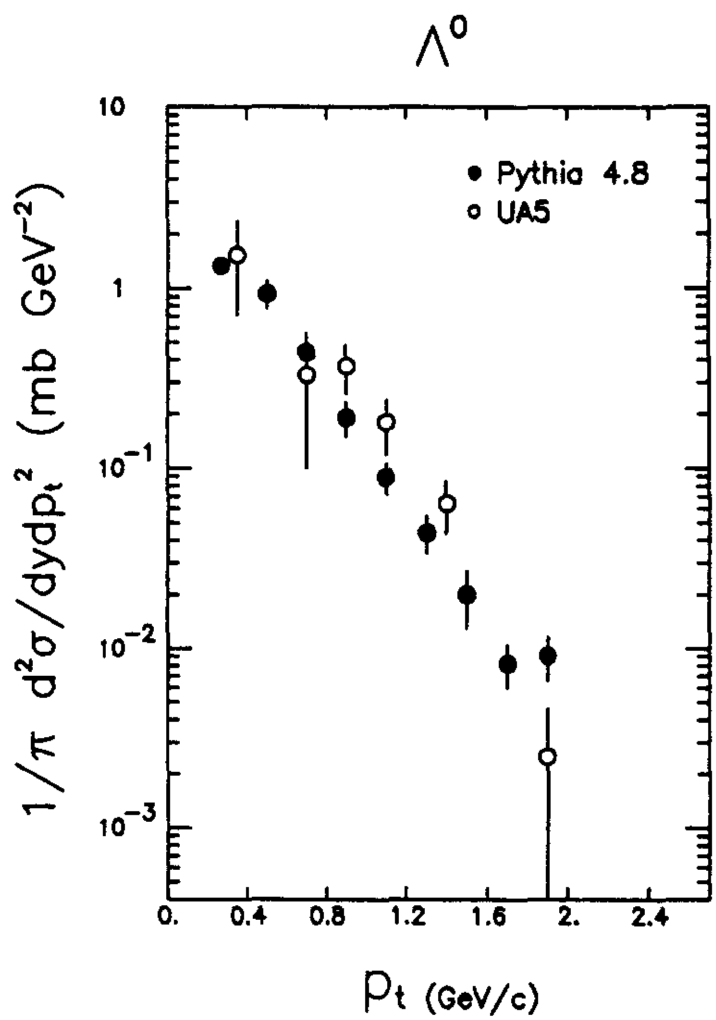

Figure 37: Λ invariant cross section as measured by UA5 (circles) and as generated by PYTHIA 4.8 (points).

APPENDIX B — UA8 Data-Driven Processor Paper

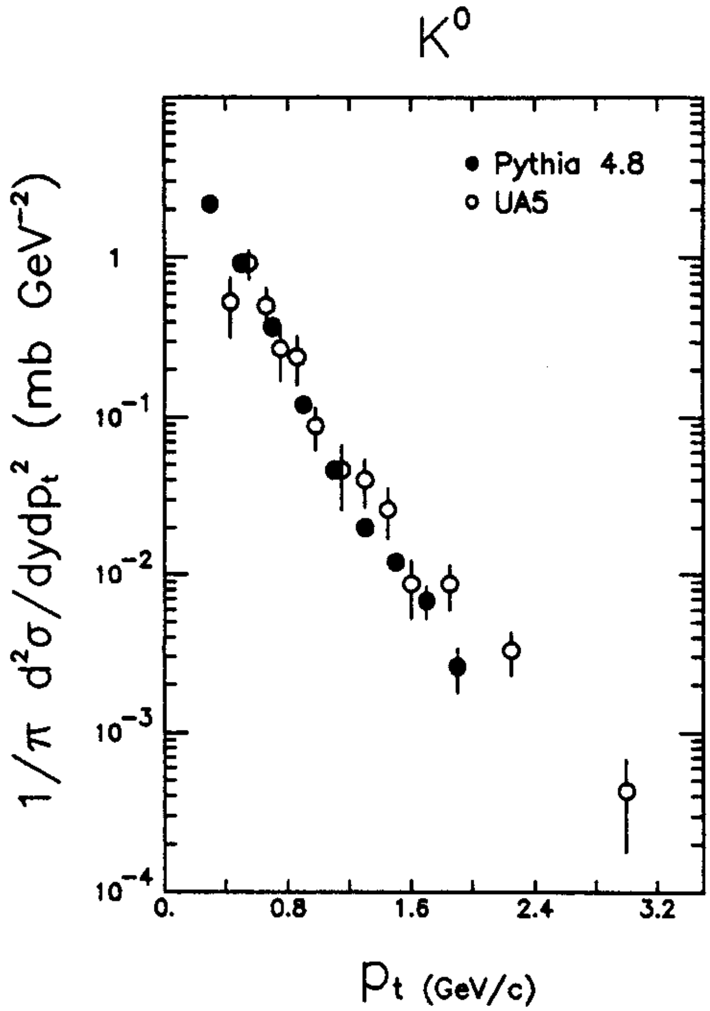

Figure 36: K^0_S invariant cross section as measured by UA5 (circles) and as generated by PYTHIA 4.8 (points).

Nuclear Instruments and Methods in Physics Research A263 (1988) 188–195
North-Holland, Amsterdam

TEST OF A DATA-DRIVEN TRIGGER PROCESSOR FOR EXPERIMENT UA8

J.G. ZWEIZIG, J.B. CHEZE [1], J. ELLETT, S. ERHAN, R. JACKSON, M. MEDINNIS, P.E. SCHLEIN and J. ZSEMBERY [1]

*University of California *, Los Angeles, California 90024, USA*
[1] *Centre d'Etudes Nucleaires-Saclay, Saclay, France*

A fast trigger, based on principles of data-driven processing, has been designed and tested for CERN SPS-Collider experiment UA8. The electronics calculates the momentum vector of a track traversing the UA8 Roman pot spectrometer in 500 ns. When imbedded in the chamber TDC readout system, the total time between signal arrival in the counting room and result is 1.2 μs. The calculations are performed by successive table look-ups and arithmetic operations executed by several examples of a single type of module configured in a data-driven architecture. The operation of the system is monitored with a package of control and diagnostic software. The trigger processor has been successfully tested at the SPS-Collider.

1. Introduction

UA8 is an experiment at the SPS-Collider to study hard scattering effects in events produced by $p\bar{p}$ collisions with $\sqrt{s} = 630$ GeV which have an emerging quasi-elastic proton (or antiproton) in the final state. The final state proton is measured in a Roman pot spectrometer: the hard scattering is observed in the UA2 detector.

Such events, produced via inelastic diffraction,

$$p\bar{p} \to pX(+\text{charge conjugate}), \quad (1)$$

result from the interaction of one beam particle with a soft ($x_F < 0.1$) color-singlet system called the Pomeron in the other beam particle.

Evidence of hard scattering observed in the final states of such processes would signal the occurrence of low order QCD processes between the partons in one beam particle with partons in a Pomeron of the other beam particle [1]. Ultimately, with sufficient data, the detailed study of such events should lead to an understanding of the internal structure and nature of the Pomeron, which plays a major role in high energy hadron scattering.

In the interaction region of UA2 (LSS4), we installed a spectrometer on the outgoing proton arm shown in fig. 1, to measure recoil quasi-elastic protons, and interfaced the readout of this spectrometer to the existing UA2 data acquisition system.

The search for jet structure in the diffractive system, X of reaction (1), requires a trigger consisting of coincidence between a recoil proton signature in the Roman pot spectrometer and total transverse energy in the UA2 calorimeter system, ΣE_T, above some required threshold. This trigger is logically ORed with all other UA2 triggers and initiates a readout of the UA2 detector and our spectrometers to the UA2 data tapes. Preliminary results from test data taken during the 1985 Collider run were presented at the 1986 Berkeley conference [2].

Our 1985 test run demonstrated that the use of scintillators alone to provide the recoil proton signature for the trigger leads to trigger rates several orders-of-magnitude larger than the desired physics. Partially this is because the rate of reaction (1) with $x_F = 1$ dominates the more interesting events with smaller x_F (and larger mass of X). However, false triggers also result from other sources: (i) different low momentum particles traversing each of the Roman pots and creating undesirable coincidences; (ii) beam halo particles with the beam momentum traversing the spectrometer. These sources of uninteresting triggers must be eliminated in order to meet the rate requirements imposed by dead-time considerations.

To eliminate these sources of bad triggers, we proposed [3] to calculate (in real time) the momentum of a

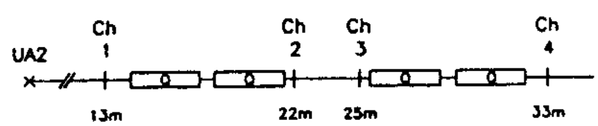

Fig. 1. The UA8 apparatus. Recoil protons from diffractive reactions are detected in four Roman pot spectrometers. There are four wire chambers above and four chambers below the beam line in each arm (only one arm is shown here.) The machine quadrupoles are used for momentum analysis. Hard scattering effects are studied in the UA2 detector at the center. Distances shown are measured from the bunch-crossing center.

* Supported by U.S. National Science Foundation grant PHY85-09175.

particle seen by the Roman pots and also to demand that its initial direction be consistent with having come from the interaction region. The data-driven [4] processor system described in this article satisfies the above requirements and was tested successfully during the 1986 SPS-Collider run.

In a larger multiparticle spectrometer experiment, a more elaborate version of this type of processor [5] will serve as a "front end" in our VIRTUS parallel processor system [6]. VIRTUS is a system of programmable parallel processors in FASTBUS intended for complete online processing of events.

1.1. The UA8 minidrift chamber system

Each chamber in the Roman pot spectrometer shown in fig. 1 comprises 6 MWPC wire planes with 2 mm spacing between wires. The system is operated with a TDC on each wire ("minidrift") and yields a spatial resolution of $\sigma = 130$ μm per plane. There are 2 planes with horizontal wires (y and y', respectively) shifted half a cell from one another to solve the intrinsic left/right ambiguities. There are two planes (u and u') with $+7°$ stereo and two planes (v and v') with $-7°$ stereo. The six planes together provide about 55 μm point resolution in the vertical (bending) plane.

2. Momentum algorithm and implementation with data flow architecture

Fig. 2 shows a sketch of a track traversing an SPS quadrupole magnet with chambers at positions 1, 2 and 3.

2.1. Momentum algorithm

The starting point for the momentum calculation is the equation * for the vertical (y) position of a track propagating along a beam line from position i to position f:

$$y_f = R_{33} y_i + R_{34} y_i' + \Delta (T_{336} y_i + T_{346} y_i'), \tag{2}$$

where Δ is the fractional momentum difference from a central value (e.g., the beam momentum p_0), y_i and y_i' are the starting y position and slope, y_f is the final y position, and the coefficients R_{33}, R_{34}, T_{336} and T_{346} are calculated from the SPS magnet parameters in LSS4 for a particle of momentum p_0.

We solve this equation for Δ using the pot 2 position for the track's initial position, pots 2 and 3 to determine the slope, and the pot 1 position for its final position (the equation is invariant to reversals of the direction of the particle) and find the following result:

$$\Delta = \frac{p - p_0}{p} = \frac{y_1 - R_{33} y_2 - R_{34} y_2'}{T_{336} y_2 + T_{346} y_2'}. \tag{3}$$

Using the fact that $\Delta \ll 1$ and that $e^{\Delta} = 1 + \Delta$, we rewrite the equation as:

$$\begin{aligned}\Delta &= \ln(1 + \delta) \\ &= \ln \frac{y_1 + (T_{336} - R_{33}) y_2 + (T_{346} - R_{34}) y_2'}{T_{336} y_2 + T_{346} y_2'} \\ &= \ln\{ y_1 + (T_{336} - R_{33}) y_2 + (T_{346} - R_{34}) y_2' \} \\ &\quad - \ln\{ T_{336} y_2 + T_{346} y_2' \}.\end{aligned} \tag{4}$$

Since y' is a linear combination of the measured y positions in chambers 2 and 3, eq. (4) may be rewritten as:

$$\Delta = \ln(y_1 + a y_2 + b y_3) - \ln(c y_2 + d y_3), \tag{5}$$

where a, b, c and d are known constants. The calculation of Δ may thus be reduced to a set of four calculations, each of which is the sum of two single variable functions:

$$\begin{aligned} A &= a y_2 + b y_3, \\ B &= c y_2 + d y_3, \\ C &= y_1 + A, \\ \Delta &= \ln(C) - \ln(B). \end{aligned} \tag{6}$$

2.2. Calculation of y-intercept at the bunch crossing center

To calculate the y-intercept at the center of the beam–beam crossing region, y_0, we use the thin lens approximation. This approximation uses the two track y positions measured after the magnet (y_2, y_3) to determine a point at the center of the magnetic field (y_m), which is then used with the hit position in the first pot (y_1) to approximate the initial track trajectory. Specifically,

$$\begin{aligned} y_m &= \frac{z_3 - z_m}{z_3 - z_2} y_2 + \frac{z_m - z_2}{z_3 - z_2} y_3, \\ y_0 &= \frac{z_m}{z_m - z_1} y_1 \frac{z_1}{z_m - z_1} y_m. \end{aligned} \tag{7}$$

* The notation used here is that used by the TRANSPORT beam optics program [7].

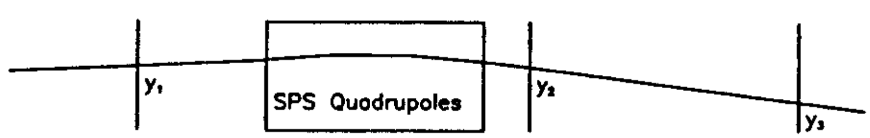

Fig. 2. Tracking of a proton through three Roman pots and an SPS quadrupole pair.

Eqs. (7) are of the same simple type as eqs. (6).

2.3. Implementation

Each line of eqs. (6) and (7) can be executed with the use of a module that has 2 independent digital inputs, a table look-up for each followed by a summation of the two table outputs. Moreover, since the calculations of A and B in eqs. (6) may be performed simultaneously, the entire calculation can be made in 3 module delays. A module with these properties (called DIMSUM, for Dual Input Memory-Look-up and Summation) has been designed and built and is described in section 3.

Eqs. (7) can also be evaluated using DIMSUM modules. This requires only 2 additional modules which function in parallel with the above momentum calculation, therefore taking no additional time.

A second new type of module (called EDSEL for Event Data Selector) is also needed to interface the raw wire chamber hit information (wire numbers and drift times from y and y' planes) to a DIMSUM module which finds the accurate y coordinate. The technical implementation of these modules [8,9] is discussed in the following sections.

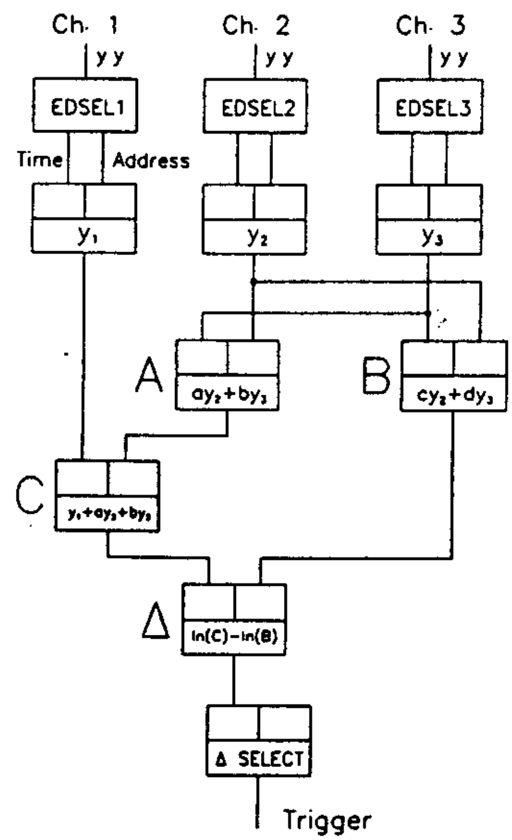

Fig. 3. UA8 trigger processor block diagram.

Symbolically, the algorithm for momentum calculation and selection is executed as shown in fig. 3, which is a data-driven type of computer architecture [4]. The track y coordinates in the three chambers serve as input (by way of the EDSEL modules) to the first of four layers of DIMSUM modules, the last of which produces the Δ of eq. (6). This quantity is input to one final DIMSUM module which selects Δ in some desired range. Since, as discussed below, the time spent in one DIMSUM module is approximately 100 ns, the total time from EDSEL module output to trigger availability is about 500 ns.

3. Dual input memory-look-up and summation module (DIMSUM)

3.1. Physical description

The DIMSUM module is housed in a single width CAMAC module. The modules are interconnected with standard 26-connector flat cables via the front panel, thus allowing arbitrarily complex calculations to be made in a multilayered configuration. Input cable termination resistors are installed in sockets and are consequently easily removed to allow connection of a single output to more than one input.

3.2. Functional description

The basic features of the DIMSUM module are shown in fig. 4 The DIMSUM module has two operational modes. In the first of these, the on-line mode, each 12-bit input word serves to address a 4096 × 14 bit RAM. The first 12 bits of the contents of each addressed word are summed and the result is output on a 12 bit bus. In the second mode, the test mode, the RAM addresses are supplied by a single CAMAC controlled address register, and data can be entered to or read from either table over the CAMAC interface.

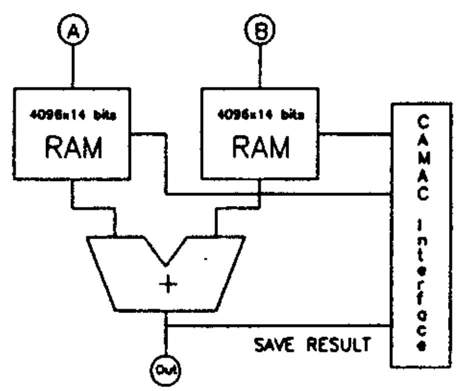

Fig. 4. Block diagram of DIMSUM module.

Module operation is switched between the two modes through the CAMAC interface. Mode changes may be accomplished either by setting a bit in the control register, or by setting or clearing the test mode bit using CAMAC enable and disable functions (F26 · A2 and F24 · A2 respectively). A back panel paired output (LEMO) is set by this test mode status and may be daisy-chained with other modules to indicate that the system is not ready for use.

3.2.1. On-line operations

In on-line mode, the output values are computed from the data on the two input cables as described above. All numeric data are transmitted as TTL compatible dc levels and therefore propagate asynchronously through the system.

Each interconnect cable contains a data valid flag in addition to the numeric data. This flag is originally set by each EDSEL module when data from an event has been latched. Each DIMSUM module asserts the data valid flag on its output cable approximately 100 ns after the data valid flags on both of the input cables have been asserted. This delay is adjustable for each module by setting a potentiometer which is accessible through the front panel. The data valid signal is therefore tuned to propagate through the processor at the same rate as the calculation results. Presence of the flag at the output of the final module indicates that the calculation is complete.

The module contains parity and overflow checking circuitry for detection of hardware faults and illegal input data. The parity error and overflow signals are each available as open collector TTL levels on a pair of LEMO connectors at the back of the module. The paired outputs enable daisy-chaining all the modules in the system to obtain a single system-wide error signal.

3.2.2. Test mode functions

The DIMSUM module is loaded, tested and monitored through CAMAC by way of a simple CAMAC interface on the board which is functionally compatible with both the CAMAC and the CERN REMUS standards. Control and loading of the module are accomplished through four registers accessed via CAMAC. Each register is assigned a unique CAMAC subaddress for write access. However, since REMUS allows reading from only one CAMAC subaddress, a jumper option allows the internal address field of the control register to specify the register to be read in a CAMAC read operation.

In standard CAMAC, the data may be read or written either with single action calls, or, in the case of the memory data, with repeat mode block transfers. Since the Q response for valid commands is always 1, any such block transfer has to rely on LAM synchronization or a word count to end the transfer. ROMULUS/REMUS block transfers may be made using the LAM synchronized repeat mode. In accordance with the usual ROMULUS procedure, a LAM is set by the enable function (F26) and cleared after a successful read of the status or address register, or when an address overflow occurs on a read of one of the table memories. LAM response may be disabled by clearing the LAM mask bit in the control register with a F24 · A1 or by writing a zero to bit 14 of the control register.

Software utilities exist for emulating a DIMSUM system as well as loading, testing, and facilitating the repair of such a system. These are described below in section 5.

4. Technical implementation of chamber readout and trigger

Fig. 5 shows a block diagram of the TDC readout and trigger system in the configuration used for the on-line calculations in UA8.

4.1. The TDC readout system

The trigger implemented for UA8 works in three stages. First, a signal synchronized with the bunch crossing (RF) generates a gate for the chamber TDC system and all CAMAC instrumentation. ECL logic signals from each "struck" wire of the chamber system which arrive at the inputs of the 32-channel TDC modules while the gate is asserted cause a 4-bit Gray-code clock signal to be latched. This constitutes the time digitization.

One 32-channel TDC receives the signals from one wire plane. All six TDCs for a given chamber are placed in a single crate such that the y and y' plane TDCs are read out first. Each crate also contains a readout module, which sends the gate and clock signals to the TDC modules over the crate backplane, and controls the sequential readout of the hit data into a memory module. All TDC crates are read out in parallel.

The second stage of the trigger starts 80 ns after the arrival of RF, when all signals from the minidrift chambers have been time-digitized. At this time, the parallel readout from the TDC crates is started, causing all chamber hit data to be transferred to the memory modules at a rate of 75 ns per hit. During this readout process, the hit data from the y and y' planes are picked up and latched by the EDSEL modules in the EDSEL–DIMSUM crate shown in fig. 5.

There is one memory module per chamber crate, which can store up to 31 16-bit hit words. All the memory modules are located in a single central memory crate. The data in the memory modules are accessible by the UA8 on-line computer (for diagnostic and control functions) via a control module located in the memory crate.

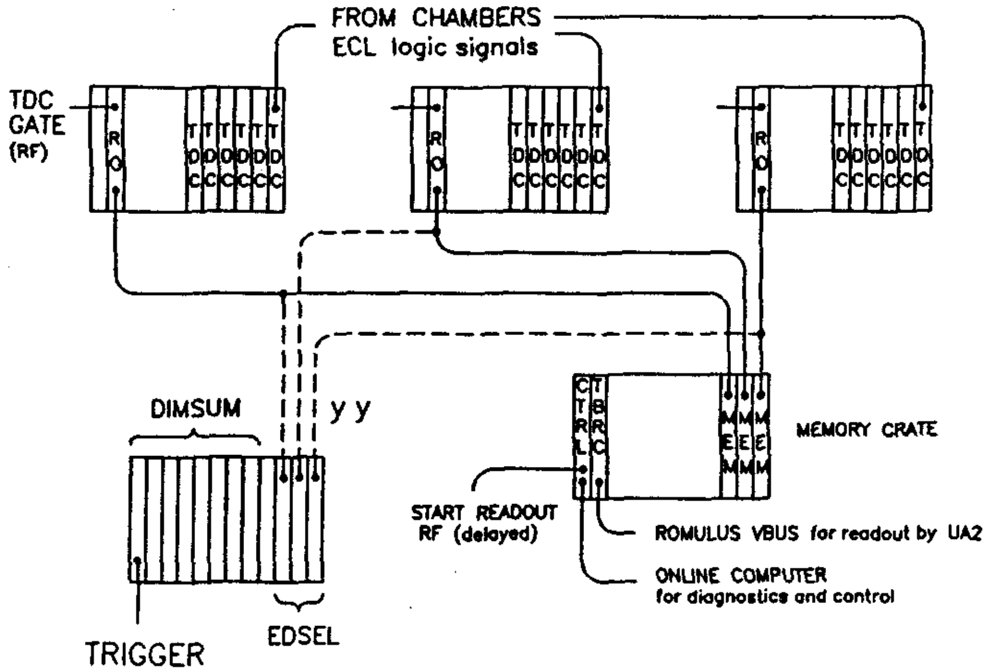

Fig. 5. TDC readout system with DIMSUM processor attached. The dashed lines show the connections of the new EDSEL-DIMSUM crate to the pre-existing UCLA TDC system.

The final stage of the trigger logic is provided by the chamber hit consistency check and momentum calculation of the EDSEL-DIMSUM system, as described in the following section.

Transfer of data to the UA2 on-line computer takes place through a so-called TBRC module [10] which resides in the memory crate and interfaces the crate bus to a CERN standard ROMULUS VBUS. Upon receipt of a prepare and go signal over the ROMULUS VBUS, the TBRC scans through all the memory modules and transfers the hit data over the VBUS (under internal control).

4.2. EDSEL-DIMSUM operation

The final stage of the trigger commences when the three EDSEL data latch modules determine that the hit pattern in the selected planes (y, y') is consistent with having resulted from the passage of a single track through each chamber. When this occurs, data valid signals are set at the outputs of the EDSEL, and the hit information and accompanying validity indicator begin to propagate through the DIMSUM-based computing structure.

The precise y and y' coordinates for each chamber are determined by one EDSEL module followed by a DIMSUM module. As shown in fig. 5, the EDSEL module connects to the cable which runs from the TDC readout module for a given chamber to the memory module. During the readout from TDC crates to memory crate, an EDSEL module counts the number of hits with valid drift times in the y and y' planes and latches the hit address and time code for one of the hits from each of these planes. A data valid signal is generated only for events with one or two adjacent hits in both the y and y' planes. In the case that either of these planes contains two hits, the information from the hit with the lesser time code is stored, and the other hit is ignored.

The latched hit addresses, time codes, and ambiguity variable (which indicates the drift direction) are sent over two cables to a DIMSUM module for calculation of the y coordinate for the chamber. The first of these cables carries the address of the hit y-plane wire. This is converted to a y position by table look-up in the DIMSUM board. The other cable contains the time codes and ambiguity variable from which is computed a signed drift distance. The sum of these two quantities – which is the y coordinate – appears on the output of the DIMSUM module.

4.3. Limit comparison and final trigger calculation

A single trigger signal is derived from the results of the DIMSUM calculations by comparing the momentum variable and the y intercept position to one or more sets of limits * and logically combining the results of these comparisons. This step is implemented using a further DIMSUM module. In this scheme, the y intercept position (calculated using eqs. (7) as described in section 2), and the momentum variable are each sent to one input of a DIMSUM module. Each of the multiple triggers are assigned a pair of adjacent bits in the DIMSUM data word. The tables are set such that the low order bit of each trigger pair is set on for all input values which are valid for the associated trigger. The paired bits at the output of the adder then contain the logical AND and exclusive OR of the two range selections. One or both of these logical combinations are used by the trigger electronics to indicate the existence of a valid track.

5. Diagnostic software

5.1. The system definition files

All modules and interconnections are specified in an on-line definition file which is used by the following software packages: (1) table loader/verifier; (2) connection verification routine; (3) module diagnostics; and (4) system emulator.

5.2. On-line definition files

This file describes the processor completely. Fixed format records describe the CAMAC address of each EDSEL or DIMSUM module, the contents of the DIMSUM tables and all interconnections between the EDSEL and DIMSUM modules. It therefore provides a functional description of the system which can be compared with the system itself.

5.3. The table loader / verifier program

The table loader and verifier program fills the DIMSUM tables and then reads them back to verify that they were properly loaded. All DIMSUM modules listed in the configuration file are loaded and verified in turn. The table is built up in memory based on the table description in the configuration file and loaded into the DIMSUM with a single DMA transfer. The contents of the tables are then read back and compared to the original. If any errors are found, an error message is printed and the program terminates.

* Several sets of momentum limits are foreseen to provide separate triggers (which are individually selectable by the fast electronics) for elastic scattering, inclusive diffraction, high mass diffraction and double-Pomeron exchange.

5.4. Connection verifier

The connection verifier insures that all interconnections between EDSEL and DIMSUM modules are installed correctly. The program sets each EDSEL module to produce an alternating 1/0 bit pattern and then follows the pattern through all DIMSUM modules downstream of the EDSEL. It then reverses the pattern and repeats the verification procedure to insure that all signals in each of the cables are making good contact. Any bad connections are reported by the program.

5.5. Module diagnostics

A diagnostic routine exists for testing any DIMSUM or EDSEL module inside the system. All functional units and data paths in the modules are tested. If an error is detected, it is reported to the operator and the program optionally enters a loop repeating the failing test to allow the repair of the module.

5.6. System emulation

A library of routines exists for facilitating the emulation of the system. Fortran callable routines are available to (1) build the system configuration database, (2) locate functional elements using symbolic names, and (3) emulate a DIMSUM module.

The following routines are also planned: (1) cycle hits through an EDSEL module; and (2) examine the contents of an arbitrary cable.

6. Results of test run – May 1986

The last two weeks of the Spring 1986 collider run afforded us our only opportunity to test the trigger system before the ACOL startup scheduled for the Fall of 1987. The UA2 detector had by this time already been removed so that it was not possible to trigger simultaneously with the trigger processor and the transverse energy deposition in the UA2 central calorimeter. Nonetheless, we were able to test the trigger processor and study backgrounds under conditions very similar to those we will encounter during the data taking stage.

Detectors were installed in the four pots above the outgoing proton beam as well as the four pots below the outgoing $\bar{p}$ arm. At that time, we had enough DIMSUM and EDSEL modules available for one of the four pot spectrometers. We chose to equip the outgoing proton arm with the processor since the background from beam halo is more severe in this arm and is therefore closer to what we expect starting in 1987.

Our first level trigger consisted of a three-fold coincidence of the scintillators in the first three pots of the proton arm and a veto formed from the scintillators in

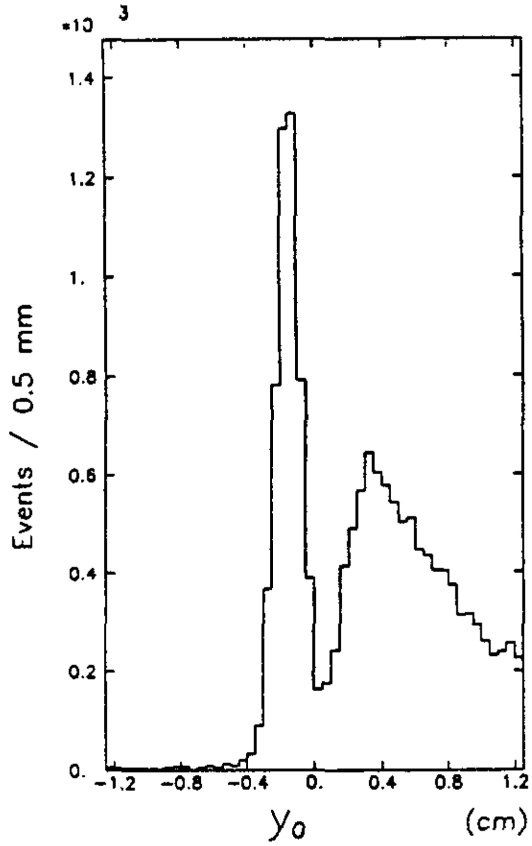

Fig. 6. y-coordinate of track at $z = 0$. The measured track extrapolated to the bunch-crossing center at $z = 0$ separates those arising from beam–beam interactions from background tracks.

the $\bar{p}$ arm. The timing of the veto was set to cut out protons in the beam halo which traverse the $\bar{p}$ arm spectrometer in the opposite direction from tracks from valid interactions and are then focussed into the proton arm spectrometer.

A second level trigger was formed by the EDSEL modules and demanded valid hit combinations in the first three of the chambers of the proton arm spectrometer, as described in section 4. The detector in pot 4 served mainly to provide redundant information for the off-line analysis and was not used either in the trigger or in the analysis presented here.

Data from events satisfying the second level trigger were written on tape and further analyzed off-line. In addition to the raw chamber information, each event record also included the output data from every DIMSUM module, including the momentum estimate and DIMSUM trigger decision (although this was not used in the on-line trigger).

Fig. 6 shows the distribution of the vertical coordinate (y_0) of reconstructed tracks projected to the bunch-crossing center. The tracks with y_0 greater than zero are mainly from proton beam halo which escaped the halo veto. The narrow peak centered at -0.15 cm is from valid interactions. Although we did not calculate y_0 on-line during the Spring run, such a calculation could be made by the method described in section 2. Thus, we will be able to considerably improve our halo veto by rejecting those tracks not originating from the interaction region.

The DIMSUM momentum spectrum for those tracks

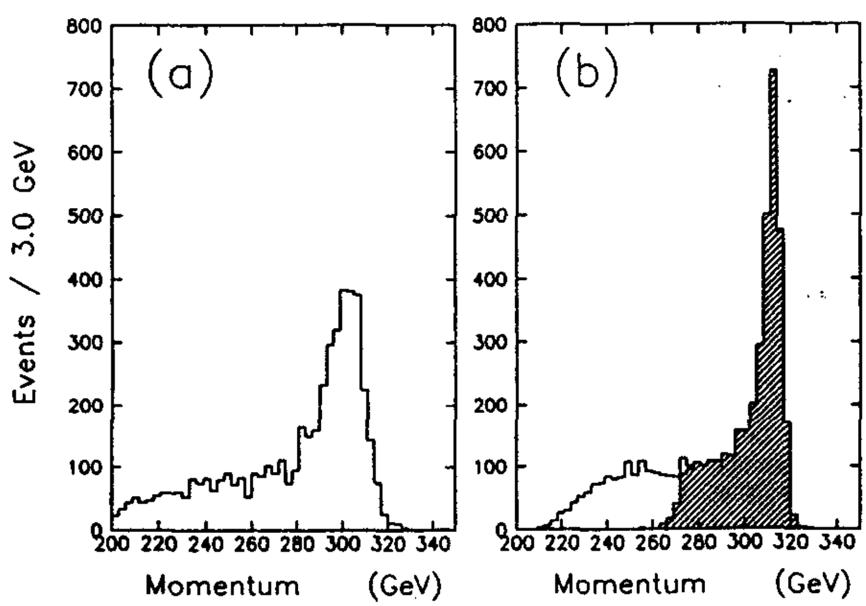

Fig. 7. UA8 momentum spectra. (a) The on-line calculation. (b) An off-line calculation. The shaded events are those selected with an on-line cut.

in the peak of fig. 6 is shown in fig. 7a. This spectrum was also available on-line (except for the y_0 cut) where it served as a powerful diagnostic tool. Fig. 7b shows the momentum spectrum from tracks reconstructed off-line from the same events used for fig. 7a. The peak in fig. 7a is broader than that in fig. 7b and also displaced from the nominal beam momemtum of 315 GeV. This is because the correct geometry constants were not known at the time of the test run. We expect the on-line resolution to be nearly as good as the off-line estimate when the correct constants are loaded into the DIMSUM tables. Nevertheless, the on-line resolution for the test run would already have been adequate for triggering purposes.

When the data of fig. 7b were recorded, the processor was set to trigger on tracks with momentum larger than 265 GeV/c (even though the processor trigger was ignored during the test run, its status was written into the event record). The shaded region of fig. 7b is the spectrum of those events which satisfied the processor trigger. Except for a small region near the momentum cut, there is no trigger inefficiency and furthermore, there are no events in which the off-line and on-line momentum estimates grossly disagree.

Acknowledgements

We thank the SPS Division for the effort required to make the UA8 1986 Collider run possible. The support of the CERN administration is gratefully acknowledged. We thank David Plane for his work on the momentum algorithm. Two of us (P.E.S. and J.G.Z.) particularly wish to thank Bruce Knapp and Bill Sippach for many helpful and friendly discussions about their work with data driven processors.

References

[1] G. Ingelman and P. Schlein, Phys. Lett. 152B (1985) 256.
[2] R. Bonino et al. (UA8 collaboration), contribution to the 23rd Int. Conf. on High Energy Physics, Berkeley (1986).
[3] S. Erhan et al., Proposal to the SPSC P208, CERN-SPSC/84-82.
[4] W. Sippach, G. Benenson and B. Knapp, IEEE Trans. Nucl. Sci. NS-27 (1980) 578; H. Cunitz, Y. Hsiung, B. Knapp and W. Sippach, Data Driven Processing, in: Proc. Int. Conf. on Instrumentation for Colliding Beam Physics, SLAC Report 250 (June 1982).
[5] For large-scale applications of these methods, see: L. Borten et al., A Data Driven Parallel Pipelined Hardware Reconstruction Processor, p. 45 and D.M. Kaplan, A Parallel, Pipelined Event Processor for Fermilab Experiment 605, p. 31; Proc. Symp. on Recent Developments in Computing, Processor and Software Research for High-Energy Physics, Guanajuato, Mexico (May 8-11, 1984).
[6] J. Ellett, R. Jackson, R. Ritter, D. Yaeger and J.G. Zweizig, VIRTUS - A System of Parallel Processors in FASTBUS, UCLA-VIRTUS/86-04.
[7] K.L. Brown et al., TRANSPORT, A Computer Program of Designing Charged Particle Beam Transport Systems, CERN 80-04.
[8] J. Ellet, R. Jackson and J.G. Zweizig, The Dual Input Memory-Lookup and Summation Module, DIMSUM, UCLA-VIRTUS/86-02.
[9] J. Ellett, R. Jackson and J.G. Zweizig, The Event Data Selection Module, EDSEL, UCLA-VIRTUS 86-03.
[10] J. Ellett, R. Jackson and J.G. Zweizig, The TDC Buffer Readout Controller, UCLA-VIRTUS/86-01.

APPENDIX C – Rich Resolution

C1 – Liquid Radiator

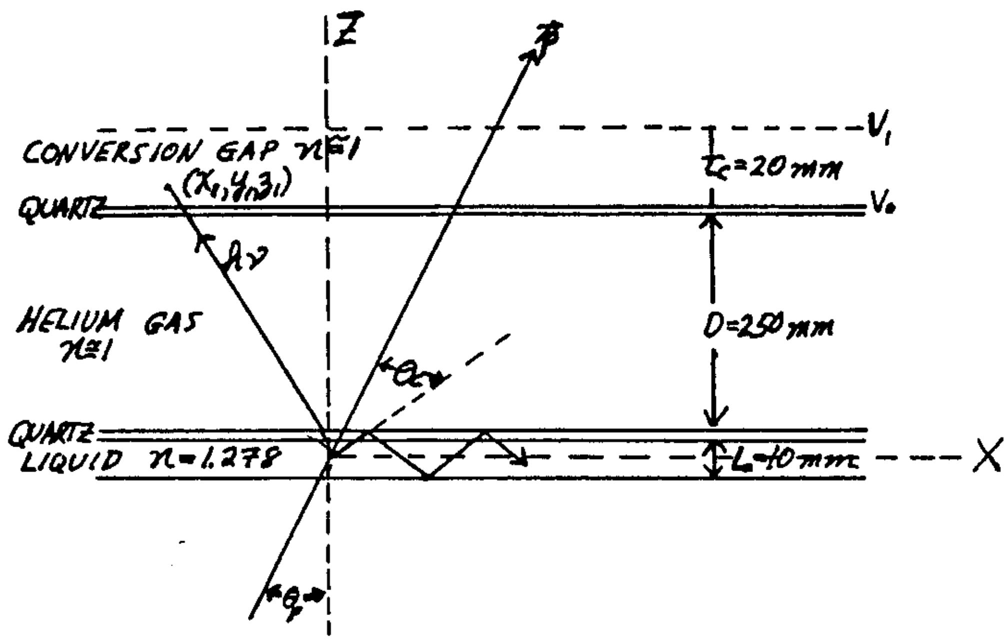

Figure 38: Liquid Radiator Geometry.

The xz plane is defined to contain the radiator normal (z) and the particle momentum vector ($\vec{p}$) as shown in Fig. 38 The photon emission point ℓ along the particle direction varies between $-L/2 \cos\theta_p < \ell < +L/2 \cos\theta_p$ and is unmeasurable. Hence $\sigma_\ell = L/\sqrt{12} \cos\theta_p$. The photon energy is also unmeasurable and has an energy width ΔE determined by the detector response, in this case $\sigma_E = \Delta E/\sqrt{24} = .31$ eV. The photons are detected at points (z_1, x_1, y_1) in the detector volume with r.m.s. errors $\sigma_{z_1}, \sigma_{x_1}$ and σ_{y_1}. The Cherenkov angle θ_{CR} may be reconstructed from the measured quantities z_1, x_1, y_1, θ_p, $\ell = \langle\ell\rangle = 0$, $n = \langle n \rangle = 1.278$ with the formulas (valid for vanishingly thin window and radiator)

$$\cos\theta_{CR} = (\sin\theta_p/n)(x_1/r_1) + (\cos\theta_p/n)\sqrt{[n^2 - (x_1^2 + y_1^2)/r_1^2]}$$

$$\tan\phi_{CR} = y_1/[x_1 \cos\theta_p - \sin\theta_p \sqrt{(n^2 r_1^2 - x_1^2 - y_1^2)}]$$

The derivatives of these reconstruction formulas allow calculation of the angular error at a given ϕ_c via the relation $\sigma_{\theta c} = (\partial\theta_c/\partial v_i)\,\sigma_{vi}$ The derivatives are:

$$\partial\theta_c/\partial x_1 = (\beta\sqrt{K}/z_1)[K\cos\phi_c/\alpha - \sin\theta_p\tan\theta_c\sin^2\phi_c/\beta^2]$$

$$\partial\theta_c/\partial y_1 = (\beta\sqrt{K}/z_1)\sin\phi_c[1/\beta^2 - \cos\theta_p(n^2-1)/\alpha]$$

$$\partial\theta_c/\partial z_1 = -(K/z_1\alpha)(\cos\theta_p\tan\theta_c + \sin\theta_p\cos\phi_c)$$

$$\partial\theta_c/\partial\theta_p = -\cos\phi_c$$

$$\partial\theta_c/\partial\ell = (\tan\theta_c\sqrt{K}/z_1\beta)[(\beta^2K/\alpha^2)(1-\sin^2\theta_p\sin^2\phi_c) + \sin^2\theta_p\sin^2\phi_c]$$

$$\partial\theta_c/\partial n = (n\tan\theta_c)^{-1}(n^2\beta^2)(\cos\theta_p/\alpha)$$

with $\alpha = \cos\theta_p - \sin\theta_p\tan\theta_c\cos\phi_c$ and $K = 1 - n^2 + \alpha^2/\beta^2$.

C2 – Gas Radiator

The xz plane is defined such that the z axis is the radial line parallel to the particle direction $\vec{p}$ and the x axis is along the line connecting the point of closest approach to the mirror center of curvature C. The particle trajectory thus lies in the xz plane as shown in Fig. 39 . The emission point (z,x,0) is measured in the particle reference frame (PQR) while the detected point (z_1,x_1,y_1) is measured in the detector reference frame (ZXY). The general defining equations (thin window approximation) are (with $r = \sqrt{(z^2+x^2)}$ and $r_1 = \sqrt{(z_1{}^2 + x_1{}^2 + y_1{}^2)}$)

$$\Omega_1 = \Omega - \sin^{-1}(r\sin\Omega/r_1) - 2\sin^{-1}(r\sin\Omega/r_m)$$

$$\cos\Omega_1 = [(zz_1 + xx_1)/rr_1]\cos\theta_p + [(zx_1 - xz_1)/rr_1]\sin\theta_p$$

$$\cos\Omega = (z\cos\theta_c + x\sin\theta_c\cos\phi_c)/r$$

The relevant derivatives $\partial\theta_c/\partial v_i$ for the variables $v_i = (z,x,z_1,x_1,y_1,\theta_p)$ are obtained from the above equations and are of the form

$$\partial\theta_c/\partial v_i = [r\sin\Omega(A_i - K_i)/(1 + J\cos\Omega) - B_i]/D$$

with $D = z\sin\theta_c - x\cos\theta_c\cos\phi_c$ and $J = (r_1{}^2 - r^2\sin^2\Omega)^{-1/2} - 2(r^2{}_m - r^2\sin^2\Omega)^{-1/2}$.
The quantities K_i, A_i, B_i are summarized in the following table for each variable v_i :

v_i	K_i	A_i	B_i
z	$Jz\sin\Omega/r$	$(zr_1\cos\Omega_1 - z'_1r)/(r^2r_1\sin\Omega_1)$	$(z\cos\Omega/r) - \cos\theta_c$
x	$Jx\sin\Omega/r$	$(xr_1\cos\Omega_1 - x'_1r)/(r^2r_1\sin\Omega_1)$	$(x\cos\Omega/r) - \sin\theta_c\cos\phi_c$
z_1	$-z_1G$	$(z_1r\cos\Omega_1 - z'r_1)/(rr_1{}^2\sin\Omega_1)$	0
x_1	$-x_1G$	$(x_1r\cos\Omega_1 - x'r_1)/(rr_1{}^2\sin\Omega_1)$	0
y_1	$-y_1G$	$(y_1\cos\Omega_1)/(r_1{}^2\sin\Omega_1)$	0
θ_p	0	$(a\sin\theta_p - b\cos\theta_p)/\sin\Omega_1$	0

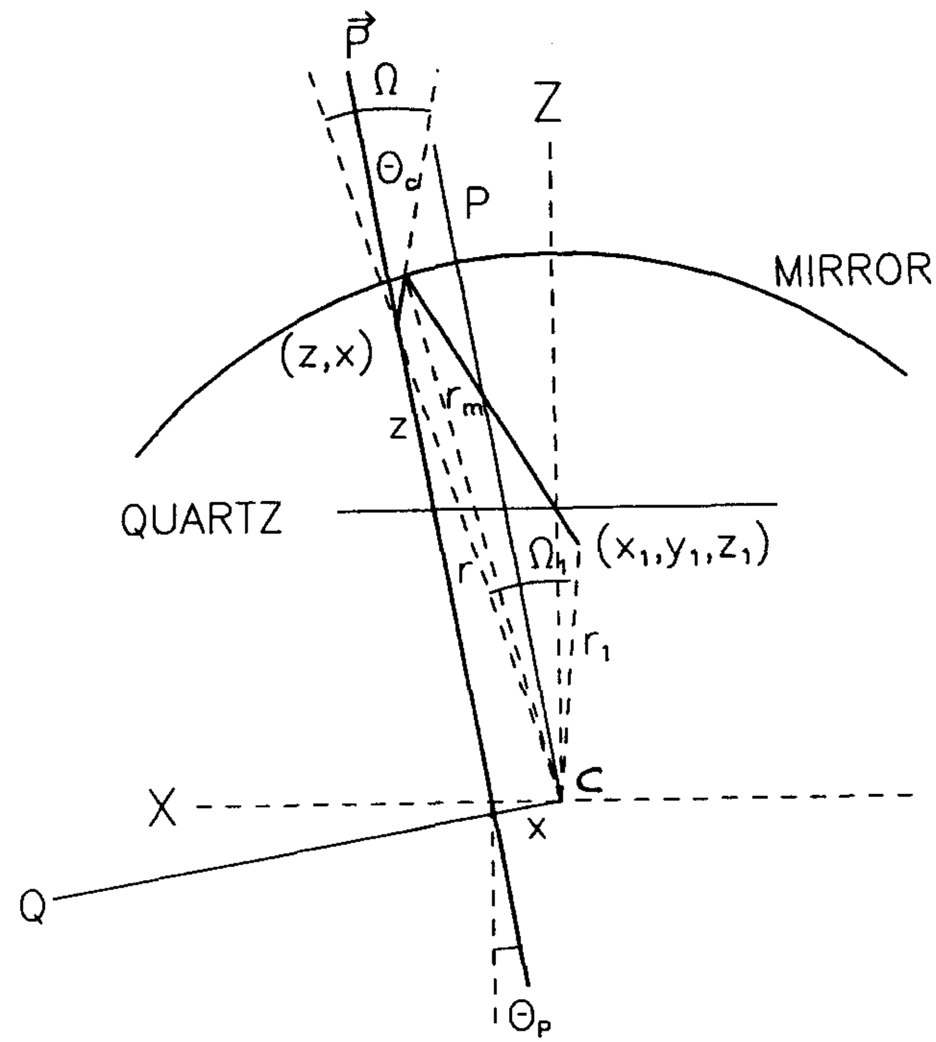

Figure 39: Gas Radiator Geometry.

with $G = r\sin\Omega/[r_1^2(r_1^2 - r^2\sin^2\Omega)^{1/2}]$, $a = (zz_1 + xx_1)/rr_1$ and $b = (zx_1 - xz_1)/rr_1$. The vector (z'_1, x'_1) is related to the vector (z_1, x_1) by a finite rotation through angle θ_p and (z', x') to (z, x) by a rotation through angle $-\theta_p$. The chromatic error is, as before, $\sigma_{\theta c}(E) = (\partial\theta_c/\partial n)(dn/dE)\sigma_E$ with $\partial\theta_c/\partial n = (n\tan\theta_c)^{-1}$, dn/dE the radiator dispersion and σ_E the energy error.

APPENDIX D

Possible Liquid Xenon Electromagnetic Calorimeter

We plan to have as the final element in each spectrometer, a fine-grained high-resolution electromagnetic calorimeter which will allow us to reconstruct B (and D) decays with one π^0 (or more ?) in the final state. The use of liquid Xenon in the calorimeter is dictated by the need for the best energy and space point resolution attainable.

Liquid Xenon is a very fast and efficient scintillater which yields one photon of 7.3 eV per 50 eV energy loss with a 3 ns lifetime. The proposed calorimeter will simultaneously detect ionization charge and scintillation light via locally deposited (in situ) organic photocathodes. It has been established by Doke et al.[21] that there exists an anticorrelation between fluctuations in ionization charge and scintillation light in noble liquids. Hence a suitable linear combination of the two signals should give much better energy resolution than either alone.

Such organic photocathodes have been recently developed by Peskov, Charpak, Séguinot, Ypsilantis et al.[22]. The quantum efficiency for 7.3 eV photons will be high ($\approx$50%) resulting in a signal from light of 10^4 electrons per MeV of energy deposition. The light signal will provide a fast trigger signal ($\approx$10 ns) which is the start for a clock which measures the arrival time of the ionization charge signal. (maximum drift time $\approx 3\mu s$). The time and hit wire of this ionization charge signal establish the core of the electromagnetic shower with a precision of about 300 μm.

Energy resolution of this detector is estimated to be $\sigma_E = 0.005 \sqrt{E}$ (E in GeV). Because the calorimeter is totally active, its sensitivity will extend down to 10 MeV. Other advantages of noble liquid scintillaters are: (1) its light and charge signals are proportional to energy loss even for heavy ions with up to 10^4 minimum ionization; (2) the detector is highly radiation resistant because the liquid can be continuously circulated and cleaned.

The basic cell structure being designed has 20×20 mm^2 transverse dimensions and 56 mm longitudinal ($2X_0$). Thus, a tower structure 10 cells in depth has $20X_0$ containment of the electromagnetic shower.

The calorimeter in the first spectrometer covers 17.3 m^2 of area and the second 4.5 m^2 for a total of 22 m^2. Since each cell has an area of 400 mm^2, we require 5.5×10^4 cells per layer; ten layers in depth give a total of 5.5×10^5 cells. The read out of the cells is via wave form sampling circuits which allow current division to pinpoint the collection time and hit wires. Two such circuits are used per 10 cells for a total of 1.1×10^5. In addition, the fast cathode signals are read out for each tower (10 cells in depth) which will require 5.5×10^4 additional readouts for a total of 1.65×10^5 for the calorimeter.

The calorimeter depth is 0.6 m ($20X_0$) and its surface area is 22 m^2. Hence its volume is 13 m^3 and its weight is 40 tons. At a price of 300 SF/Kg the total Xenon cost is about 12 Msf. However, the Xenon can be reused after this experiment and thus represents a capital investment on which interest ($\approx$10 %/yr) would be paid. This R & D project, directed by T. Ypsilantis and J.Séguinot, has been recently funded by the LAA collaboration at CERN.

References

[1] R. Brun, F. Bruyant, M. Maire, A.C. McPherson, P. Zanarini "Geant3", CERN report DD/EE/84 – 1, September 1987.

[2] W. Sippach, G. Benenson, B. Knapp, IEEE Trans. Nucl. Sci., NS-27, 578 (1980); H. Cunitz, Y. Hsiung, B. Knapp, W. Sippach, "Data-Driven Processing", in Proceedings of the International Conference on Instrumentation for Colliding Beam Physics, SLAC Report 250, June 1982.

[3] For large-scale applications of these methods, see: L. Borten et al., "A Data-Driven Parallel Pipelined Hardware Reconstruction Processor" (page 45) and D.M. Kaplan, "A Parallel, Pipelined Event Processor for Fermilab Experiment 605" (page 31); Proceedings of the Symposium on Recent Developments in Computing, Processor and Software Research for High-Energy Physics (Guanajuato, Mexico, May 8-11, 1984).

[4] J.G. Zweizig et al.(UA8 Collaboration); Nucl. Instruments & Methods A263 (1988)188.

[5] H.-U. Bengtsson, G. Ingelman, Comput. Phys Commun. 34 (1985) 251; H.-U. Bengtsson, T. Sjostrand, Comput. Phys Commun. 46 (1987) 43.

[6] P. Chauvat et al., Phys. Rev. Lett. 199B (1987) 304.

[7] G. Bellettini, private communication (1988).

[8] D. Bettoni et al.,Nuclear Instruments and Methods A252 (1986) 272.

[9] C. Young et al., IEEE NS36 (1986).

[10] W. Zimmerman et al., Nuclear Instruments and Methods A243 (1986) 86.

[11] J.Seguinot and T.Ypsilantis , Proposal to LAA for the development of a fast ring-imaging Cherenkov Detector with local readout for use on a hadron collider, 24 september 1987.

[12] R.Arnold et al., NIM A270, 255 and 288 (1988).

[13] S. Kleinfelder et al., A Flexible 128 Channel SSD Instrumentation Integrated Circuit with Sparse Data Readout, Proceedings of IEEE NSS Conference (October 1987) San Francisco.

[14] A. Seiden (private communication about Univ. of California, Santa Cruz chip). G. Lutz et al., Nuclear Instruments and Methods A263 (1988) 163. J. T. Walker et al., Nuclear Instruments and Methods 226 (1984) 200.

[15] J. Ellett, VIRTUS: A Multi-Processor Event Selector Using FASTBUS, Proceedings of the 1983 DPF Workshop on Collider Detectors (LBL-15973), p. 185; J. Ellett et al., "VIRTUS, A Multi-Processor System in FASTBUS", Computing in High Energy Physics (Ed., L.O. Hertzberger and W. Hoogland, North Holland-1986), page 235.

[16] UA1 Collaboration, Presented at $p\bar{p}$ Workshop at Fermilab (June 1988).

[17] K. Ellis, Talk at $p\bar{p}$ Workshop at Fermilab (June 1988).

[18] H. Schroeder, Rapporteur Talk at XXIV International Conference in High Energy Physics, (August 1988 - Munich, FRG) and DESY 88-101 (1988).

[19] D. Hitlin, Proceedings of the Electron Photon Conference, DESY 1987.

[20] G.J. Alner et al. (UA5 Collaboration), Physics Reports 154 (1987) 247.

[21] T. Doke et al., Nucl. Instruments & Methods A235 (1985) 136; H.J. Crawford, Nucl. Instruments & Methods A256 (1987) 47.

[22] V. Peskov et al., Nucl. Instruments & Methods A269 (1988) 149.

APPENDIX C

EUROPEAN ORGANIZATION FOR NUCLEAR RESEARCH

CERN-SPSC/89-43
SPSC/P238Add.1
16 August 1989

Addendum to Proposal P238:

MEASUREMENT OF B_s MIXING

A. Brandt, S. Erhan, D. Lynn, M. Medinnis, P. Schlein*, J. Zweizig
University of California, Los Angeles, U.S.A.

T. Ypsilantis
College de France[1], Paris, France

G. Borreani
University of Ferrara and INFN[2], Italy

A. Kaschuk, V. Samsonov, V. Sarantzev, E. Spiridenkov, A. Vorobyov
Institute for Nuclear Physics, Gatchina, Leningrad, U.S.S.R.

M. Calvetti
University of Perugia and INFN[2], Italy

J.B. Cheze, J. Zsembery
Centre d'Etudes Nucleaires – Saclay[3], Gif-sur-Yvette, France

R. Dzhelyadin, Y. Guz, V. Kubic, V. Obraztsov, A. Ostankov
IHEP-Serpukhov, Protvino, U.S.S.R.

C. Biino, R. Cester, A. Migliori, R. Mussa, S. Palestini
University of Torino and INFN[2], Italy

ABSTRACT

We report the results of a detailed investigation into the capability of our proposed forward B-spectrometer experiment to observe and measure the time oscillations in the decay of tagged B_s mesons. With the best conceivable electromagnetic calorimeter resolution ($0.5\%/\sqrt{E}$ for Liquid Xenon) and with both outgoing collider arms instrumented, 9000 reconstructed B_s are obtainable per 10 pbarn^{-1} integrated luminosity. Lead-Glass calorimetry with $4\%/\sqrt{E}$ leads to 6000 events. Charged kaons are shown to tag 58% of these events with an adequate (good tag/all tag) ratio of 73%. Using Lead-Glass calorimetry with only one instrumented arm, $\Delta M/\Gamma$ would be measured with 3000 events, for values up to 15 or more, with an error of about ± 0.1. Our conclusion is that superior mixing measurements can be performed with the proposed apparatus.

*) Spokesman
1) Pending approval of the Laboratory and IN2P3
2) Pending approval of INFN
3) Pending approval of CEN-Saclay

TABLE OF CONTENTS

APPENDICES

1. INTRODUCTION

The Forward Beauty Spectrometer in proposal P238 has the following properties:

- Real-time vertex calculations based on silicon micro-vertex detector data yield the suppression of minimum bias background necessary for efficient triggering on beauty particles.
- The average momentum of detected and reconstructed B-mesons is about 35 Gev/c and the B proper time can be measured with a precision better than $\sigma_t/t = 6\%$. These facts allow excellent B-$\bar{B}$ oscillation studies to be made.
- Particle identification is furnished offline with a system of liquid and gas Ring Imaging Cerenkov Counters.
- The forward peaking of heavy flavor particles should be even more pronounced at the higher energy UNK, LHC and SSC colliders. Thus, our proposed experiment would be a first example of an important class of future beauty experiments which should eventually allow an effective search for CP violation in B decay.

In document P238, we presented details of the trigger design and detector which would furnish more than 2×10^5 reconstructed B-Mesons per 10 $pbarn^{-1}$ integrated luminosity at the CERN SPS-Collider with $\sqrt{s} = 630$ GeV.

In the present Addendum to P238, we examine in detail the suitability of our proposed experiment for a measurement of B_s-$\bar{B}_s$ oscillations. We find a capability which is superior to that of any other existing or proposed experiment.

Chapter 2 contains a discussion of the relevant mixing formalism. Chapter 3 contains a discussion of the acceptance properties of the proposed apparatus, a performance summary of the trigger and the reconstruction efficiencies for B_s mesons. The expected yields are given.

Chapter 4 contains the results of a Monte-Carlo study of flavor tagging procedures in which it is shown that charged kaons can be used to tag 58% of all reconstructed B_s mesons. The B_s lifetime measurement is described in Chapter 5. In Chapter 6 we present mixing analyses of simulated Monte-Carlo data samples, which would result from runs with integrated luminosity of 10 $pbarn^{-1}$, and define the minimum hardware capabilities necessary for a satisfactory measurement with a reasonable "margin of safety".

In Chapter 7 we discuss, as best we can with the available information, the apparent capabilities of other existing or planned beauty experiments to measure B_s-mixing.

We conclude that superior mixing measurements can be performed with the proposed apparatus at the SPS-Collider.

2. THE OBSERVATION OF B_s MIXING

Four proper time distributions will be obtained from the reconstructed and tagged B_s and $\bar{B}_s$ mesons:

$$t^+ \; B_s(t) \tag{1}$$

$$t^- \; B_s(t) \tag{2}$$

$$t^+ \; \bar{B}_s(t) \tag{3}$$

$$t^- \; \bar{B}_s(t) \tag{4}$$

where t^+ and t^- denote the two charges of the possible tagging particles (e.g., e^+, e^-, μ^+, μ^-, K^+, K^-). We note that, since a B_s can be produced together with a $\bar{B}_u$, $\bar{B}_d$ or $\bar{B}_s$, a tagging particle can arise from any one of these. The latter two states are themselves subject to oscillation and can lead to the wrong sign tag, refered to in this document as "mistagging". Other sources of mistagging are, for example, background under the B_s signal, other physics sources of the tagging particles, etc. Tagging procedures are discussed in Chapter 4 in some detail.

In order to arrive at the equations which describe the above four distributions (ignoring the possibility of CP violation), we start by expressing B^0 and $\bar{B}^0$ as the usual linear combination of mass eigenstates, B_1 and B_2:

$$|B^0> \; = \; [|B_1> \; + \; |B_2>] \, / \, \sqrt{2} \tag{5}$$

$$|\bar{B}^0> \; = \; [|B_1> \; - \; |B_2>] \, / \, \sqrt{2} \tag{6}$$

With the $B^0 \leftrightarrow \bar{B}^0$ transitions allowed by the second-order weak interaction (box diagram), we have as the time-evolved state for an initial B^0:

$$\psi(t) = [e^{-iM_1t-\Gamma_1t/2} \cdot |B_1> \; + \; e^{-iM_2t-\Gamma_2t/2} \cdot |B_2>] \, / \, \sqrt{2} \tag{7}$$

Expanding $|B_1>$ and $|B_2>$ in terms of the observed $|B^0>$ and $|\bar{B}^0>$ states, and projecting out their amplitudes, we have as the probabilities to see B^0 and $\bar{B}^0$:

$$|<B^0|\psi(t)>|^2 \; = \; e^{-\Gamma t} \cdot [1 \; + \; \cos(\Delta Mt)] \, / \, 2 \tag{8}$$

$$|<\bar{B}^0|\psi(t)>|^2 \; = \; e^{-\Gamma t} \cdot [1 \; - \; \cos(\Delta Mt)] \, / \, 2 \tag{9}$$

We write in (8) and (9), $\Gamma \equiv \Gamma_1 = \Gamma_2$, because of the large phase space available in B decay, and $\Delta M = M_1 - M_2$. As required, the sum of equations (8) and (9), $e^{-\Gamma t}$, describes the untagged B_s decay.

Integrating Eqs. 8 and 9 over time, we find that the rates for no-oscillation and oscillation, respectively, go as $(2+x^2)/(1+x^2)$ and $x^2/(1+x^2)$, where $x \equiv \Delta M/\Gamma$. If we assume, as is reasonable, that a B_s and its accompanying $\bar{B}$ decay independently and that we only measure the time dependence of the B_s, then the correct expressions to describe the tagged time distributions in Eqs. 1-4 are just Eqs. 8 and 9 multiplied by the appropriate time-averaged rate. These are shown in Table 1 for the four cases of Eqs. 1-4 and for the two possible initial states.

Krawczyk et al. (DESY 88-16) have pointed out that if data in Reactions 2 and 3 (or Reactions 1 and 4) are added together, the time dependences, $[1 \pm \cos(\Delta Mt)/(1+x^2)]$, result. This can be seen to be the case from the relations in Table 1, independently for each of the two possible initial states. What we can see in addition, however, is that, if the initial states, $B\bar{B}_s$ and $\bar{B}B_s$ occur with equal probability, this occurs independently for each of Reactions 1-4, as shown in column 4 of Table 1.

Table 1: Joint Time-Integrated, Time-Dependent Rates(a,b,c)

Final State	Initial State $B\bar{B}_s$	Initial State $\bar{B}B_s$	Equal Sum
$t^+ \; B_s(t)$	$(2+x^2)\cdot[1-\cos]$	$x^2 \cdot[1+\cos]$	$1-[1/(1+x^2)]\cdot\cos$
$t^- \; B_s(t)$	$x^2 \cdot[1-\cos]$	$(2+x^2)\cdot[1+\cos]$	$1+[1/(1+x^2)]\cdot\cos$
$t^+ \; \bar{B}_s(t)$	$(2+x^2)\cdot[1+\cos]$	$x^2 \cdot[1-\cos]$	$1+[1/(1+x^2)]\cdot\cos$
$t^- \; \bar{B}_s(t)$	$x^2 \cdot[1+\cos]$	$(2+x^2)\cdot[1-\cos]$	$1-[1/(1+x^2)]\cdot\cos$

(a) The B decay which provides the tagging particle is time-integrated. The B_s decay is time-dependent. Throughout this table, $x = \Delta M/\Gamma$ for the tagging B
(b) We note that in a B decay, for example, a μ^+ or a K^+ tag results (if the K results from the $\bar{c} \to \bar{s}$ transition). In a tagging $\bar{B}$ decay, of course, the signs are opposite.
(c) To simplify the reading of this table, a common factor $e^{-\Gamma t}/(1+x^2)$ is suppressed in all terms in columns 2 and 3, as is the argument, (ΔMt), from all cosine functions.

Thus the distributions for the four Reactions must be pairwise identical if valence quarks do not play a role in modifying the equality of the initial states (presumably the case for production of B_s at small Feynman-x).

It remains to be pointed out, as in Krawczyk et al., that since the accompanying B (or $\bar{B}$), which provides the tagging particle, can be either B_u, B_d or B_s, the factor $[1/(1+x^2)]$ in the relations in the last column of Table 1 must be weighted over the three types of tag-producing B's according to their relative production frequency. In calculating the weighted average of $[1/(1+x^2)$ over B_u (40%), B_d (40%) and B_s (20%), x is taken to be 0, 0.7 and 15, respectively.

The resulting constant, K = 0.67, is essentially a "dilution" factor since it decreases the amplitude of the oscillation from the value it would have were the flavor of the decaying B always correctly determined. For example, the observed distribution from, for example the $t^+ \; B_s(t)$ final state, now has the form: $1 - K\cos(\Delta Mt)$. Other contributions to dilution come from mistagging or background (the tagging problem is discussed in detail in Chapter 4). For example, if the tag used is only 70% efficient (good/all = 70%), then K receives another multiplicative contribution of (good − bad)/all = 0.4. The effective value of the constant, K, is discussed in Chapter 6, where we present the complete analysis of simulated data samples.

3. YIELDS OF RECONSTRUCTED B_s AND $\bar{B}_s$ MESONS

Most of the ingredients for a realistic estimate for B_s yields can be found in Proposal P238. See, for example, Section 8.1 (page 54). Here we list, in Table 2, the various steps which result in an estimate of 4500 reconstructed B_s and 4500 reconstructed $\bar{B}_s$ mesons per 10 $pbarn^{-1}$ integrated luminosity. We note that these numbers represent the "ultimate capability" of the SPS-Collider, namely if both outgoing arms are instrumented and if the best conceivable electromagnetic calorimeter is used (Liquid-Xenon). As is discussed below, while maximum statistics and minimal background are clearly always desirable features, a proper measurement of B_s mixing can be made with less than this maximum commitment. The following two sections explain the various steps in arriving at the estimates.

Table 2: B_s & $\bar{B}_s$ Event Yields(*)

10^8 $b\bar{b}$ Produced for $\int \mathscr{L} dt = 10\ pbarn^{-1}$

2.0×10^7 B_s	2.0×10^7 $\bar{B}_s$	0.20 = B_s Production
6.0×10^6	6.0×10^6	0.30 = 2-Arm Geometrical Acceptance
3.0×10^5	3.0×10^5	0.05 = $BR(B_s \rightarrow D_s^* n\pi^{\pm})$
3.0×10^5	3.0×10^5	1.00 = $BR(D_s^* \rightarrow D_s \gamma)$
4.4×10^4	4.4×10^4	0.15 = $BR(D_s \rightarrow KK\pi, KK3\pi, K^0K)$
3.0×10^4	3.0×10^4	0.68 = No Other Interaction in Bunch Crossing
2.8×10^4	2.8×10^4	0.94 = Vertex Acceptance of Silicon μVertex
1.18×10^4	1.18×10^4	0.42 = Trigger Efficiency (D_s^* 3π)
1.05×10^4	1.05×10^4	0.89 = Track Finding Efficiency
4500 B_s	4500 $\bar{B}_s$	0.43 = Event Reconstruction This assumes best e.m. calorimetry. See text for further discussion.

(*) The cuts in this table are discussed in Section 3.1

3.1 Geometric Acceptance, Branching Ratios & Trigger Efficiencies

As in P238, we base our yield estimates on an assumed integrated luminosity, $\int \mathcal{L} dt = 10$ $pbarn^{-1}$, and a $b\bar{b}$ total cross section of 10 μbarn. These assumptions correspond to a $b\bar{b}$ production sample of 10^8 events. The following losses and efficiencies are tabulated in Table 2:

- A $\bar{b}$-quark is assumed to have a 20% probability of combining with an s-quark to make a B_s-meson. This leads to 2×10^7 B_s and 2×10^7 $\bar{B}_s$ mesons produced, with negligible simultaneous production.

- Geometric Acceptance – According to PYTHIA (which assumes $b\bar{b}$ production via gluon-gluon fusion and quark-quark fusion), the decay products of 30% of all produced B_s mesons are fully contained by a system of two 600 mrad aperture forward spectrometers. This leads to 6.0×10^6 B_s and 6.0×10^6 $\bar{B}_s$ produced and fully contained in the aperture (these numbers are slightly smaller than the 6.4×10^6 given on page 55 of P238, due to a recalculation of the geometrical acceptance for the specific B_s decay mode discussed below).

- B_s Branching Ratios – We assume BR = 5% for the total of all reactions of the type:

$$B_s \rightarrow D_s^* + n\pi^\pm$$

  This leads to 3.0×10^5 B_s (and the same number of $\bar{B}_s$) with these decay modes. We noted in Table 7, page 56 of P238 that the observed ARGUS BR = 6.7% for reactions of the type $B_d \rightarrow D^* + n\pi$ with n = 1,2,3. It seems likely that we shall also be able to reconstruct such final states with n > 3 and that, therefore, our effective useful BR will be larger than the 5% assumed.

- D_s^* Branching Ratio – We assume that all D_s^* decay via the mode:

$$D_s^* \rightarrow D_s \gamma$$

  This has the consequence that an electromagnetic calorimeter is essential for this experiment. The characteristics of the calorimetry required for the effective reconstruction of these events are discussed in the following section. (Note that with such calorimetry, we also acquire the capability to detect $D^{*0} \rightarrow D^0\gamma$ (BR = 48%) and gain additional efficiency for charged D^* in $D^{*+} \rightarrow D^+\gamma$ (BR = 17%)).

- $D_s^\pm$ Branching Ratio – We take BR = 15% for all known charged final states ($K^+K^-\pi^\pm$, $K^+K^-\,3\pi$, $K^0K^\pm$). This reduces each sample to 44,250 events.

- Pileup loss – As in P238 (see page 55 and Section 3.2), 68% of all B_s events have no second inelastic interaction in the same bunch crossing at an average luminosity of 2×10^{30} cm^{-2} sec^{-1}. For purposes of the present estimates, we assume that all events in bunch crossings which contain more than one inelastic interaction will be lost (in practice, however, since many of multiple interaction bunchs may be usable, 68% is a conservative estimate of this efficiency). The B_s sample is reduced to 30,090 events.

- Vertex Acceptance in Silicon – About 6% of events have vertices outside the acceptance range in longitudinal coordinate, z, of the silicon micro-vertex detector (see Appendix B) and are therefore lost. The samples are thus reduced to 27,682 events each.

- Trigger Efficiency – The trigger simulation is discussed in detail in Chapter 4 of P238 with some results given in Chapter 7. For the present estimates, we have focussed our attention on one particular final state:

$$B_s \to D_s^* \pi\pi\pi$$
$$\quad \hookrightarrow D_s \gamma$$
$$\quad\quad \hookrightarrow \phi\pi$$
$$\quad\quad\quad \hookrightarrow K^+K^- \qquad (10)$$

We calculate a trigger efficiency of 42% for this state. This may be compared with the results given in Table 6 (page 51) of P238 of 47% for $B_d \to D^*\pi\pi\pi$ (8 tracks) and 41% for $D^0\pi\pi$ (6 tracks). The samples are thus reduced to 11,627 each.

- Track Finding Efficiency — We assume a 98% track finding efficiency and therefore $(.98)^n$ for the entire event. For the above 6-track event, this efficiency is 88.6%, which reduces each sample to 10,301 events.

- Reconstruction Efficiency — An efficiency of 43% follows from the analysis discussed in the following section when an electromagnetic calorimeter with resolution $\sigma_E/E = 0.5\%/\sqrt{E}$ is used (Liquid-Xenon, as discussed in Appendix D of P238). 43% is somewhat larger than the 36% reported for the decay $B \to D^*3\pi$ in P238 (page 51), because of some improvements in reconstruction software. For other calorimeters (Lead-Glass, etc.), the reconstruction efficiency is smaller, as discussed in the following section.

3.2 B_s Reconstruction: Signal & Background Estimates

Chapter 7 of the P238 proposal discussed the B-meson reconstruction procedure and combinatoric background problem in some detail. The present analysis of the $D_s^* \to D_s\gamma$ reaction requires the introduction of a new factor, namely the effect of using electromagnetic calorimeter information in the B_s-meson reconstruction. We have thus studied the effect of calorimeter energy and spatial resolutions on both the reconstruction yield and the B_s signal/background ratio.

Following the procedures outlined in Chapter 7 of P238, we construct the invariant mass difference, $M(D_s^*) - M(D_s)$ for the B_s decay in Reaction 10. We plot the resulting mass difference distributions in Fig. 1 for 12 combinations of calorimeter parameters. Calorimeter energy resolutions of 0.5%, 1%, 2% and 4% and spatial resolutions of 0.3 mm, 1.0 mm and 10 mm are considered. In constructing these plots, we randomly vary all charged track and γ parameters in accordance with the expected energy and angular resolutions. Since the purpose of these plots is to demonstrate the effect of different calorimeter resolutions on the invariant mass resolution, we do not include the combinatoric background resulting from all possible track combinations — only the correct B_s decay tracks are used.

Although there is very little dependence of the invariant mass difference resolution on calorimeter spatial resolution seen in Fig. 1, there is a very large dependence on its energy resolution. For the $0.5\%/\sqrt{E}$ calorimeter (e.g.: the Liquid-Xenon device discussed in Appendix D of P238), the FWHM is 2 MeV, while for $4\%/\sqrt{E}$ (Lead-Glass), the FWHM is increased to about 12 MeV. As will be demonstrated below, the effect of this poorer resolution is to allow more combinatoric background into the signal region and also to lose some signal because some of the tails in the $M(D_s^*) - M(D_s)$ distribution will be cut off. In addition, a larger fraction of the γ's from D^*'s combine with other γ's in the event to form a π^0 mass; these are then cut out in our selection procedure.

Using appropriate mass cuts in Figs. 1 to select most of the signal peaks leads to the B_s invariant mass distributions shown in Figs. 2 for the same sets of calorimeter parameters. Although there is a significant dependence of the mass resolution on calorimeter parameters, the dependence is weak, due to the fact that, in general, the γ possesses only a small part of the B_s energy (average γ energy is about 1 GeV, compared with average B_s energy of about 35 GeV).

Before discussing the matter of how the signal/background depends on calorimeter resolution, we show in Fig. 3(a) the expected B_s signal for the best calorimeter case ($0.5\%/\sqrt{E}$ and 0.3 mm), with all combinatoric background (obtained as described in Chapter 7 of P238). Fig. 3(b) shows the expected D_s signal with its combinatoric background.

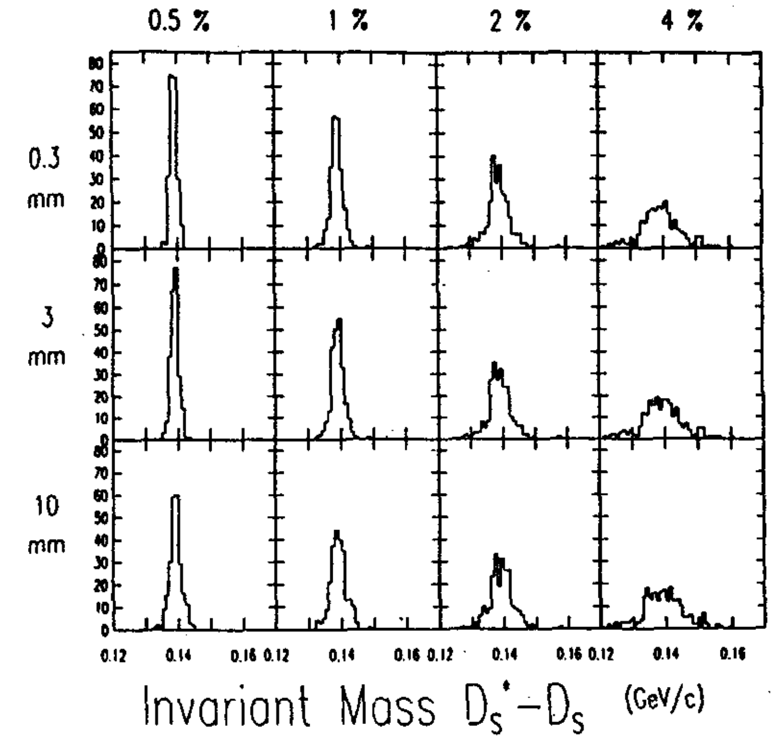

Figure 1: Invariant mass differences, $M(D_s^*) - M(D_s)$, for the indicated 12 combinations of electromagnetic calorimeter energy and spatial resolutions. The spatial resolution is the standard deviation, σ_X. The mass bins are 1 MeV. No combinatoric background is shown. In each case, the energy resolution σ_E/E is the indicated constant (e.g. k = 0.5%) divided by $\sqrt{E}$ in GeV.

The B_s signal size and signal/background have been evaluated for all of the 12 sets of calorimeter resolutions considered (we include the expected background from the general B event sample, in addition to the combinatoric background arising from Reaction 10). Figs. 4(a,b), respectively, contain these results. For the $0.5\%/\sqrt{E}$ calorimeter, the event yield is 9000 total reconstructed B_s and $\bar{B}_s$ events and the signal/background is about 10. The degradations of both these quantities with worsening calorimeter energy resolution are clear. In particular, for a $4\%/\sqrt{E}$ calorimeter (Lead-Glass), the event yield drops to 6000 events and the signal/background to about 4. The question of what calorimeter resolution will allow the extraction of our desired physics results is deferred to Chapter 6 of this document where we give the results of maximum likelihood fits to Monte-Carlo data samples of varying sizes and with varying backgrounds.

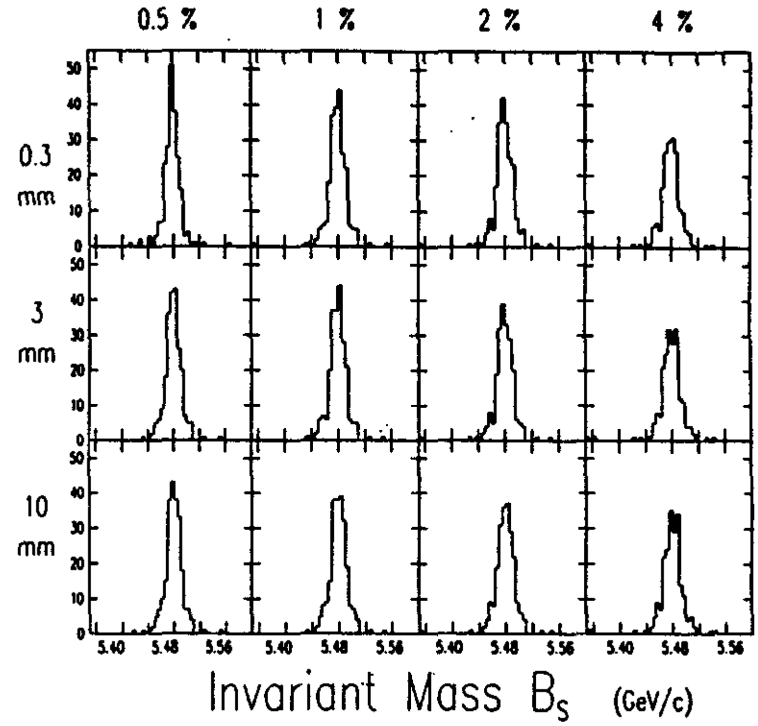

Figure 2: Reconstructed B_s Invariant Mass for the indicated 12 combinations of electromagnetic calorimeter energy and spatial resolutions as in Fig. 1. In each case, an appropriate cut is made on the mass difference, $M(D^*) - M(D_s)$, of the corresponding plot in Fig. 1. The mass bins are 5 MeV. No combinatoric background is shown.

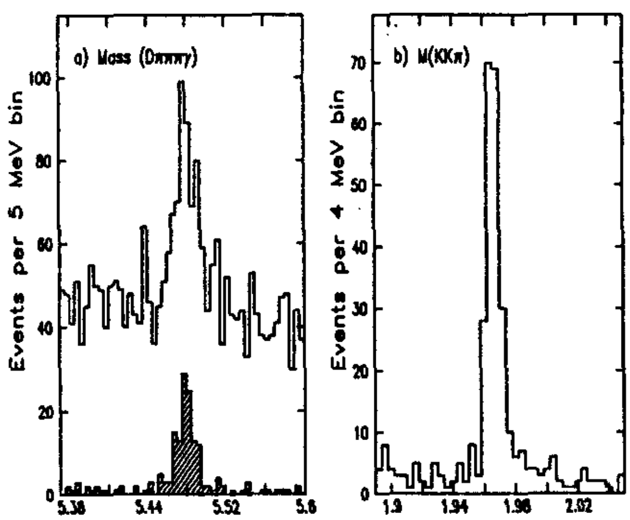

Figure 3: (a) Reconstructed $D^*\pi\pi\pi$ invariant mass and (b) $KK\pi\gamma$ invariant mass. Both plots assume calorimeter energy resolution $\sigma_E/E = 0.5\%/\sqrt{E}$ and position resolution = 0.3 mm. All expected combinatoric background is shown.

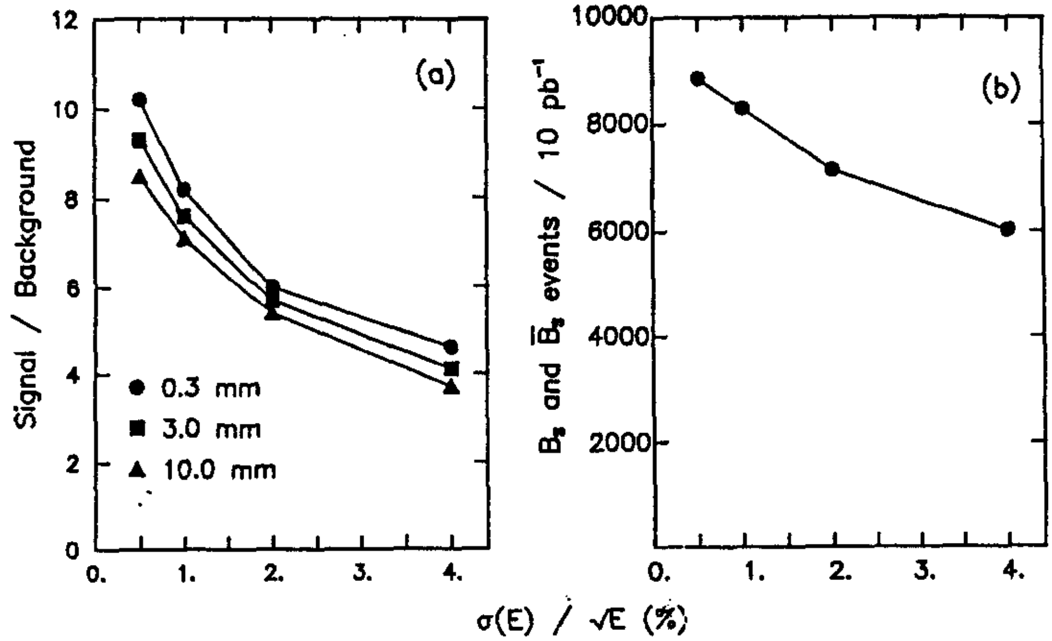

Figure 4: Event yield and Signal/background vs. Calorimeter Resolution: (a) Signal/Background. The dependence is shown vs. k in $\sigma_E/E = k\%/\sqrt{E}$. Curves are given for three different spatial resolutions of the calorimeter. (b) Number of signal events vs. k (for a two arm system).

4. FLAVOR TAGGING

4.1 The Use of Muon Tags

In order to understand the tagging possibilities using leptons, we consider two questions, which we then attempt to answer with the use of the Monte-Carlo event generator, PYTHIA 5.1:

1. For events in which a B_s is detected in a 600 mrad spectrometer, what are the momenta and laboratory angles of accompanying leptons? This question is answered in Fig 5, which is a scatter plot of p_μ vs. θ_μ for events containing both an accepted B_s and a muon with at least 1.2 GeV p_t. The expected correlation between μ and B_s is clearly visible. Most muons are in the same hemisphere as the B_s detected at 0° and correlated within ~ 1 unit of rapidity. Furthermore, the muons within the spectrometer aperture of 34.9° (600 mrad) are seen to have much larger momenta than those outside the spectrometer. We conclude that, for detected B_s in the 600 mrad spectrometer, there is not much to be gained by constructing additional lepton detection outside the 600 mrad aperture.

2. What is the momentum and direction of B_s mesons associated with muons detected by a central muon detector, for example the UA1 detector which can identify muons in the pseudorapidity range $|\eta| < 2$ and transverse momentum range $p_{t\mu} > 3$ GeV? This question is answered with reference to Fig. 6, which is a scatter plot of momentum (p_B) vs. laboratory angle

(θ_B) for B_s mesons associated with muons in the above kinematic range. There remains a strong polar preference for the direction of the B_s. Those B_s's with $\theta_B < 600$ mrad have substantially higher momenta than those outside the spectrometer aperture, whose average momentum is less than 10 GeV. The mean flight path for B_s mesons accepted by the spectrometer is ~ 2.5 mm, compared to ~ 0.6 mm for B_s mesons outside the spectrometer. Thus, for optimum triggering, reconstruction and resolution, the B_s's of choice for mixing measurements are those seen by our proposed detector.

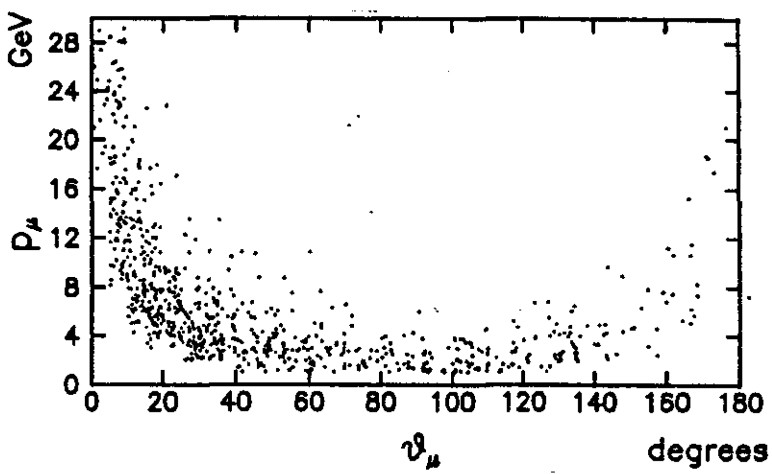

Figure 5: Lab momentum vs. lab angle of muons accompanying an accepted B_s. In this plot, the detected B_s is on the 0° side. Additionally, the muons are required to have $p_t > 1.2$ GeV.

Some properties of Figs. 5 and 6 are summarized in Table 3, for events in which a B_s meson is fully accepted in the 600 mrad aperture. For each of five different requirements on θ_μ and $p_{t\mu}$, the fraction of tagged B_s mesons is given together with the tagging quality (this is the fraction of those tagged B_s which are tagged by a muon with correct sign). We note here that, following the discussion given in Chapter 2 on mistagging, the contribution to the dilution factor, K, which governs the oscillation amplitude, is given by: (good tags − bad tags)/all tags.

In the first row of Table 3, there are no restrictions on either θ_μ and $p_{t\mu}$. Thus, the fraction tagged (22%) is nearly equal to the semi-leptonic decay probabilities of the second B, both for the $b \to c$ transition and the $c \to s$ transition (= 11.2% + 6.7%) (the equality is not exact since more than one muon is present in some events). The good/all ratio is 54% for this class of events, indicating that no useful lepton tagging can result from the complete lepton sample without a $p_{t\mu}$ cut (K ~ 0).

Case B, which has a relatively modest $p_{t\mu}$ cut, tends to exclude leptons from charm decay, thereby increasing the percentage of good tags to 81%, but loses ~ 2/3 of the leptons. Case C, which corresponds approximately to the UA1 muon trigger, has a very good tagging efficiency, although only 1.4% of the B_s mesons are tagged (we emphasize that in the generation of these events, we have not "tuned" PYTHIA to agree with UA1 measurements).

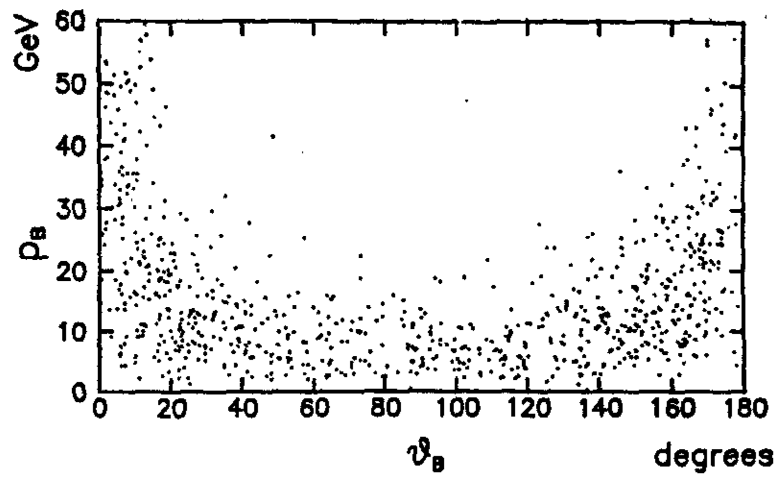

Figure 6: Lab momentum vs. lab angle of B_s mesons for events containing a muon with p_t > 3 GeV and $|\eta|$ < 2.

*Table 3: Flavor tagging of Accepted B Mesons with Muons**

	Angular Range	pt Range (GeV)	Fraction Tagged	Good/All	Comments
A	all	all	.22	.57	Useless
B	$\lvert\eta\rvert < 2$	> 1.2	.061	.81	
C	$\lvert\eta\rvert < 2$	> 3.0	.014	.91	"UA1-like" trigger
D	θ < 600mrad	all	.12	.56	Useless
E	θ < 600mrad	> 1.2	.047	.82	Possible with P238

(*) All entries in this table are calculated with PYTHIA 5.1. No attempt was made to tune, for example, the muon p_t distribution with that measured by UA1.

Case D, in which the tagging muon is required to be in the 600 mrad aperture, but in which no selection on $p_{t\mu}$ is made, is useless since the tagging efficiency is ~ 50%, as in case A. If the modest

1.2 GeV $p_{t\mu}$ cut is added (case E), the tagging efficiency increases to an acceptable 83%. The disadvantage of this tagging method is that only 4.7% of the accepted B_s's are tagged.

Although this study considered only muons, both muons and electrons could, in principle, be used as tags. If electron tags were added, the fraction of tags could increase to an upper limit of 9.4% in Case D. However, additional losses arise from Cerenkov limitations and various cuts, needed to minimize the background coming from sources such as pion decay and Dalitz electrons. We have not attempted to estimate these losses since, as discussed in the next section, the use of kaon tags looks more promising and we intend to rely on kaons rather than leptons to tag the B_s flavor.

4.2 The Use of Kaon Tags

We have investigated the possibility of using charged kaons as tags. Our overall strategy is to assign a tag based on the sign of kaons found in the spectrometer and based on whether or not the found kaon tracks, as measured in the vertex detector, point to the primary vertex. We consider below various schemes for handling this information. All calculations are done with PYTHIA 4.7.

There are two major sources of kaons in an event which contains a reconstructed B_s. They either come from the accompanying B meson or they come from the primary vertex. We refer to these as "secondary kaons", K_s, and "primary kaons", K_p, respectively. In general, there is a "good" version and a "bad" version of each. This refers to whether their sign correctly tags the flavor of the produced B_s meson or not.

1. Good K_s: kaons which contain the s-quark at the end of the $b \to c \to s$ chain correctly tag the flavor of the accompanying B-meson at decay.. These kaons will often be measured to be inconsistent with pointing to the primary vertex. However, when the flight path of the accompanying B is too short for this to be the case, the kaon will incorrectly be called a primary kaon and will give a bad tag.

2. Bad K_s: kaons arising from the $W^\pm$ in either the $b \to c$ or the $c \to s$ transition can have either sign. Since they will often be measured as being inconsistent with pointing to the primary vertex, they produce a background for the good K_s tags discussed in the first point.

3. Good K_p: these kaons contain the $\bar{s}$-quark which is created in association with the s-quark contained in the B_s meson and can also be used as tags (Note, however, that the sign of these kaons is opposite to those kaons in point 1. Here a $K_p = K^-$ implies a $\bar{B}_s$ meson.) These kaons will in general be produced nearby in rapidity to the reconstructed B_s meson and can be distinguished from the kaons in point 1 since they are produced at the primary vertex. They have an advantage over K_s's from the decay of the accompanying B, in that they suffer no oscillation effects.

4. Bad K_p: kaons produced from the $s\bar{s}$ sea in the numerous hadronization processes at the primary vertex are not associated with the B_s or $\bar{B}_s$ mesons. Such kaons can be of either flavor and thus dilute the kaon tagging. These kaons are particularly troublesome for the tags discussed in point 3 since they are also associated with the primary vertex.

We have studied possible tagging schemes with PYTHIA generated events which contain a B_s meson decaying according to Reaction 10 in Section 3.1. No requirements are made on the hadronization or decay of the associated b-quark. As described in the P238 proposal, events are passed through our trigger simulation software and the B_s is reconstructed. We next sort the kaons, which are accepted by the spectrometer, according to charge and check if the kaon track is consistent with pointing to the primary vertex, using the software simulation package for the micro-vertex detector and online algorithm. Those kaons which are consistent with coming from the primary vertex are K_p; those which are inconsistent are called K_s.

Table 4 contains the results of a study of 313 reconstructed B_s mesons in the form of a matrix. The top row contains events in which no correct tag was found. The second row contains events in which one (or more) good K_s tag is found. The third row contains events in which one (or more) good K_p tag is found. The bottom row contains events which contain both good K_s and K_p tags. Similarly, the first column contains events in which no bad tags are found. The second column contains events with bad K_s tags. The third column contains events with bad K_p tags and the fourth contains events with both bad K_s and K_p tags. Note that, since the event generator program, PYTHIA, contains no B oscillation effects in it, it is possible to know for each event, what constitutes a good tag or a bad tag.

Table 4: *Numbers of Good vs. Bad Kaon Tags in 313 B_s Events**

		Bad tags			
		none	K_s	K_p	both
Good Tags	none	84	18	22	5
	K_s	41	(23)	12	[2]
	K_p	51	1	(18)	[1]
	both	16	[5]	[8]	(6)

(*) Note that events in round brackets, ( ), have one pair (or both) of either K_s^+ and K_s^- or K_p^+ and K_p^-. They provide no tagging information and can be dropped from the table. Events in square brackets, [ ], have in addition to such pairs, also one (or more) K_s or K_p. These events therefore provide unique tags and can be added to the appropriate tagged event samples in the first column or first row.

The reduction of Table 4 is facilitated by the observation that several categories have, as indicated in the footnote in the Table, both secondary K^+ and K^- or both primary K^+ and K^-. These pairs obviously provide no tagging information and can be dropped from further consideration or, if there is an additional K_s or K_p in the event, added to the appropriate first column or first row entry. After these steps, we are left with 12 events in the category, good K_s and bad K_p, and 1 event in the category, bad K_s and good K_p. For these events, a correct tagging statement is clearly made by giving priority to the K_s.

With the steps outlined in the previous paragraph, we are able to form Table 5, which is a list of all uniquely tagged events. There are 3 types, those where the tag is provided by a K_s or K_p, respectively, and those where both both agree. The total number of tagged events is 182 events which is 58% of the total 313 events. All types have approximately the same tagging efficiency, which is 73% for the total sample.

In conclusion, we find that we can use kaons found in the spectrometer to tag more than half of all events containing a reconstructed B_s meson. This is more than a factor of five larger than the best

Table 5: Kaon Tagging Efficiencies

	Events	Fraction Tagged	Good Tags	Bad Tags	Good/All
K_s	81	.26	61	20	.75
K_p	80	.26	56	24	.70
K_s and K_p	21	.07	16	5	.76
Total	182	.58	133	49	.73

we can hope for with a lepton tag. The "trick" which makes this possible is the segregation of primary vertex kaons from kaons originating from secondary vertices by using impact parameter information provided by the silicon vertex detector. Our estimates of the primary tags depend heavily on PYTHIA's hadronization scheme. Nevertheless, our conclusion remains that tagging with kaons is probably much more efficient than tagging with leptons.

5. MEASUREMENT OF B_s LIFETIME

The mean reconstructed B-meson momentum of about 35 GeV/c (see Fig. 6 in P238) and the mean distance of 2 cm between event vertices and first silicon detector plane (see Appendix B in this document) allow rather good measurements of proper flight time for each event.

Fig. 7 displays the simulated proper time distribution (in units of B mean life) expected for the 9000 event total B_s and $\bar{B}_s$ data sample obtainable in a 10 $pbarn^{-1}$ run with a single arm instrumented and using Lead-Glass calorimetry. This distribution shows the fitted curve used for maximum likelihood fits described in the next chapter.

It is seen in Fig. 7 that we have excellent acceptance in t above about one mean life. The departure from a pure exponential in Fig. 7 illustrates the combined effect of the geometrical acceptance (aperture) and trigger efficiency. The acceptance function, $A(t) = 4t^2/(1+4t^2)$, approximately describes the net acceptance and is used in the generation of Monte-Carlo events in the analysis described in Chapter 6. This function is multiplied by $e^{-t/\tau}$ and shown superimposed on the data in Fig. 7. In chapter 6, simultaneous fits to the data shown in Fig. 7 and to the subset which is flavor tagged (see Chapter 5) are performed to obtain the B_s mean life, $x = \Delta M/\Gamma$ and the dilution factor, K.

The experimental resolution in the measured proper time is obtained by comparing the generated B_s flight path with its reconstructed value (see Chapter 7 in P238) for a large number of Monte-Carlo events. This difference quantity is plotted in Fig. 8 and is seen to have a standard deviation, $\sigma_z = 180$ μm. This is an improved version of Fig. 33 on page 54 of P238.

The error in proper time, σ_t, is obtained from the relation $z = ctp/m$ and $\sigma_z = 180$ μm. With a mean $p = 35$ GeV/c, we find $\sigma_t = 6.7$ %. For a number of reasons, the expected value will be somewhat smaller than this. Firstly, the data in Fig. 8 are calculated using a distance of 5 cm between sili-

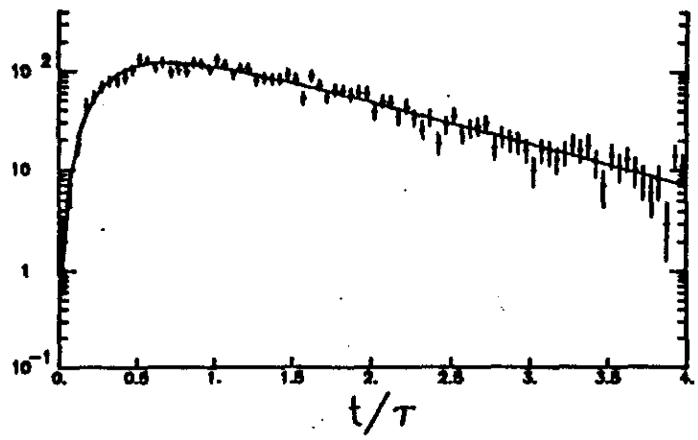

Figure 7: Simulated proper time distribution (in units of B mean life) for 9000 reconstructed B_s events. The departure from a pure exponential illustrates the acceptance effects of geometry, trigger and event reconstruction. The superimposed curve is the empirical acceptance function $A(t) = 4t^2/(1+4t^2)$ multiplied by $e^{-t/\tau}$ This curve is a reasonably good fit to the B events which have been accepted by our trigger simulation and reconstruction programs.

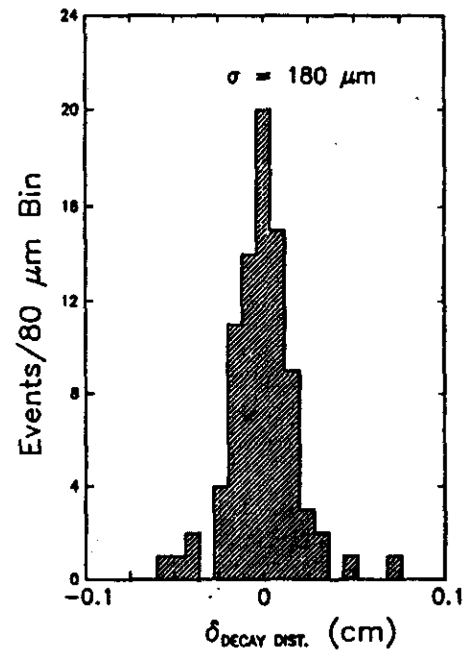

Figure 8: Difference between Monte-Carlo generated and reconstructed B track length. The width of this distribution (standard deviation, σ_Z = 180 μm) gives the uncertainty in our measurement of the B track length. As discussed in the text, several improvements in software and hardware will result in σ_Z actually being smaller than this value.

con detector planes used in the P238 silicon configuration. We have since decided to decrease this distance to 4 cm (see Appendix B in this document). Secondly, the algorithm used in the calculation of the data in Fig. 8 can be further improved.

6. SIMULATION AND ANALYSIS OF B_s MIXING

As discussed in the previous chapters, we expect a total sample of at least 9000 fully reconstructed B_s and $\bar{B}_s$ mesons with measured proper decay time, per 10 $pbarn^{-1}$ integrated luminosity if both outgoing arms are instrumented with spectrometers and $0.5\%/\sqrt{E}$ electromagnetic calorimetry is used. This minimum number assumes that only the decay modes listed in Table 2 are reconstructed. The observation of additional decay modes obviously increases the event yield. According to the tagging discussion in Chapter 4, 58% of these events, or about 5000, will be tagged with charged K-mesons.

Six different observable proper time distributions can be formed using these events, as shown in Table 6. The expected numbers of events of each type are also shown, as well as the mathematical function which is to be fit to each.

Table 6: Types of Proper Time Distributions & Sample Sizes[a,b,c]

Type	No. Events	Nature of Proper Time Distribution
B_s untagged	1980	$A(t) \cdot e^{-t/\tau}$
$\bar{B}_s$ untagged	1980	$A(t) \cdot e^{-t/\tau}$
B_s tagged with K^+	1260	$A(t) \cdot e^{-t/\tau} \cdot [1 - K\cos(xt/\tau)]$
$\bar{B}_s$ tagged with K^+	1260	$A(t) \cdot e^{-t/\tau} \cdot [1 + K\cos(xt/\tau)]$
B_s tagged with K^-	1260	$A(t) \cdot e^{-t/\tau} \cdot [1 + K\cos(xt/\tau)]$
$\bar{B}_s$ tagged with K^-	1260	$A(t) \cdot e^{-t/\tau} \cdot [1 - K\cos(xt/\tau)]$

(a) The total number of events in this table, 9000, corresponds to an integrated luminosity of 10 $pbarn^{-1}$ and two instrumented arms, as discussed in Chapter 3. The tagging fractions are discussed in Chapter 4. The equations are derived in Chapter 2.
(b) The sign of the K tag shown in each case assumes it is a secondary K, as explained in Chapter 4. If it is a primary K, its sign must be opposite to correspond to the function shown.
(c) For the tagged distributions, the actual numbers of events will be somewhat different when x is small since the integrals of the two types of functions are not equal.

In these formulae the mixing parameter, $x = \Delta M/\Gamma$ and τ is the B_s lifetime. Thus, the proper time, t, appears in units of this lifetime. K is the "dilution" factor, explained in Chapter 2, which results from all types of "mis-tagging". A(t) is the acceptance factor which depends on trigger efficiency and event reconstruction efficiency, as discussed in the last chapter.

In order to demonstrate the expected statistical significance in the determination of x, τ and K with samples of this size, and also to show how the significance depends on sample size and background, we have generated Monte-Carlo data samples and subjected them to joint maximum likelihood fits with x, τ and K as free parameters. In the generation, the acceptance function is taken to be $A(t) = 4t^2/(1+4t^2)$. As explained in Chapter 4, this curve describes the simulated data sufficiently well for our present purposes.

A Monte-Carlo data sample of 9000 events was generated according to the equations listed in Table 6 for each of the x values, 0.7, 5, 10 and 15. The value of K used in the generation was fixed at 0.34, which is approximately the product of the dilution factors discussed in chapters 2 and 4, but also includes a factor of 0.95 for Cerenkov misidentification and takes into account the fact mentioned in Chapter 4 that oscillation of the tagging particle is not a relevant concern for K_p tags.

A simultaneous maximum likelihood fit was then made to the entire data sample using, for each event, the relevant equation. For example, the likelihood function for a B_s tagged with a "secondary" K^+ is:

$$\mathscr{L} = \frac{A(t) \cdot e^{-t/\tau} \cdot [1 - K\cos(xt/\tau)]}{\int A(t) \cdot e^{-t/\tau} \cdot [1 - K\cos(xt/\tau)]\, dt}$$

The sum of $-\log \mathscr{L}$ for all events is minimized using the program MINUIT. The results are shown in Figs. 9 for all four values of x and the fitted parameters K and x are given in Table 7.

A measure of the uniqueness of the maxima found in the likelihood function is given by plotting, for each case, the value of that function vs. x, with fixed τ and K. τ can be obtained independently from the time distribution of the entire sample and the value of K is known reasonably well from physics arguments and observed background. Such plots are shown in Fig. 10.

The fits shown in Fig. 9 and Table 7 are excellent. The fluctuations in the likelihood function vs. x seen in Fig. 10 are a very small fraction of the convergence peaks. We can thus conclude that, if our estimates are correct, a successful experiment could be performed with far fewer events and/or more background.

Thus, we now investigate the dependence of the quality of the results on sample size and background. This will allow us to finally decide on (a) whether to instrument only one arm or both arms; (b) whether to construct a Lead-Glass calorimeter or a Liquid-Xenon calorimeter.

The parameters which best indicate the sample size required for a good measurement of B_s mixing are the error in the mixing parameter (σ_x) and the significance of the oscillation amplitude (N_σ = K divided by the error in K). We plot these two quantities as a function of the number of signal events in Fig. 11 for a fixed K value of 0.34 and an x value of 15. It can be seen from this figure that at the expected yield of 3000 events for a Lead-Glass calorimeter and one instrumented arm, we expect a highly significant measurement (9 standard deviations in the oscillation amplitude) and an error of less than ± 0.1 on the measurement of x.

This is further illustrated in Fig. 12 which show the results of likelihood fits performed on a sample size of 3000 simulated events for the same x values used in Fig. 9. In the simulation of this 3000 event sample, we have also taken into account the expected signal/background ratio (about 4 for the Lead-Glass calorimeter) illustrated in Fig. 4 of section 3.2. Since the background is mainly associated with B events, we assume that it will have an exponential proper time dependence with the same lifetime as the signal. With this assumption, the only effect of the background is to dilute the oscillation amplitude and thus reduce K. Even with this additional dilution, the significance of the measurement is still good and the error on x is everywhere less than ± 0.1.

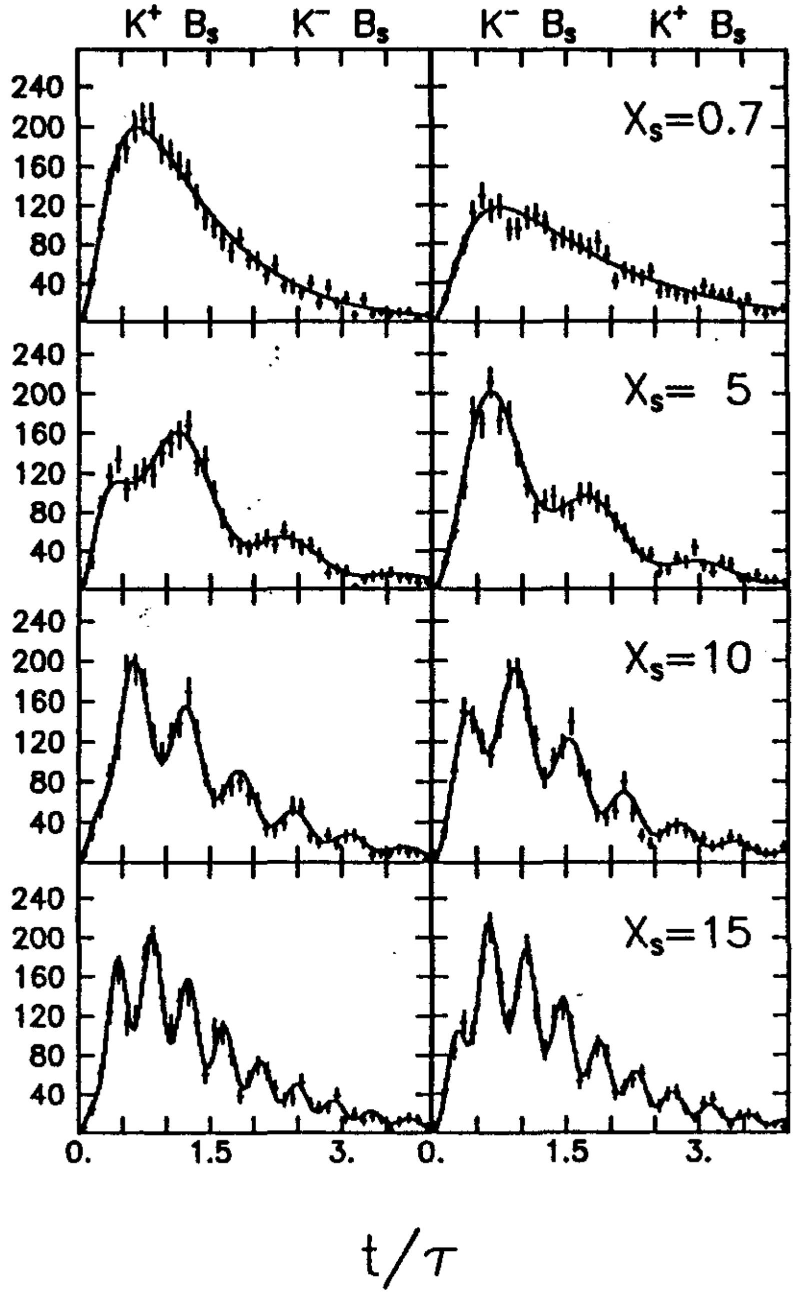

Figure 9: Proper time distributions for the two types of tagged events shown in Table 6 (a,b) x = 0.7, (c,d) x = 5, (e,f) x = 10, (g,h) x = 15. The Monte-Carlo data points correspond to a total sample of 9000 events as discussed in the text. The curves result from simultaneous maximum likelihood fits to the data shown and the proper time distribution of the entire 9000 event sample.

Table 7: Parameters Obtained From Fits(a) Shown In Fig. 9

Input x Value	Fitted K	Fitted x
0.7	0.27 ± 0.03	0.70 ± 0.05
5.0	0.30 ± 0.02	4.99 ± 0.03
10.0	0.32 ± 0.02	9.96 ± 0.03
15.0	0.33 ± 0.02	14.93 ± 0.03

(a) For a 9000 event sample

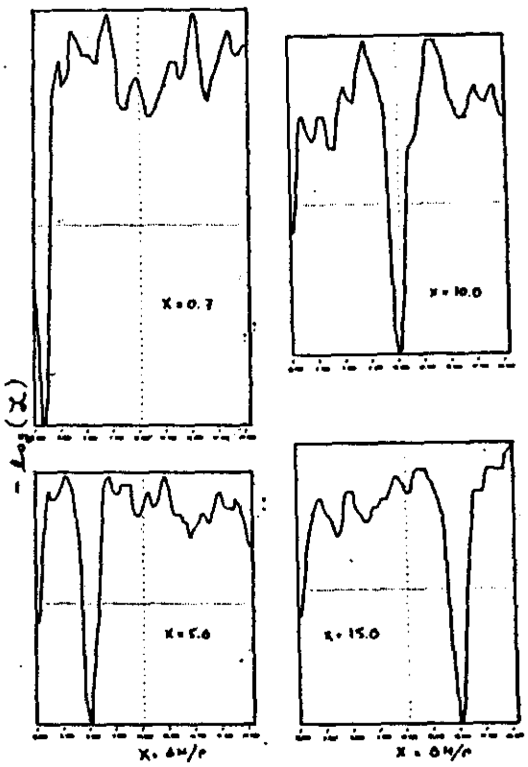

Figure 10: The log-likelihood function plotted vs. the mixing parameter, x for four data samples generated with x = 0.7(a), 5(b), 10(c), 15(d). The values of τ and K are fixed to their generated values.

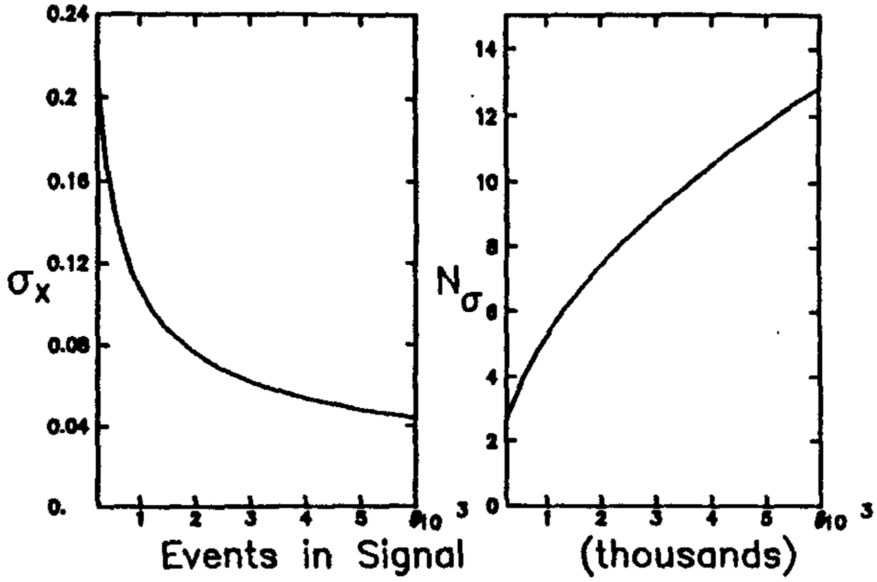

Figure 11: (a) Error on the mixing parameter (σ_x) vs. the number of B_s signal events. (b) The significance (in standard deviations) of the oscillation amplitude (K) vs. the number of B_s signal events.

The 3000 event sample obtained when we assume one instrumented arm and a Lead-Glass calorimeter, is seen to yield an acceptably precise and significant measurement of the mixing parameter x. We next try to find the minimum event sample size which will allow an adequate measurement of the mixing parameter. Refering again to Fig. 11, we see that a sample size of as few as 500 events will give a 4σ measurement and an error on x of about 14%. We investigated the uniqueness of the solution by studying (as in Fig. 10) the log-likelihood function vs. x for several randomly generated samples for each type of sample size. In Fig. 13(b), we show a typical example of the resulting curves. In Fig. 13(a) a typical (bad) example of the result for a 250 event sample shows that it is not possible to obtain reliable results with such a small sample. For comparison, Figs. 13(b,c,d) show typical log-likelihood functions plotted vs. x for sample sizes of 500, 1000 and 3000 events, respectively. We conclude that a sample size of 500 events is the smallest sample size from which a meaningful result could be obtained. Thus, our prediction of 3000 events implies a safety margin of about a factor of six.

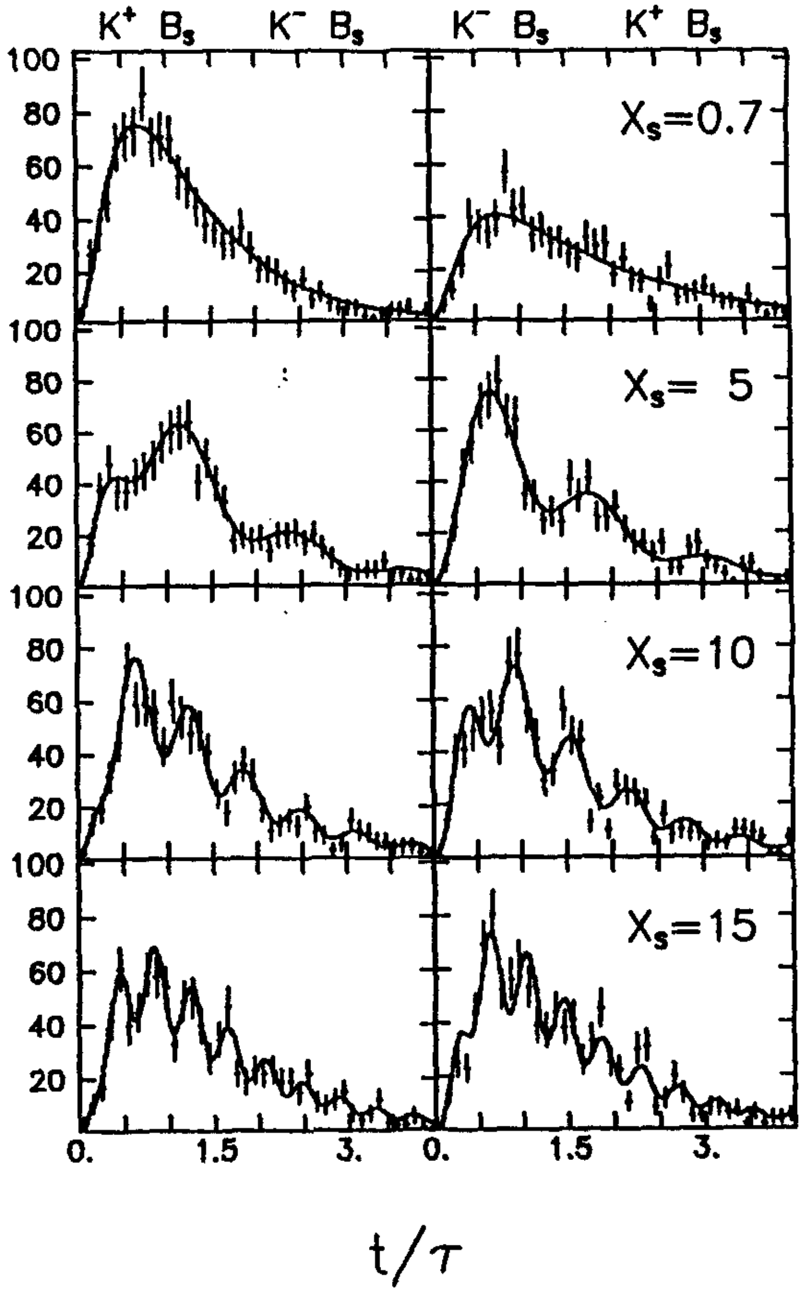

Figure 12: Proper time distributions for the two types of tagged events shown in Table 6 (a,b) x = 0.7, (c,d) x = 5, (e,f) x = 10, (g,h) x = 15. The Monte-Carlo data points correspond to a total sample of 3000 events as discussed in the text. The curves result from simultaneous maximum likelihood fits to the data shown and the proper time distribution of the entire 3000 event sample.

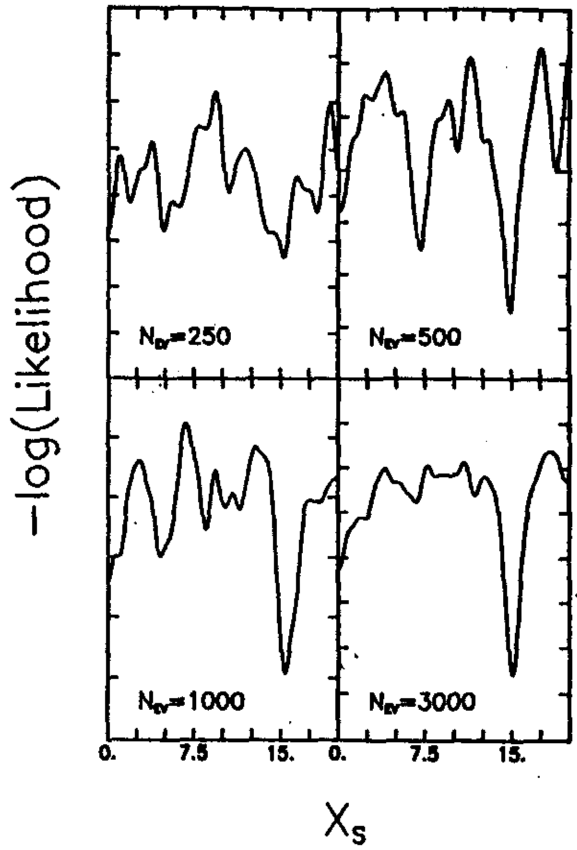

Figure 13: − Log-Likelihood Function vs. x: The data samples of 250, 500, 1000 and 3000 events were all generated with x = 15. In each case, the distributions are typical examples from a study of 20 Monte-Carlo experiments.

7. OVERVIEW OF OTHER EXPERIMENTS

We have been asked to compare this experiment with other experiments which will take data in the next few years, with regards to the feasibility of measuring the B_s mixing parameter. This is a hard task since, to our knowledge, no detailed analysis of the type presented in this addendum to P238 exists for the other experiments. Some work along these lines has been done to evaluate the impact of new or upgraded machines (see for example Roudeau [Selected topics in B physics at LEP, LAL 89−21] on B_s mixing at the luminosity-upgraded LEP).

We limit ourselves, therefore, to give a table of indicators (Table 9) which is meant to provide a qualitative understanding of the relative merits of different experiments.

The choice of indicators is based on the fact that the determination of x_s requires a precise measurement of the time distribution of B_s and $\bar{B}_s$ (where the particle / antiparticle identity is defined at $t = 0$). The figures of merit are:

1. The expected number of tagged B_s ($\bar{B}_s$) mesons selected by the trigger which have all the decay products within the detector acceptance.

2. The capability of fully reconstructing B_s final states, a characteristic that depends crucially on the quality of particle identification, especially π-K separation.

3. The precision of the reconstruction of the vertex coordinate. Vertex measurement is essential both as a tool for identifying secondary vertices, and to measure the time distribution accurately.

We have chosen four experiments to represent general classes of experiments (e^+e^- low energy collider, fixed target, etc.). In our opinion the chosen experiments have the highest sensitivity to B_s of experiments in their respective classes. We do not consider experiments to be done at machines that either are in the design stage (PSI, SSC, etc.) or require major upgrades (High Intensity LEP, Fermilab Tevatron with a new main injector) since they will take place, we trust, on a different time scale.

The estimates for the number of events from the different experiments is straightforward. The number of B_s + $\bar{B}_s$ is equal to

$$2 \cdot \int \mathcal{L}\, dt \cdot \sigma_{b\bar{b}} \cdot F_s \cdot A$$

where F_s is the number of B_s (or $\bar{B}_s$) per $b\bar{b}$ event, and A is the fraction of B_s or $\bar{B}_s$ events with the decay products in the spectrometer. We have used the input values described in Table 8. Where detailed information is not available, a reasonable upper limit is used.

Table 8: Estimates of event samples

Experiment	CLEO (Υ5S) (CESR)	DELPHI (LEP)	E771 (FNAL)	CDF (FNAL)	P238
Integrated $\mathcal{L}$	10^3 pb^{-1}	150 pb^{-1}	250 pb^{-1}	10 pb^{-1}	10 pb^{-1}
σ_{bb}	0.27 nb	6.5 nb	20 nb	45 μb	10 μb
B_s Fraction (F_s)	1.0	0.2	0.2	0.2	0.2
Acceptance (A)	1.0	1.0	1.0	1.0	0.295
Number[1] of B_s in Detector	5.4×10^5	3.9×10^5	2×10^6	1.8×10^8	1.2×10^7

[1] Per run of 10^7 sec. of data taking

We repeat the last row of Table 8 (the estimate of the number of B_s events in each detector) at the top of Table 9. The second row of this table gives the expected yield after triggering. For the trigger efficiency we have taken arbitrarily $\epsilon_t = 0.8$ for DELPHI and CLEO. For E771, the trigger requires two muons in the final state, and should detect events with one $J/\psi \to \mu^+\mu^-$, or events in which both B's decay semileptonically. The geometric acceptance for the two muons is 0.25. We then take:

$$\epsilon_t = 0.25\cdot[BR(B\to\mu)^2 + BR(B_s\to J/\psi)\cdot BR(J/\psi\to\mu\mu)] = 0.25\cdot[.124^2 + 5\times 10^{-3}] = 5\times 10^{-3}.$$

For CDF the trigger requires one muon with high p_t so the trigger acceptance is $\epsilon_t = 0.124 \cdot \epsilon_{ptcut}$. Because the minimum p_t is unknown, we leave $\epsilon_{ptcut} = 1$.

The numbers in parentheses in the last line of the table are obtained by multiplying the number of events collected by the trigger by the reconstruction factor obtained for our experiment ($9000/5\times 10^6 = 1.8\times 10^{-3}$). In the case of LEP, this estimate agrees well with the number obtained by scaling down Roudeau's estimate to the nominal LEP luminosity.

Table 9: Comparison of Existing Experiments with P238

	Low Energy e^+e^- Colliders	High Energy e^+e^- Colliders	Fixed Target	$\bar{p}-p$ Colliders	This Experiment
Experiment	CLEO (Υ5S) (CESR)	DELPHI (LEP)	E771 (FNAL)	CDF (FNAL)	
Number[1] of B_s in Detector	5.4×10^5	3.9×10^5	2×10^6	1.8×10^8	1.2×10^7
$B_s + \bar{B}_s$ Selected by Trigger	4.3×10^5	3.1×10^5	10^4	2.2×10^7	5×10^6
σ_L/L	>.50	.11	.05	.04	<.06
Particle ID	Partial	Yes	Yes?	No	Yes
Event Sample	?	245(558)	(18)	?	9×10^3

[1] Per run of 10^7 sec. of data taking

We conclude that:

1. CLEO is not competitive in this measurement because the decay path is measured very poorly and the sample size is low.

2. CDF is the only experiment which starts out with large statistics, but reconstruction and positive identification of the B_s will be made very difficult by the lack of good quality particle identification.

3. E771 does not have sufficient statistical power.

4. DELPHI is the experiment which comes closest to performing an x_s measurement, but it is still too weak from the statistical point of view. In fact, Roudeau estimates that one needs thirty times the statistics of a typical run to measure this effect.

APPENDIX A: Comments on Data-Driven Processor

As reported in our memo to the committee (SPSC/M 443) of 16 May, 1989, we have decided to use the existing Nevis/University of Massachusetts processor design to implement the trigger algorithm described in the P238 proposal.

We have discussed the P238 algorithm at some length with Bruce Knapp and have realized that the problems we face are simpler than those already solved by the Nevis group for their trigger in Fermilab Experiment E690. There are several reasons for this:

- We look only for straight lines in 3 planes, while they are reconstructing 5 point tracks in an inhomogeneous magnetic field.
- Our algorithm does not call for matching tracks between views. Theirs does.
- We do not require track fitting for parameter estimation. They do.
- Unlike E690, we are not attempting full efficiency for track finding (we would in fact rather lose the low momentum tracks since they have poor impact parameter resolution).
- Since our detector is divided into four independent quadrants and since, at the collider, the tracks are not folded into the forward direction by a Lorentz boost, we have a substantially smaller track density and thus a smaller number of hit combinations to sort through (despite the increased track multiplicity at the collider).

Although they do not try to find an event vertex using all the found tracks in an event, it appears we can adapt and extend techniques they use for track fitting to the vertex finding problem with rather little difficulty.

Fig. 14 is a preliminary block diagram of a processor suitable for the P238 algorithm as described in Section 4.3 of the P238 proposal. We divide the processor into 5 subroutines, which are isolated from each other by control buffers. The 3-plane line finder contains most of the hardware, approximately 160 existing Nevis modules divided into eight identical sections (4 quadrants $\times$ 2 views) and is essentially a copy of a basic line-finding subroutine designed by Bruce Knapp et al.

The Nevis processor modules are themselves quite simple. Each module takes one or two 24 bit (16 data + 8 control) input data words, performs some simple operation on them and produces an output which is passed on to the next module. All modules in the system are clocked synchronously and the input and output data words are latched into registers on each clock cycle. Care has also been taken to allow access to all of the input and output registers in the system, either for reading data or inserting data. This greatly simplifies the task of debugging and diagnosing problems since the state of the system can be determined and checked on a cycle by cycle basis.

The rest of the subroutines for the P238 algorithm have not yet been mapped out in complete detail but preliminary design work indicates that we will need fewer than 100 modules for the rest of the system (for a total of about 260 modules compared to about 700 modules for the E690 processor). We will need to design one module for the Histogrammer subroutine but can probably use existing Nevis modules otherwise (although perhaps some minor modifications may be necessary). Detailed design of the system awaits the completion of the software emulator package (described below).

The processor emulator is a software package designed to simulate the action of the processor on a cycle by cycle basis. Each processor board type (of which there are 47) is simulated by a separate subroutine. The simulation extends not only to the processing of event data but also communication with the processor control structure. The emulator can thus mimic such actions as the loading of tables, the processing of real data, or loading and reading test data words into any register in the system.

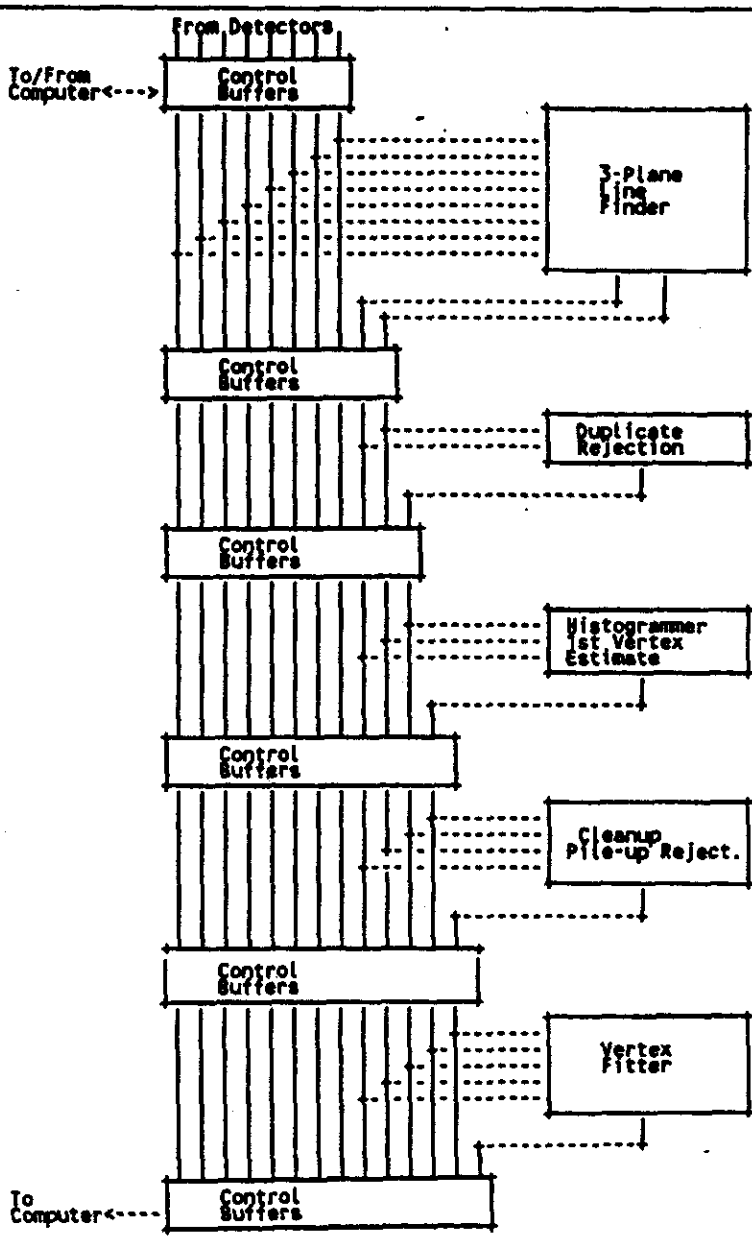

Figure 14: Preliminary block diagram of P238 processor

A processor algorithm consists of a list of boards, the specification of the contents of any memory elements on those boards and the specification of how these boards are to be cabled together. Such a list is known as a configuration file. The emulator reads this file in its initialization phase and thus determines which board subroutines must be called. It calls these subroutines which in turn reserve enough memory to hold any tables which must be downloaded as well as memory locations for the input and output registers. Storage is also reserved to hold cable contents and pointers are set up to the memory locations which hold the contents of the input and output cables. After this initialization phase, the memory locations reserved to hold on-board tables are loaded by simulating the cycles that would be executed by the processor hardware in performing this function.

At this point, the emulator is ready to process data. Data is put into the locations reserved for input cables and the board subroutines are called for each board listed in the configuration file. Each board subroutine checks for data on the input cables, and if present performs its operation and modifies the memory locations reserved for its on-board registers as well as that reserved for its output (and possibly input) cable. This procedure completely emulates the processing performed in one clock cycle. It can then be repeated any number of times to simulate subsequent cycles. If the process is repeated a sufficient number of times, the data will eventually propagate through the entire "processor" (assuming it is correctly designed) and start appearing in the locations reserved for the output control buffers, together with the processed data.

Using the emulator, it will be possible to precisely predict the operation of a given algorithm on any set of simulated event data. For example, the average number of clock cycles per event can be easily determined and problems of precision can be investigated.

The emulator will be usable not only for the design and evaluation of processor configurations but also for diagnostics since the same data can be given to both the emulator and the real processor and the results of the computation compared. The operation of a single board can thus be evaluated as can the operation of an entire subroutine.

We are currently collaborating with E. Hartouni of the University of Massachusetts, Amherst to write this emulation package. Two of us (M. Medinnis and R. Dzhelyadin) are actively writing new modules and debugging existing ones. We are also training a student (D. Lynn)) and plan that before the end of August, to have a team of 4 nearly full-time people (also including J. Zweizig) working on software development at CERN, in addition to E. Hartouni.

Currently, a total of 10 of the required 47 software modules either exist or are under development. We plan to finish writing the code by the end of September or early October. Soon thereafter, some of us will go to Fermilab to work with the E690 collaboration on the installation and debugging of their processor.

Replication of the modules necessary for construction of the processor should be completed by early January 1990. The Nevis / University of Massechusetts collaboration (E690) has agreed to lend us the rack and crates necessary to house a processor of the size we envision.

APPENDIX B: New Silicon Micro-Vertex Detector Configuration

In our simulation work (including that presented in this addendum), we assume a vertex detector consisting of 11 parallel planes, spaced 6 cm apart, with each plane divided into four 7×7 cm^2 silicon squares (see section 4.1 of the P238 proposal). The silicon planes are assumed to be 200 μm thick and to have 25 μm strips on both sides.

After discussions with manufacturers, we have come to realize that such a scheme is not feasible primarily because the 7×7 cm^2 size is too large to comfortably fit on the standard 4 inch diameter silicon wafers. We have thus revised our detector design. We are now considering a detector which consists of sixteen parallel 10×10 cm^2 detector planes divided into four 5×5 cm^2 squares, spaced 4 cm apart. The detector is otherwise the same as that presented in the proposal.

This new configuration results in somewhat improved impact parameter resolution for low momentum tracks which will in turn result in a somewhat improved minimum bias rejection. (We have not estimated the improvement but we do not expect a dramatic effect.) Another advantage of the new design is that it extends the coverage of the interaction region from ± 18 cm to ± 22 cm, thus increasing the fraction of usable events from 81% to 94%. The disadvantage of the new scheme is that the amount of material in the detector increases by 45%. The resulting increase in multiple scattering will not cause problems for the trigger algorithm since only the two planes closest to the vertex are used to estimate track parameters. The effect of increased photon conversions, delta ray production and nuclear interactions has not been simulated, but we do not expect the trigger suppression estimates to change significantly since these processes had but small effect on the original estimates.

APPENDIX D

APPENDIX 2

EUROPEAN ORGANIZATION FOR NUCLEAR RESEARCH

CERN-SPSC/89-55
SPSC/P238Add.2
14 September, 1989

Addendum to Proposal P238:

REQUEST FOR COLLIDER TEST OF SILICON MICROVERTEX DETECTOR

A. Brandt, S. Erhan, D. Lynn, M. Medinnis, P. Schlein*, J. Zweizig
University of California, Los Angeles, U.S.A.

P. Weilhammer[1]
CERN, Geneva, Switzerland

T. Ypsilantis
College de France[2], Paris, France

G. Borreani
University of Ferrara and INFN[3], Italy

A. Kaschuk, V. Samsonov, V. Sarantzev, E. Spiridenkov, A. Vorobyov
Institute for Nuclear Physics, Gatchina, Leningrad, U.S.S.R.

M. Calvetti
University of Perugia and INFN[3], Italy

J.B. Cheze, J. Zsembery
Centre d'Etudes Nucleaires – Saclay[4], Gif-sur-Yvette, France

R. Dzhelyadin, Y. Guz, V. Kubic, V. Obraztsov, A. Ostankov
IHEP-Serpukhov, Protvino, U.S.S.R.

C. Biino, R. Cester, A. Migliori, R. Mussa, S. Palestini
University of Torino and INFN[3], Italy

ABSTRACT

We request a collider run during the fall of 1990, in order to test the silicon micro-vertex detector proposed in P238. To be certain that the proposed trigger will function correctly, we should verify that real data, taken in situ under the same conditions of the experiment (including present low-β machine configuration), are in essential agreement with the Monte Carlo simulation data used in the trigger design of P238. Revised (conservative) event yield estimates and a first analysis of simulated RICH counter data for B_s are also given.

---

*) Spokesman
[1]) At this time, commitment is for silicon test run
[2]) Pending approval of the Laboratory and IN2P3
[3]) Pending approval of INFN
[4]) Pending approval of CEN-Saclay

TABLE OF CONTENTS

APPENDICES

1. Introduction

In the documents, P238 and P238Add.1, we have proposed a new approach to the study of B (beauty or bottom) physics at hadron colliders. Forward detectors installed on the outgoing arms of an interaction region provide adequate acceptance of the forward-collimated decay products of B-mesons. The reconstruction of exclusive final states in B-decay with minimal background is made possible with the use of a silicon microvertex detector, whose elements are installed perpendicular to the beam, inside the vacuum pipe and dispersed throughout ±30 cm of the interaction region. Data acquisition is triggered by the results of high speed digital calculations based on the silicon data and performed with the use of a data-driven processor.

The efficient triggering of heavy flavor in hadron machines was long thought to be "next to impossible". However, the success of Fermilab Experiment E691 and its successor in obtaining large clean samples of charmed particles has partly dispelled this "myth". Now, with the several physicist-years of Monte Carlo simulation work reported in P238, we have demonstrated that it should be possible to advance one step further by triggering on and obtaining, at the much higher energy hadron colliders, relatively clean and large samples of beauty mesons.

While there are many challenging hardware components in the proposed Forward Beauty Detector (FBD), only the operation of the silicon detectors within the SPS vacuum chamber has intrinsic uncertainties which could influence the overall success of the experiment. These major uncertainties are the amounts of event-unrelated noise and beam halo tracks which will be recorded by the silicon detectors. Since we have shown, in Appendix A of P238, that the PYTHIA-generated minimum bias events are in good agreement with the minimum bias data from Experiment UA5, it is likely that only such (unanticipated) event-unrelated "noise" in the silicon could, a priori, present serious difficulties.

In order to determine the magnitude of such contributions to the observed silicon signals, and thus the reliability of the proposed trigger in the complete experiment, it is essential to have a preliminary run at the collider with elements of the silicon microvertex detector installed in the manner proposed in P238, and with the same low-β machine configuration that will be required by the full experiment (straight section ±13 meters). If the silicon data thus obtained is similar to our Monte Carlo simulated silicon data, the proposed trigger will work as required.

2. Goals of Collider Test Run

The collider test will be carried out with the following goals in mind:

- Write events on tape, using a minimum bias trigger (beam crossing signal in coincidence with signals from a modest scintillator hodoscope), to verify and tune (offline) both our Monte Carlo simulation and the trigger described in proposal P238. This will also allow an evaluation of the effects of background sources such as beam halo, which are not included in the simulation. With this data we will be able to improve the present trigger algorithm and evaluate (and invent) other, possibly more effective, trigger algorithms.

- It should be possible to clearly demonstrate evidence for events which contain B hadrons by track reconstruction (straight lines) in events with multiple high multiplicity secondary vertices. We estimate that 10^7 events on tape will yield approximately 100 events with visible B hadrons. Detailed estimates are being made of the fraction of these which will be distinguishable from the more abundant charmed particle events.

- Measure radiation doses to detector and readout electronics. For a number of reasons, we are reasonably confident that radiation is not a problem: (a) our silicon detectors will be retracted about 10 cm from the beam line when the machine is not in "stable beam" state; (b) from measurements made by UA8, the halo rate under normal operating conditions is rather small;

(c) the beam-beam interaction rate is not high enough to cause difficulties. We will nonetheless take this opportunity to install dosimeters at various places within the detector volume.

- Test the precision and reproducibility of the detector positioning mechanism using reconstructed tracks in the silicon. Although such tests could be done in a fixed target test beam, the completed silicon mechanics system (see Section 4 below) is not likely to be available before the end of the fixed target run in June, 1990.

Finally, we note that, in Appendix A of P238Add.1, we described the current status of the data-driven processor. Development of the software package which will allow emulation of the full trigger processor is in progress with very high priority and production (replication) of the hardware modules should be completed early in 1990. Although the online use of the processor does not constitute an uncertainty in the same class as those mentioned above, it will nonetheless be possible to have a smaller version of the full processor running on-line by the time of the collider run (about 30 modules out of the full set of about 260 modules). This test processor configuration would include one of the eight 3-point line-finding subroutines of the final processor configuration, a duplicate rejection subroutine and a first vertex estimator and would be capable of online reconstruction of the tracks and calculation of the vertex position (using the first-vertex estimate described in Section 4.3 of P238).

3. Silicon Detectors

The following two paragraphs are from Appendix B of P238Add.1.

> In our simulation work (including that presented in this addendum), we assume a vertex detector consisting of 11 parallel planes, spaced 6 cm apart, with each plane divided into four $7 \times 7\ cm^2$ silicon squares (see section 4.1 of the P238 proposal). The silicon planes are assumed to be 200 μm thick and to have 25 μm strips on both sides.
>
> After discussions with manufacturers, we have come to realize that such a scheme is not feasible, primarily because the $7 \times 7\ cm^2$ size is too large to comfortably fit on the standard 4 inch diameter silicon wafers. We have thus revised our detector design. We are now considering a detector which consists of sixteen parallel $10 \times 10\ cm^2$ detector planes divided into four $5 \times 5\ cm^2$ squares, spaced 4 cm apart. The detector is otherwise the same as that presented in the proposal.

In order to keep the detector for the test run as simple as possible, consistent with attaining the goals listed in Section 2, a subset of the full 16-plane detector system will be used. Fig. 1 shows the 6-plane system which will be constructed. The planes are perpendicular to the beam line and are spaced every 4 cm. Each detector consists of independent upper and lower assemblies, each of which comprises two 5 cm x 5 cm detectors side by side. The detectors will only have vertical microstrips. We can thus save considerable money and effort while still meeting the goals of the proposed test.

With the 6-plane geometry of the test detector, about one third of all events will occur in a roughly 8 cm long region, which will allow reconstruction of tracks with at least three hits in one hemisphere and tracks with two hits in the opposite hemisphere.

Since the version of the Berkeley SVX chip intended for use in the final experiment will not be available until 1991, we will use the current SVX chip (Version D). This chip is a production version and is now being installed on the CDF microvertex detector. For the test run, we will read out the charge associated with all hit strips.

Because Version D of the SVX chip is designed to couple to 50 μ pitch silicon detectors, the detectors used in the test run will have 50 micron pitch instead of the 25 micron pitch of the detectors in the final experiment. Since the configuration to be used in the test will only measure coordinates in the horizontal view, there will be a total of about 24,000 channels.

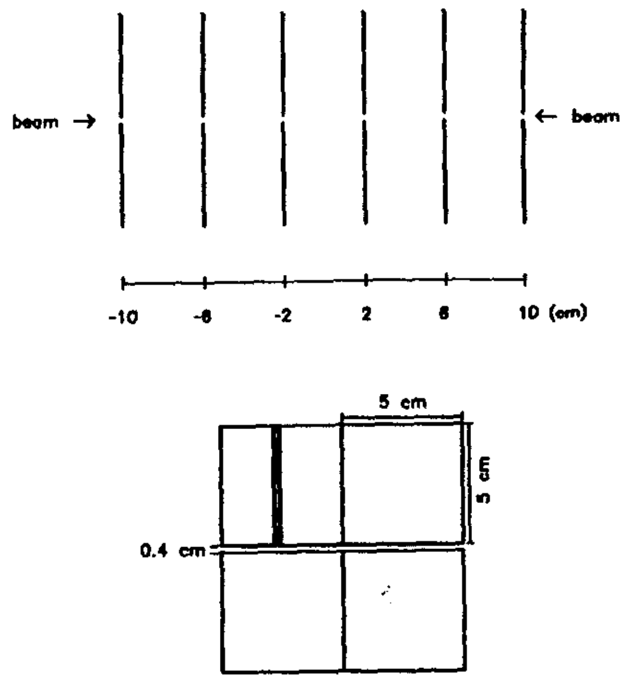

Figure 1: Proposed 6-plane silicon detector system for collider test run. Side view shows the 4 cm spacing between planes. and the independent upper and lower detector assemblies. The beams pass through the 4 mm gap between these assemblies. The front view shows how the upper and lower assemblies each contain two 5 cm x 5 cm silicon detectors side by side.

4. Support Mechanics & RF Shielding

The essential requirements for the silicon support mechanics are discussed on pages 16-18 of P238. These have been discussed with members of the SPS vacuum group and various ideas on how to achieve them have evolved. In particular, Hartmuth Wahl of that group has suggested a scheme, whereby the silicon detectors are isolated from the main machine vacuum by a window which would also provide sufficient shielding against RF pickup by the silicon detectors due to the passing beam bunches.

It has been suggested to us that the Vacuum Group might be able to assist us in some preliminary tests of the RF pickup problem by constructing a model chamber in which one of our presently running silicon detectors is positioned close to a long wire, through which a current pulse is passed to simulate the passage of a beam bunch. Such a test would give us a first estimate of the amount of shielding necessary in the construction of the full mechanical system.

It is our understanding that Hartmuth Wahl has communicated to Pierre Darriulat his assessment that the complete silicon mechanics system could be designed and constructed to be ready for a fall 1990 run in the collider. From our side, we would have the necessary detectors tested and ready for installation on the mechanics system several months before the run.

5. Preparation Timetable for Collider Test Run

Due to the effort made in preparing silicon detectors for a test run in one of the UA8 Roman pot spectrometers during the 1989 run of the SPS-Collider, we already have all necessary SVX-chip readout electronics and relevant software fully operational and interfaced to an online MicroVax computer. We plan to install this equipment as a silicon test setup in a fixed target test beam during the next few weeks. With this test setup, we will test and compare silicon detectors from three sources, The Central Institute for Industrial Research[1] (Oslo), Hamamatsu and Micron.

We already have Hamamatsu and Micron detectors with SVX readout chips bonded to them. They are thus ready to be installed in a test beam. We can bond an existing SVX chip to one of the Oslo detectors in a short time and thus be ready to compare the readout of all three detector types with that chip.

We should have all tests completed by the end of this year, in time to have completed production runs of the necessary detectors and SVX chips on the necessary time scale. We will be ready for the mechanical interface of the detectors with the mechanical support structures provided by the SPS Division, in time for a fall 1990 Collider run.

6. Timetable for Complete Experiment

If design work of the other detector components (magnets, chambers, lead-glass calorimeter and RICH detectors) is carried out in parallel with preparations for this proposed silicon test, it should be possible to go into full production before the end of 1990. With some considerable effort (and help from CERN), it may be possible to have a completed detector ready for use before the end of 1992.

---

[1] The Oslo source manufactures capacitively-coupled strip detectors with integrated polysilicon bias resistors, which were pioneered by P. Weilhammer and T.E. Hansen [see: M. Caccia et al., NIM A260 (87)124]. The advantage of this approach over other detectors now in use is the elimination of d.c. offsets which can be caused by channel-dependent leakage currents. Such detectors have been developed for use in the DELPHI microvertex detector and are found to give reproducible results within very tight specifications. The possibility of also conveniently reading out the n-side (back-side readout) is a very promising aspect which could be very useful for us in the construction of the final complete silicon trigger detector.

APPENDIX A: REVIEW OF EVENT YIELD ESTIMATES IN P238Add.1

We have reviewed our estimates of B_s and $\bar{B}_s$ event yields in P238Add.1 and adjusted several of the assumed efficiencies and branching ratios in an attempt to provide a more conservative view of the situation. Table 1 is a revised version of Table 2 in P238Add.1 and contains the new estimates. With two arms instrumented and Lead-Glass electromagnetic calorimetry, 1900 reconstructed B_s-mesons should result per 10 $pbarn^{-1}$ integrated luminosity (with Liquid-Xenon calorimetry, 2800 events result). Thus, with one arm instrumented and Lead-Glass calorimetry, approximately 1000 events could be obtained per 10 $pbarn^{-1}$. This should be sufficient for an excellent measurement of $\Delta M/\Gamma$, although the additional factor of two statistics available with a second instrumented arm would be comforting.

Table 1: Revised B_s & $\bar{B}_s$ Event Yields

$1.5 \cdot 10^8$ $b\bar{b}$ Produced for $\int \mathcal{L} dt = 10$ $pbarn^{-1}$

1.8×10^7 B_s	1.8×10^7 $\bar{B}_s$	0.12 = B_s Production
5.4×10^6	5.4×10^6	0.30 = 2-Arm Geometrical Acceptance
4.9×10^5	4.9×10^5	0.09 = BR($B_s \rightarrow D_s^*$, D_s and DK with $n\pi$
4.9×10^5	4.9×10^5	1.00 = BR($D_s^* \rightarrow D_s \gamma$)
2.4×10^4	2.4×10^4	0.05 = BR($D_s \rightarrow KK\pi$, $KK3\pi$, K^0K)
1.7×10^4	1.7×10^4	0.68 = No Other Interaction in Bunch Crossing
1.6×10^4	1.6×10^4	0.94 = Vertex Acceptance of Silicon μVertex
6.5×10^3	6.5×10^3	0.42 = Trigger Efficiency (D_s^* 3π)
3.3×10^3	3.3×10^3	0.50 = Event Efficiency Due to Track Finding Losses
1400 B_s	1400 $\bar{B}_s$	0.43 = Event Reconstruction Assumes Liquid-Xenon e.m. calorimetry.
950 B_s	950 $\bar{B}_s$	0.29 = Event Reconstruction Assumes Lead-Glass e.m. calorimetry.

The five parameters that have been changed are discussed in the following paragraphs.

- We now take the $b\bar{b}$ total cross section to be 15 μbarn. The 10 μbarn value previously used corresponded to a $|y| < 1.5$ rapidity cut [K. Ellis, private communication]. This yields a $b\bar{b}$ production sample of 1.5×10^{8} events per 10 pbarn^{-1}.

- We now assume that a $\bar{b}$-quark has a 12% probability to combine with an s-quark to make a B_s-meson. This should allow, for example, for the loss of excited B_s which can decay into D + K [V. Khoze, private communication].

- B_s Branching Ratios − We assume BR = 9% for the total of all reactions of the type:

$$B_s \rightarrow D_s^* + n\pi^{\pm}\ ,\ D_s + n\pi\ ,\ D_u + Kn\pi$$

  We noted in Table 7, page 56 of P238 that the observed ARGUS BR = 6.7% for reactions of the type $B_d \rightarrow D^* + n\pi$ with n = 1,2,3 [H. Schroeder, Rapporteur Talk at XXIV International Conference in HEP (August 1988 - Munich, FRG) and DESY 88-101]. We also assume that the D_s^* to direct D_s ratio is 3/1 and that the final state $D_u Kn\pi$ contributes at least 0.2 %, giving us the total of 9%. Since it seems likely that we shall also be able to reconstruct such final states with $n > 3$, our effective useful BR should be larger than this.

- $D_s^{\pm}$ Branching Ratio − We now take BR = 5% for all known charged final states: $K^+K^-\pi^{\pm}$, $K^+K^-3\pi$, $K^0K^{\pm}$ [P. Karchin, Rapporteur Talk at SLAC Lepton-Photon Conference (August 1989)].

- Event Efficiency Due to Track Finding Losses − We now assume a total event finding efficiency of 50% due to all possible track losses. This should be a very conservative assumption.

APPENDIX B: MONTE CARLO SIMULATION AND ANALYSIS OF RICH COUNTER DATA

In all our simulation and reconstruction work reported in P238 and P238Add.1, we have assumed that the RICH counter system perfectly identifies all particles. We are now attempting to make a more realistic estimate of the RICH identification efficiencies by simulating the RICH counter response to the tracks from B_s decay and to all other tracks in the detectors. These simulated RICH data are then analyzed, in order to extract identification information for the particles.

In order to obtain an overall efficiency for the RICH identification procedure, we have generated 200 B_s events, in which all particles in the final state $K^+K^-\gamma 4\pi$ (see Eq. 10 in P238Add.1) are contained in the spectrometer aperture. Fig. 2(a) shows the momentum distribution for kaons which emerge from the decay of the B_s. Fig. 2(b) shows the momentum for kaons in the spectrometer which are not from the B_s decay (they provide the K_p and K_s tagging sample discussed in Section 4.2 of P238Add.1). Fig. 3 shows the momentum ranges of unique separation for the indicated particles in the liquid and gas RICH counters.

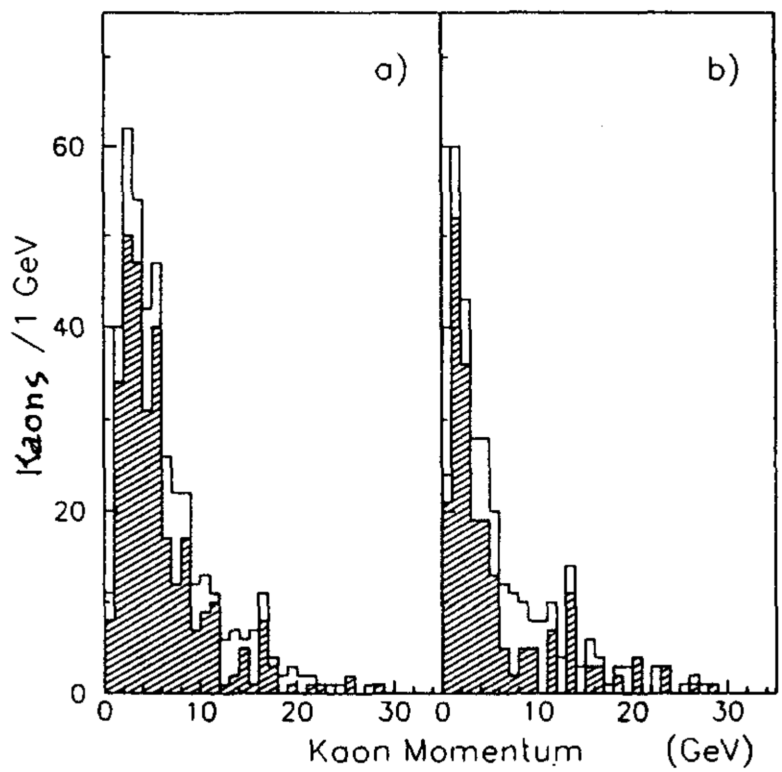

Figure 2: (a) Momentum distribution of $K^\pm$ which emerge from $B_s \rightarrow D_s^* 3\pi$ decay. Shaded histogram shows those that enter the first spectrometer (100-600 mrad); (b) Momentum distribution of $K^\pm$ in the detector, which do not come from the decay of B_s. Shaded histogram is same as in (a).

We have started by doing an accurate simulation of the Liquid RICH counter in the first (100-600 mrad) spectrometer. The Liquid RICH counters are the most difficult for the following reasons:

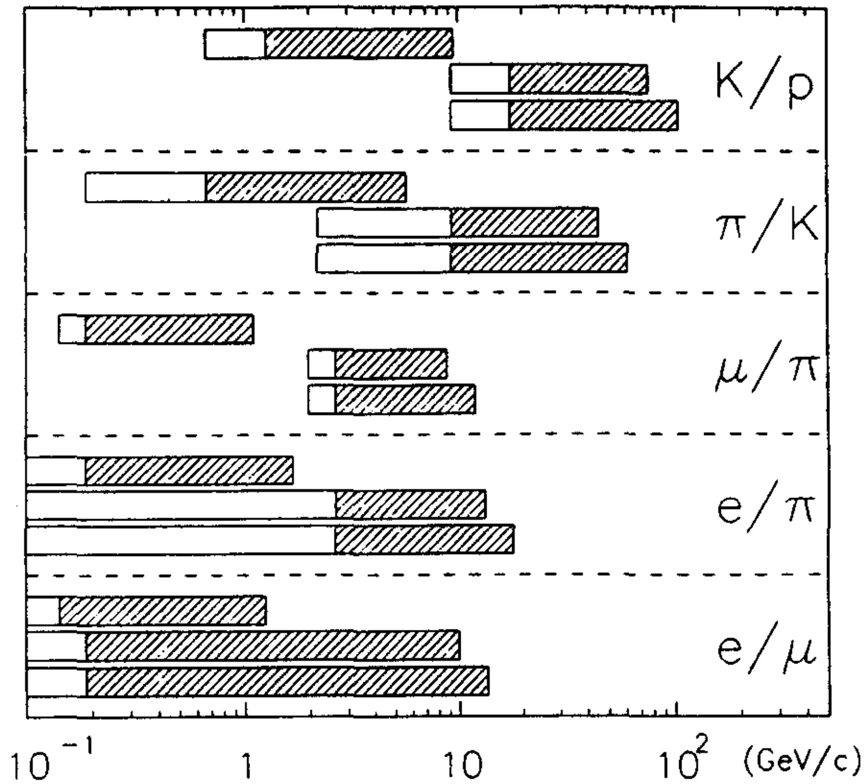

Figure 3: Momentum Ranges of RICH counter Identification. For each indicated pair of particles, the bars at lower momentum are for the liquid RICH counters; the two bars at higher momenta are for the gas RICH counters in the first and second spectrometers, respectively. In all cases, the open bars show the momentum range between the thresholds for the lighter and heavier particles. The upper limits for the hatched bars in all cases show the upper limit for 3σ separation (it is higher for the gas counter of spectrometer 2 because its gas radiator is somewhat longer).

- The number of particles which produce Cerenkov light in the liquid RICH is larger than in the gas counters (pion threshold is about 0.2 GeV/c in the liquid and is about 2.6 GeV/c in the gas counters).
- The "rings" are only rings for particles at normal incidence. Away from normal incidence, the light is seen in conic sections which have been truncated by light loss due to total internal reflection in the liquid radiator.
- The radii of the liquid RICH "rings" are large. Thus, there is considerable overlap of the rings from different particles. There is also some light loss to the walls of the counter.

To illustrate the enormous difference between the signals in the detector planes of both types of counters, we show in Figs. 4(a,b) the detector planes for typical events in, respectively, the liquid and gas RICH counters. For the gas counter, the signals from nine events are superimposed. Note also that the noise signals referred to below are not shown in these figures.

Because the rings in the gas RICH are much much smaller and relatively well isolated, for the purposes of this study, we provisionally assume that the Gas RICH counter perfectly identifies all par-

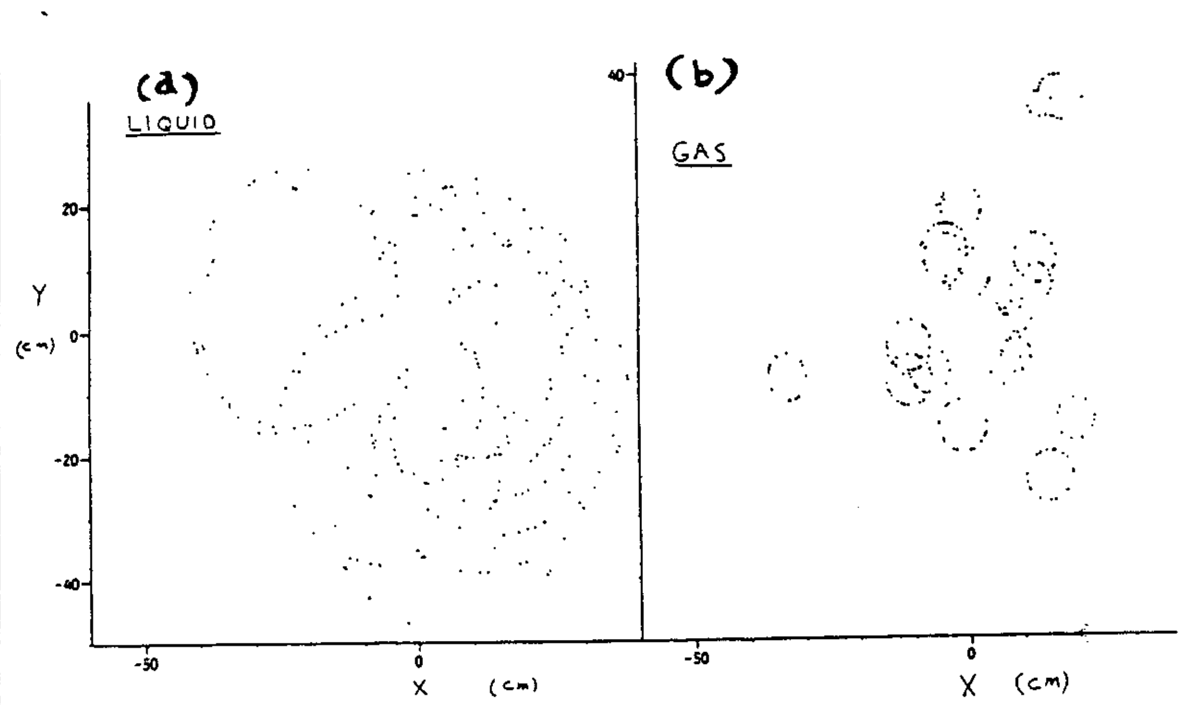

Figure 4: (a) Photon Images for One Typical Event in Detector Plane of Liquid RICH; (b) Photon Images in Detector Plane of Gas RICH. The signals from 9 events are superimposed in the gas RICH figure. Noise signals referred to in the text are not shown in either figure.

ticles for which at least 4 photons are detected. We are in the process of extending our modeling to the entire system and should soon have a more complete answer. We first describe the RICH counter simulation, then the reconstruction algorithm and finally present the results of this study.

RICH Data Simulation

Apart from an approximation described in the next paragraph, the Liquid RICH counter geometry used for this simulation is identical to that described in P238. As shown in Figs. 22 and 38 of P238, the counter consists of a 1 cm thick radiator which is followed by a 3mm thick quartz window. Cerenkov photons which are emitted in the radiator pass through the window into a 25 cm long, helium-filled volume. After traversing the helium, the photons pass through a second quartz window into a photon detector. As described in Section 5.5 of the proposal, this detector consists of a TMAE conversion layer followed by two parallel-plate amplification regions, and a detector with 3×3 mm^2 pixels.

For ease of simulation, all windows, detectors and radiators were assumed to have surfaces perpendicular and parallel to the beam axis. This differs slightly from the proposed geometry in which the normals to the windows are along the average particle direction (see Fig. 22 of P238). This approximation slightly decreases the number of photons detected in a ring image (because of increased losses due to total internal reflection), but should have little effect on the the ring reconstruction problem. In fact, the average number of "detected" photons generated by the program (20) is very close to the 23.4 photons measured by R. Arnold et al. [CRN/HE 87−08] for a $\beta = 1$ track normally incident on a similar prototype module.

All physical effects relating to the generation and propagation of the Cerenkov photons were carefully simulated. Tracks entering the RICH radiator are multiple-scattered between emission of photons. The photons are propagated through the radiator, the two quartz windows and the helium space, taking into account the energy-dependent index of refraction and absorption lengths in each medium. Reflection probabilities are calculated at each interface between two materials with differing indices of refraction and photons were eliminated if reflection takes place. The distance each photon travels in the detector before absorption is then calculated, and the detected photon position is digitized, assuming 3×3 mm^2 pads.

Cerenkov light is also generated by all tracks as they traverse the quartz windows (this effect is expected to account for the major fraction of noise photons). These photons are propagated through the counter to the detector in the same manner as those generated in the radiator. It may be noted that the counter configuration used in the present simulation (perpendicular to the beam axis, rather than rotated as in Fig. 22 of P238) overestimates the number of photons from this source, since most photons from tracks normally incident on the quartz are internally reflected in the windows.

Analysis of Simulated RICH Data

The input to our provisional reconstruction algorithm is the list of tracks and their trajectories and momenta, as well as the list of hit RICH detector pads produced by the simulation program. As described below, we assume that, if a particle's velocity is above Cerenkov threshold for pions in the gas RICH counter, the gas counter gives a correct particle identification.

For a given measured charged track, the analysis is based on the reconstruction of a Cerenkov emission angle, θ_c, for each detected photon (at present, each struck 3×3 mm^2 pad is interpreted as one photon). A straightforward ray calculation, which includes refraction at the interfaces, gives two equations for the coordinates (x,y) of converted photons in the photon detector as a function of θ_c and the azimuthal Cerenkov emission angle, ϕ_c. For each track, we use these equations and standard numerical techniques to give θ_c and ϕ_c for each detected photon (if a solution exists).

The subsequent analysis is facilitated by the removal of hits in the Liquid RICH detector, which constitute background from two sources:

- For the relatively few tracks in each event which are above Cerenkov threshold in the Gas RICH, a random number, n, is generated according to a Poisson distribution, whose mean is the expected β-dependent photo-electron yield (20 for $\beta = 1$). If $n > 4$, we assume that the Gas RICH counter correctly identifies this track (tracks whose momenta are between pion and kaon thresholds in that counter, and which have no light, are assumed to be kaons). We then remove, from the Liquid RICH hit list, all photons from these tracks which are within 2 standard deviations of their expected θ_c (this standard deviation is discussed in Section 5.5 of P238).
- Cerenkov photons produced in the quartz detector window are removed by removing all hits produced in a 1 cm radius circle about the point where the particle enters the photon detector.

Since, as discussed above, the gas RICH counter is assumed to correctly identify all tracks which are above about 2.6 GeV (pion threshold in that counter), we now investigate with our detailed simulation how well the liquid RICH counter can be used to identify tracks with momentum below 2.6 GeV. Fig. 5 shows a histogram of the values of θ_c for an identified kaon track in a typical B_s event after the above cleanup procedure.. A peak is seen at an angle which corresponds to the Cerenkov emission angle for the track in question. In general, the situation may not be so obvious.

In order to quantify the RICH identification picture, we have employed the following algorithm (somewhat arbitrarily). For each track with momentum below 2.6 GeV, and for each possible mass identity, we count the number of the photons within a "road" of width, $2\sigma_c$, where σ_c is the expected standard deviation on θ_c referred to above (see Section 5.5 of P238). A photon count thus results for

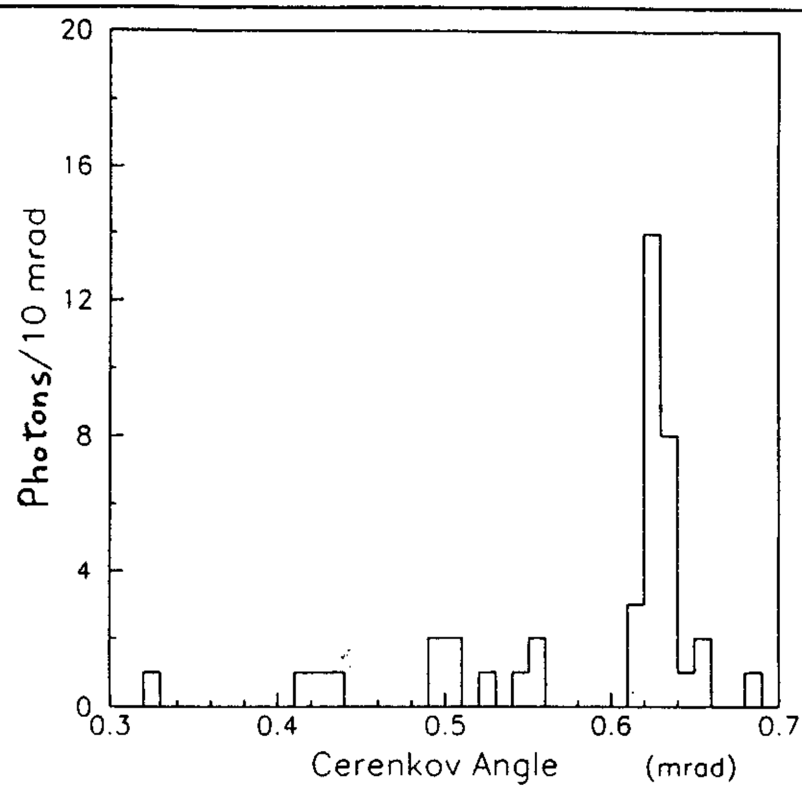

Figure 5: Histogram of reconstructed Cerenkov emission angles for a typical kaon track that is identified by the liquid RICH counter. The momentum of this kaon is 1.7 GeV/c.

each mass identity possibility. For the particle to be uniquely identified as a particular type, the algorithm requires:

- The photon count, $n_\gamma > 5$, within the "road" for that particle type.
- For all other particle types, their photon counts, $n_\gamma' < n_\gamma - 4$.

We are also exploring other more sophisticated algorithms but this relatively simple one already gives rather good results. Table 2 gives the results of the analysis for the sample of 200 events. The rows are the "true" identities of the tracks and the columns are the identities deduced using the above algorithm.

We see in Table 2 that 85% of all "real" kaons are called kaons by the RICH counters. On the other hand, of all tracks that are called kaons by the RICH counters, 88% of these are real kaons. As commented above, we are fairly confident that these efficiencies can be improved, as we use increasingly more sophisticated reconstruction algorithms.

*Table 2: RICH Counter Identification Matrix for 200 B_s Events**

		Identification from RICH counters			
		p	K	π	pKπ
'True' ID	p	22	22		26
	K	3	372	5	62
	π	10	30	1277	673

(*) For simplification, muons are not included here. Their contribution is small, however.